

Cover Page



Universiteit Leiden



The handle <http://hdl.handle.net/1887/92885> holds various files of this Leiden University dissertation.

Author: Ruytenberg, T.

Title: Novel magnetic resonance antennas and applications

Issue Date: 2020-06-04

NOVEL MAGNETIC RESONANCE ANTENNAS AND APPLICATIONS

NOVEL MAGNETIC RESONANCE ANTENNAS AND APPLICATIONS

Proefschrift

ter verkrijging van

de graad van doctor aan de Universiteit Leiden,

op gezag van de Rector Magnificus prof. mr. C.J.J.M. Stolker,

volgens besluit van het College voor Promoties,

te verdedigen op donderdag 4 juni 2020

klokke 13:45 uur

door

Thomas RUYTENBERG

Geboren te Capelle aan den IJssel

in 1992

Promotor

Prof. dr. A.G. Webb¹

Copromotor

Prof. dr. P. Börnert^{1,2}

Promotiecommissie

Prof. dr. ir. M.J.P. van Osch¹

Prof. dr. ir. T.H. Oosterkamp³

Prof. dr. J. Dankelman⁴

¹ *Leiden University Medical Center, Leiden, The Netherlands*

² *Philips Research, Hamburg, Germany*

³ *Leiden University, Leiden, The Netherlands*

⁴ *Delft University of Technology, Delft, The Netherlands*

This work is part of the research programme 'From Coil to Antenna' with project number 13783, which is financed by the Dutch Research Council (NWO).

Typesetting by T. Ruytenberg in \LaTeX

Cover design by E.C. Blik

Copyright ©2019 by T. Ruytenberg

An electronic version of this dissertation is available at the Leiden University Repository.

CONTENTS

1	General Introduction	1
1.1	The wider perspective.	2
1.2	RF coils in MRI	2
1.3	Design considerations	4
1.4	High permittivity materials	7
1.5	This work	8
	References	10
2	High Resolution Laryngeal Imaging	15
2.1	Introduction	16
2.2	Materials and Methods	19
	2.2.1 Coil Development	19
	2.2.2 Protocol Development	19
2.3	Results	22
	2.3.1 Healthy Volunteers.	22
	2.3.2 Patient Scanning.	22
2.4	Discussion	24
2.5	Conclusion	28
2.6	Acknowledgments	28

References	29
3 Shielded-Coaxial-Cable Coils	33
3.1 Introduction	34
3.2 Methods	35
3.2.1 Coil fabrication	35
3.2.2 Electromagnetic simulations.	37
3.2.3 MRI measurements	37
3.3 Results	39
3.3.1 Comparison of conventional and SCC coils	39
3.3.2 Receive-only array – knee imaging	39
3.3.3 Transceive array – knee imaging	43
3.3.4 Transceive array – hand imaging	44
3.4 Discussion	48
3.5 Conclusion	49
3.6 Acknowledgements	49
References	50
4 Detunable Dielectric Resonator Receive Array	53
4.1 Introduction	54
4.2 Methods	55
4.3 Results	55
4.4 Conclusions.	59
4.5 Acknowledgments	60

References	61
5 Integrated High Permittivity Materials	63
5.1 Introduction	64
5.2 Methods	65
5.2.1 Coil manufacturing and characterization	65
5.2.2 Electromagnetic Simulations	66
5.2.3 Imaging sequences.	66
5.3 Results	67
5.4 Conclusion and Discussion	73
5.5 Acknowledgements	75
References	76
6 Summary and General Discussion	79
6.1 Summary	80
6.2 General Discussion	81
References	84
Nederlandse samenvatting	85
Acknowledgements	87
Curriculum Vitæ	89
List of Publications	91

1

GENERAL INTRODUCTION

T. RUYTENBERG

1.1. THE WIDER PERSPECTIVE

In health care, medical imaging has become an ever more used diagnostic tool [1–3]. Not only have medical imaging techniques become more available in the developed world [4], also imaging capabilities per modality have increased due to technological advances. In magnetic resonance imaging (MRI) specifically, during the last decades increasing static magnetic field strengths, the invention of acceleration algorithms, advanced radio frequency (RF) antenna design, and the increase in computation power for reconstruction of images have brought many advances in increasing the quality and resolution of MRI images. This thesis will focus on the topic of RF antenna and antenna array design and in this introduction the role of RF antennas in MRI and some important design criteria are covered.

1.2. RF COILS IN MRI

Using MRI, spin systems can be studied by creating a net magnetization in a sample using a large magnet and subsequently perturbing it out of its equilibrium state and measuring the precession frequency of the system. MRI systems are most used in clinical practise to image humans for diagnostic purposes utilizing static magnetic field strengths in the order of Tesla (T). This static magnetic field is called the B_0 field.

Once a magnetization has been established in the sample, the system can be probed using a second time-dependent magnetic field at the Larmor precession frequency. This field is named the B_1 field, and by looking at the gyromagnetic ratio for protons $\gamma = 42.58 \text{ MHz T}^{-1}$, given the B_0 field strengths used in clinical practise, one easily calculates that the working frequencies are in the radio frequency range and therefore to be applied and detected with radio antennas. During an experiment a transmit B_1 field is applied and receive B_1 field is measured via the radio antenna, for which often the term 'coil' is used. It is an important notion that these transmit and receive fields are not necessarily identical.

Due to the precession of the spins, the B_1 fields are polarized circularly [5]. Fields acting on the spin system and fields generated by the spin system are therefore oppositely polarized. We can therewith define the two fields separately if the direction of the B_0 field is defined [6]

$$\mathbf{B}_0 = B_0 \hat{\mathbf{z}} \quad (1.1)$$

$$\mathbf{B}_1 = \hat{\mathbf{x}}B_{1x} + \hat{\mathbf{y}}B_{1y} + \hat{\mathbf{z}}B_{1z} \quad (1.2)$$

$$\mathbf{B}_1^+ = (\hat{\mathbf{x}} + j\hat{\mathbf{y}})\mathbf{B}_1 / \sqrt{2} \quad (1.3)$$

$$\mathbf{B}_1^- = (\hat{\mathbf{x}} - j\hat{\mathbf{y}})\mathbf{B}_1 / \sqrt{2} \quad (1.4)$$

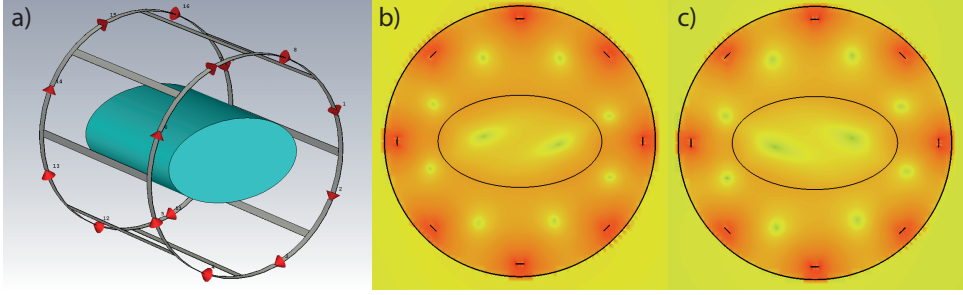


Figure 1.1: A birdcage coil and its produced fields in a phantom. a) birdcage coil drawn in simulation software, showing the birdcage with the red cones being discrete ports simulated as capacitors including a total of two driving ports. (shield around coil not shown for visibility) b) and c) the simulated B_1^+ and B_1^- fields, showing asymmetry. The phantom has an electric permittivity of $\epsilon_r = 60$ and conductivity of $\sigma = 1.0 \text{ S/m}$

where B_1^+ is the transmit field and B_1^- the receive field.

A convenient way to produce and detect these circularly polarized fields, also called quadrature excitation or detection [7], was found by Hayes et al. [8] in 1985 with the creation of the birdcage coil (see Figure 1.1a). Essentially an annular multi-loop coil with shared conductors and a single, or two driving channels in the case of quadrature excitation. The birdcage coil has become the working horse in MRI and is incorporated in every 1.5 and 3.0 T system as a body coil. The birdcage has the advantage of being able to produce a rather homogeneous B_1 field.

While the transmit and receive fields differ in polarization, additionally the field distribution can vary spatially throughout the sample due to secondary magnetic fields created by induced currents in the sample via Maxwell's law with Ampère's addition

$$\nabla \times \mathbf{B}_1 = \mu_0 \mathbf{J}_c + \mu_0 \mathbf{J}_d = \mu_0 (\sigma + \epsilon_0 \epsilon_r j\omega) \mathbf{E} \quad (1.5)$$

with \mathbf{J}_c the conduction current and \mathbf{J}_d the displacement current. Note that the secondary magnetic fields become larger at higher frequencies (or field strengths) and higher conductivities of the sample. Thereby also the asymmetry between the transmit and receive field will increase, depicted in Figure 1.1b and c. Additional examples of asymmetry at different field strengths have for example been published by Vaidya et al. [9].

1.3. DESIGN CONSIDERATIONS

RECEIVE-ONLY COILS

Even though the birdcage coil is often used in clinical MRI due to its large volume coverage with rather homogeneous B_1 fields, it is not very reasonably sensitive on the receive side, as the coil is up to tens of centimeters away from the region of interest to be imaged and the signals to be measured are small in the order of milliwatt. A method for substantially increasing the signal-to-noise ratio (SNR) was described in detail by Hoult [5] in 1978 for applications in NMR. By splitting the transmit and receive chain, one can use the body coil as homogeneous transmitter and a separate receive-only coil close to the region of interest. For an extended region of interest though, one would have to move the receive coil around to compensate for the limited FOV (field of view) of such a coil. A solution to extend the FOV would be to create an array of multiple adjacent receive loop coils and a working setup incorporating this idea in MRI was presented in 1990 by Roemer [10].

The difficulties arising from making an array of coils in MRI originate from the fact that the separate elements in such an array are in each others electromagnetic near-field. Therefore, a coupling exists between these elements. As MRI functions with narrow-band resonators as antennas, one obtains a system of damped coupled resonators for which only system-wide modes are present. These new coupled modes are not at the original resonant frequency of the single uncoupled elements anymore, resulting in an off-resonance antenna, useless for MRI.

Roemer solved this issue by compensating the initial coupling by introducing additional coupling between elements in the form of overlap. By overlapping elements, additional magnetic flux from one element to the other is induced, but with an opposite sign. This way the total inductive coupling cancels out between neighbouring elements if done precisely. For next-nearest neighbours this decoupling method does not work, as no overlap can be created between these elements.

Nowadays, receive-only coils are universally used when working with clinical MRI scanners. Head coils often consist of 32 or more elements, while body arrays are growing towards 128 or even more elements. In general more elements will result in a higher surface SNR, while central SNR depends more on the total array coverageⁱ [11–14]. Many of these multi-element arrays depend on overlap for reducing most of their coupling between neighbouring elements.

While overlapping elements is generally very effective for loop coils, the decoupling can be compromised under varying loading conditions of the coil, can be less or more effective at different field strengths [15, 16], and the method cannot be applied to coils with very different geometries than loops. Different methods to decouple elements within an

ⁱGoing to extremes in number of elements may tip the balance from gaining additional signal with extra channels, to a built-up of coil noise, reducing total SNR.

array have been extensively described. For example, introducing additional resonating circuits between elements [17–21], adjusting current distributions [22, 23], intrinsic geometric decoupling if different coil types are used [24], preamplifier decouplingⁱⁱ [10] and the use of high impedance coils [27].

With the presence of receive-arrays in MRI, algorithms to accelerate imaging, like SMASH [28], SENSE [29] and GRAPPA [30] were introduced in 1997, 1999 and 2002 respectively. Additionally to the practical problem of shifting resonances that arises from inter-element coupling in an array as discussed previously, these algorithms also degrade under high amounts of coupling. Even though the mathematical approaches to these methods are not very difficult to follow, only the intuitive way of their working is briefly touched upon here, as they are intuitively easy to comprehend and the math has been written down before in the referenced work. The methods described in this paragraph all rely on the fact that one obtains virtually free additional information when scanning with an array. When a scan is performed with an n -channel array, n -times more data is acquired compared to the single channel coil. Combined with knowledge that the individual elements within the array are only sensitive within their own immediate surrounding, free spatial encoding is obtained when using an array at the only cost of sampling multiple channels. An n -channel array would therefore theoretically allow for an acceleration of n , as in that case the same amount of data is sampled.

However, for this to work perfectly, the sensitivities of the individual channels need to be unique and non-overlapping. In the mathematical approach this manifests itself as the noise correlation matrix of the channels. If two channels show correlation in their noise, they are partly sampling the same MRI signal either because these channels both have sensitivity for the same voxel, or because MRI signal is picked up by a channel and directly coupled into another channel via the electronics. Whichever of the underlying coupling pathways occur, they both result in non-unique channels, thereby slightly spoiling the acceleration method in the form of spatially-dependent noise amplification in the accelerated images. Where exactly in the images the noise will be amplified therefore depends on the total scan setup, composed of the array geometry, the object geometry and the acceleration factor being used. The noise amplification is therefore also called the geometry factor and for a pixel p it is in the SENSE algorithm given by [29]

$$g_p = \sqrt{[(S^H \Psi^{-1} S)^{-1}]_{p,p} (S^H \Psi^{-1} S)_{p,p}} \geq 1 \quad (1.6)$$

with S being a vector with all the pixel intensities per channel, H indicating the Hermitian transpose and Ψ the noise correlation matrix. A properly decoupled array shows low geometry factors for high accelerations and using a SENSE acceleration factor of R will show the following SNR

ⁱⁱ Although preamplifier decoupling eases construction of arrays, SNR gains have been disputed if the combination of channels is done with proper weightings [25, 26]

$$SNR_p^{SENSE} = \frac{SNR_p^{FULL}}{g_p \sqrt{R}} \quad (1.7)$$

compared to the fully sampled SNR case. A properly decoupled array therefore not only shows a low g -factor, but therefore also directly increases SNR when using accelerated scanning.

TRANSMIT-ONLY COILS

With the introduction of receive-only coils in this chapter, one obviously still needs a transmitter to excite the spin system and this can be either a transmit-only, or a transceive coil. In clinical practise, often the large body (birdcage) coil is used, but in some specific cases transmit arrays are chosen. When designing transmit coils, not only transmit efficiency is important in design, especially the safety aspects have to be considered as in the order of kilowatts of RF power is applied using these antennas resulting in E-field induced heating, also called the specific absorption rate (SAR). While transmit efficiency can easily be measured, as it concerns an applied B-field. E-field induced heating however, is not easily measured in-situⁱⁱⁱ. Therefore heating is often simulated using finite-difference time-domain simulations and these simulations have become much more important with the use of transmit coil arrays close to the body, not only due to their potentially high local E-fields, but also due to their dependency of the phase settings per transmit channel. When an array is driven with a set of phases for the different channels, constructive interference can occur in a certain region within the subject, while it might not for another set of phases [33].

An example of how some coils have evolved through time considering these transmit design criteria can be seen with the dipole-type antennas [34–36]. These coils are more often used to replace or complement [24, 35–37] loop coil arrays for field strengths beyond 3 T. Their efficiency at high-field is sometimes explained by their generated current patterns adhering more to the ideal current patterns needed for optimum SNR [38, 39]. The continued work on dipoles has led to small adaptations in geometry such as folding, bumping, fractionating and meandering [39–42], inversion via Babinet's principle [43] to slots [44] and passively fed dipoles [45], most of them with the intention to improve transmit efficiency and to reduce E-field induced heating.

ARRAY DESIGN CRITERIA

For receive-only arrays it is important to consider:

- Inter-element decoupling

ⁱⁱⁱA single indirect method to measure temperature increase with MRI is well-described in literature, based on the proton resonance frequency temperature-dependency [31, 32].

- Decoupling from the transmit coil
- The total amount of elements and their arrangement as this influences acceleration performance and surface SNR
- The amount of surface coverage to obtain sufficient central SNR for the application

For transmit-only/transceive arrays additionally:

- Known E-field-induced heating characteristics
- Components should be chosen such that they can handle the intended power levels

Indubitably, safety is of the utmost importance when putting a coil into use. Besides safety on the RF side, mechanical safety, electrical safety and flammability of the coil should be considered. [33]

1.4. HIGH PERMITTIVITY MATERIALS

MRI is a well-coordinated play between the spin system under study (often a human being) and the antenna-system as exciters and as sensor. The mediator between these two is the electromagnetic field, which is bound by the properties of the whole system and especially the subject in the case of MRI, as it has a non-vacuum electric permittivity. Implications of this non-vacuum, and at the same time frequency-dependent, permittivity are well-known and understood and have its largest impact at ultra-high field MRI where it manifests as B_1 -field inhomogeneity [46, 47]. This is also where the first application of high permittivity materials presents itself, to perturb the B_1^+ -field, such to obtain an increased or more homogeneous transmit field in an anatomy or region of interest [48–50].

Another application can (simultaneously) be found on the receive side, where additionally sensitivities can be enhanced [50, 51], which will also be the subject of Chapter 5.

Other uses of dielectric materials include for example dielectric resonators [52–56]. By exciting an electromagnetic mode of the resonators, and having the imaging region of interest close to or even inside the maximum of the H-field of this mode, imaging sensitivities can be enhanced. Also in the area of implant safety, dielectric materials may have its benefits [57].

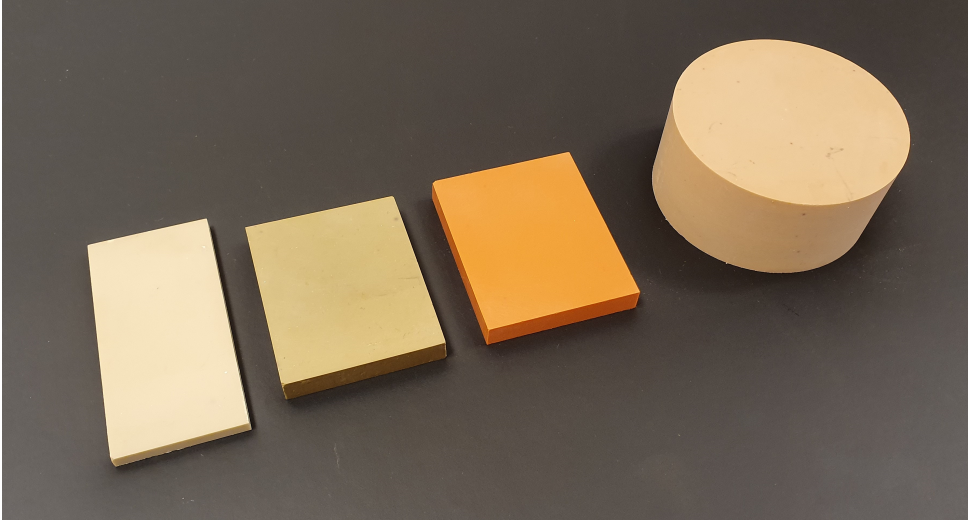


Figure 1.2: A variety of solid high permittivity material used in MRI. From left to right: lead zirconate titanate ($\epsilon_r = 1070$ and $\sigma = 1.5 \text{ S/m}$) used in Chapter 4, lead zirconate titanate ($\epsilon_r = 660$ and $\sigma = 0.01 \text{ S/m}$) used in Chapter 5, barium titanate with zirconium dioxide and ceric dioxide additives ($\epsilon_r = 4500$ and $\sigma = 1.79 \text{ S/m}$) used in Reference [45] and barium strontium titanate ($\epsilon_r = 165$) used in Reference [58]

1.5. THIS WORK

The work described in this thesis covers a range of surface coil designs, partly using high permittivity materials, and their applications.

Chapter 2 demonstrates high resolution laryngeal imaging using a semi-flexible dedicated coil. While clinical laryngeal scanning is often difficult, both due to artefacts of swallowing and breathing, and due to low sensitivity of generally used coils for this anatomy, the dedicated coil and the implemented sequences therewith resulted in high quality images of the larynx.

A very flexible transceiver and receive-only array was designed in **Chapter 3** using coaxial cable loop antennas. Even though the array is flexible, does not contain any lumped elements in the resonating circuit, and has no inter-element decoupling circuitry, the array shows lower inter-element decoupling than an array of conventional loop coils.

Chapter 4 describes a novel receive-only array of dielectric resonator antennas. When resonant dielectric materials are being used for receive-only purposes, they need to be detuned during the transmit phases when scanning. For these solid dielectric resonators, this was achieved by attaching PIN-diodes to the resonators using conductive silver paint, which resulted in a fully electrically detunable coil with dielectric resonators.

In **Chapter 5** the use of fully integrated high-permittivity material in receive-only coils

is described. While the use of high-permittivity materials in MRI have been extensively researched in literature, integrating these materials starting from the design phase had not yet been described. This chapter presents the benefits of doing so by comparing coils constructed for imaging the neck with and without high-permittivity material.

REFERENCES

- [1] W. R. Hendee, G. J. Becker, J. P. Borgstede, J. Bosma, W. J. Casarella, B. A. Erickson, C. D. Maynard, J. H. Thrall, and P. E. Wallner, *Addressing overutilization in medical imaging*, *Radiology* **257**, 240 (2010).
- [2] R. Smith-Bindman, D. L. Miglioretti, and E. B. Larson, *Rising use of diagnostic medical imaging in a large integrated health system*, *Health affairs* **27**, 1491 (2008).
- [3] R. Smith-Bindman, D. L. Miglioretti, E. Johnson, C. Lee, H. S. Feigelson, M. Flynn, R. T. Greenlee, R. L. Kruger, M. C. Hornbrook, D. Roblin, *et al.*, *Use of diagnostic imaging studies and associated radiation exposure for patients enrolled in large integrated health care systems, 1996-2010*, *Jama* **307**, 2400 (2012).
- [4] Organisation for Economic Co-operation and Development, *Health Statistics 2019: Health Care Utilisation*, <https://stats.oecd.org/>.
- [5] D. Hoult, *The NMR receiver: a description and analysis of design*, *Progress in Nuclear Magnetic Resonance Spectroscopy* **12**, 41 (1978).
- [6] T. S. Ibrahim, *Analytical approach to the MR signal*, *Magnetic Resonance in Medicine: An Official Journal of the International Society for Magnetic Resonance in Medicine* **54**, 677 (2005).
- [7] C.-N. Chen, D. Hoult, and V. Sank, *Quadrature detection coils - a further $\sqrt{2}$ improvement in sensitivity*, *Journal of Magnetic Resonance* (1969) **54**, 324 (1983).
- [8] C. E. Hayes, W. A. Edelstein, J. F. Schenck, O. M. Mueller, and M. Eash, *An efficient, highly homogeneous radiofrequency coil for whole-body NMR imaging at 1.5 T*, *Journal of Magnetic Resonance* (1969) **63**, 622 (1985).
- [9] M. V. Vaidya, C. M. Collins, D. K. Sodickson, R. Brown, G. C. Wiggins, and R. Lattanzi, *Dependence of and field patterns of surface coils on the electrical properties of the sample and the MR operating frequency*, *Concepts in Magnetic Resonance Part B: Magnetic Resonance Engineering* **46**, 25 (2016).
- [10] P. B. Roemer, W. A. Edelstein, C. E. Hayes, S. P. Souza, and O. M. Mueller, *The NMR phased array*, *Magnetic resonance in medicine* **16**, 192 (1990).
- [11] G. C. Wiggins, J. R. Polimeni, A. Potthast, M. Schmitt, V. Alagappan, and L. L. Wald, *96-channel receive-only head coil for 3 Tesla: design optimization and evaluation*, *Magnetic Resonance in Medicine: An Official Journal of the International Society for Magnetic Resonance in Medicine* **62**, 754 (2009).
- [12] G. C. Wiggins, C. Triantafyllou, A. Potthast, A. Reykowski, M. Nittka, and L. Wald, *32-channel 3 Tesla receive-only phased-array head coil with soccer-ball element geometry*, *Magnetic Resonance in Medicine: An Official Journal of the International Society for Magnetic Resonance in Medicine* **56**, 216 (2006).

- [13] B. Keil, J. N. Blau, S. Biber, P. Hoecht, V. Tountcheva, K. Setsompop, C. Triantafyllou, and L. L. Wald, *A 64-channel 3T array coil for accelerated brain MRI*, *Magnetic resonance in medicine* **70**, 248 (2013).
- [14] M. Schmitt, A. Potthast, D. E. Sosnovik, J. R. Polimeni, G. C. Wiggins, C. Triantafyllou, and L. L. Wald, *A 128-channel receive-only cardiac coil for highly accelerated cardiac MRI at 3 Tesla*, *Magnetic Resonance in Medicine: An Official Journal of the International Society for Magnetic Resonance in Medicine* **59**, 1431 (2008).
- [15] N. Avdievich, A. Pfrommer, I. Giapitzakis, and A. Henning, *Analytical modeling provides new insight into complex mutual coupling between surface loops at ultrahigh fields*, *NMR in Biomedicine* **30**, e3759 (2017).
- [16] N. I. Avdievich, I.-A. Giapitzakis, A. Pfrommer, and A. Henning, *Decoupling of a tight-fit transceiver phased array for human brain imaging at 9.4 T: Loop overlapping rediscovered*, *Magnetic resonance in medicine* **79**, 1200 (2018).
- [17] N. I. Avdievich, J. W. Pan, and H. P. Hetherington, *Resonant inductive decoupling (RID) for transceiver arrays to compensate for both reactive and resistive components of the mutual impedance*, *NMR in Biomedicine* **26**, 1547 (2013).
- [18] X. Yan, X. Zhang, B. Feng, C. Ma, L. Wei, and R. Xue, *7T transmit/receive arrays using ICE decoupling for human head mr imaging*, *IEEE transactions on medical imaging* **33**, 1781 (2014).
- [19] X. Yan, L. Wei, S. Chu, R. Xue, and X. Zhang, *Eight-channel monopole array using ICE decoupling for human head MR imaging at 7 T*, *Applied magnetic resonance* **47**, 527 (2016).
- [20] Y. Li, Z. Xie, Y. Pang, D. Vigneron, and X. Zhang, *ICE decoupling technique for RF coil array designs*, *Medical physics* **38**, 4086 (2011).
- [21] X. Yan, J. C. Gore, and W. A. Grissom, *New resonator geometries for ICE decoupling of loop arrays*, *Journal of Magnetic Resonance* **277**, 59 (2017).
- [22] X. Yan, J. C. Gore, and W. A. Grissom, *Self-decoupled RF coils*, in *Proceedings 25. Annual Meeting International Society for Magnetic Resonance in Medicine*, Vol. 25 (Honolulu, Hawaii, 2017) p. 0757.
- [23] X. Yan, J. C. Gore, and W. A. Grissom, *Multi-row and loopole-type self-decoupled RF coils*, in *Proceedings 26. Annual Meeting International Society for Magnetic Resonance in Medicine*, Vol. 26 (Paris, France, 2018) p. 4271.
- [24] M. A. Ertürk, A. J. Raaijmakers, G. Adrian, K. Uğurbil, and G. J. Metzger, *A 16-channel combined loop-dipole transceiver array for 7 Tesla body MRI*, *Magnetic resonance in medicine* **77**, 884 (2017).
- [25] A. Reykowski, C. Saylor, and G. R. Duensing, *Do we need preamplifier decoupling?* in *Proceedings 19. Annual Meeting International Society for Magnetic Resonance in Medicine*, Vol. 19 (Montréal, Canada, 2011) p. 3883.

- [26] C. Findekklee, O. Lips, P. Vernickel, C. Leussler, and R. Duensing, *Preamp decoupling improves SNR and the earth is flat*, in *Proceedings 27. Annual Meeting International Society for Magnetic Resonance in Medicine*, Vol. 27 (Montréal, Canada, 2019) p. 0563.
- [27] B. Zhang, D. K. Sodickson, and M. A. Cloos, *A high-impedance detector-array glove for magnetic resonance imaging of the hand*, *Nature biomedical engineering* **2**, 570 (2018).
- [28] D. K. Sodickson and W. J. Manning, *Simultaneous acquisition of spatial harmonics (SMASH): fast imaging with radiofrequency coil arrays*, *Magnetic resonance in medicine* **38**, 591 (1997).
- [29] K. P. Pruessmann, M. Weiger, M. B. Scheidegger, and P. Boesiger, *SENSE: sensitivity encoding for fast MRI*, *Magnetic resonance in medicine* **42**, 952 (1999).
- [30] M. A. Griswold, P. M. Jakob, R. M. Heidemann, M. Nittka, V. Jellus, J. Wang, B. Kiefer, and A. Haase, *Generalized autocalibrating partially parallel acquisitions (GRAPPA)*, *Magnetic Resonance in Medicine: An Official Journal of the International Society for Magnetic Resonance in Medicine* **47**, 1202 (2002).
- [31] J. D. Poorter, C. D. Wagter, Y. D. Deene, C. Thomsen, F. Stahlberg, and E. Achten, *Noninvasive MRI thermometry with the proton resonance frequency (PRF) method: in vivo results in human muscle*, *Magnetic resonance in medicine* **33**, 74 (1995).
- [32] F. F. Simonis, E. T. Petersen, J. J. Lagendijk, and C. A. van den Berg, *Feasibility of measuring thermoregulation during RF heating of the human calf muscle using MR based methods*, *Magnetic resonance in medicine* **75**, 1743 (2016).
- [33] J. Hoffmann, A. Henning, I. A. Giapitzakis, K. Scheffler, G. Shajan, R. Pohmann, and N. I. Avdievich, *Safety testing and operational procedures for self-developed radiofrequency coils*, *NMR in Biomedicine* **29**, 1131 (2016).
- [34] A. Raaijmakers, O. Ipek, D. W. Klomp, C. Possanzini, P. Harvey, J. J. Lagendijk, and C. A. van Den Berg, *Design of a radiative surface coil array element at 7 T: the single-side adapted dipole antenna*, *Magnetic resonance in medicine* **66**, 1488 (2011).
- [35] A. Raaijmakers, P. R. Luijten, and C. A. van Den Berg, *Dipole antennas for ultrahigh-field body imaging: a comparison with loop coils*, *NMR in Biomedicine* **29**, 1122 (2016).
- [36] M. K. Woo, R. L. Lagore, L. DelaBarre, B.-Y. Lee, Y. Eryaman, J. Radder, A. Erturk, G. Metzger, P.-F. van de Moortele, K. Ugurbil, *et al.*, *A 16-channel transceiver loop+dipole antennas head array for human head imaging at 10.5 T*, in *2017 International Conference on Electromagnetics in Advanced Applications (ICEAA)* (IEEE, 2017) pp. 1649–1652.
- [37] B. R. Steensma, M. Luttje, I. J. Voogt, D. W. Klomp, P. R. Luijten, C. A. van den Berg, and A. J. Raaijmakers, *Comparing signal-to-noise ratio for prostate imaging at 7T and 3T*, *Journal of Magnetic Resonance Imaging* **49**, 1446 (2019).

- [38] R. Lattanzi and D. K. Sodickson, *Ideal current patterns yielding optimal signal-to-noise ratio and specific absorption rate in magnetic resonance imaging: computational methods and physical insights*, Magnetic resonance in medicine **68**, 286 (2012).
- [39] G. C. Wiggins, B. Zhang, R. Lattanzi, G. Chen, and D. Sodickson, *The electric dipole array: An attempt to match the ideal current pattern for central SNR at 7 Tesla*, in *Proceedings 20. Annual Meeting International Society for Magnetic Resonance in Medicine*, Vol. 20 (Melbourne, Australia, 2012) p. 0541.
- [40] A. J. Raaijmakers, M. Italiaander, I. J. Voogt, P. R. Luijten, J. M. Hoogduin, D. W. Klomp, and C. A. van Den Berg, *The fractionated dipole antenna: A new antenna for body imaging at 7 Tesla*, Magnetic resonance in medicine **75**, 1366 (2016).
- [41] A. Sadeghi-Tarakameh, A. Torrado-Carvajal, C. Ariyurek, E. Atalar, G. Adriany, G. J. Metzger, R. L. Lagore, L. DelaBarre, A. Grant, P.-F. V. de Moortele, K. Ugurbil, and Y. Eryaman, *Optimizing the topography of transmit coils for SAR management*, in *Proceedings 26. Annual Meeting International Society for Magnetic Resonance in Medicine*, Vol. 26 (Paris, France, 2018) p. 0297.
- [42] B. R. Steensma, I. J. Voogt, T. Leiner, P. R. Luijten, J. Habets, D. W. Klomp, C. A. van den Berg, and A. J. Raaijmakers, *An 8-channel Tx/Rx dipole array combined with 16 Rx loops for high-resolution functional cardiac imaging at 7 T*, Magnetic Resonance Materials in Physics, Biology and Medicine **31**, 7 (2018).
- [43] C. A. Balanis, *Antenna theory*, 3rd ed. (John Wiley & Sons, Inc., Hoboken, New Jersey, 2005).
- [44] L. Alon, R. Lattanzi, K. Lakshmanan, R. Brown, C. M. Deniz, D. K. Sodickson, and C. M. Collins, *Transverse slot antennas for high field MRI*, Magnetic resonance in medicine **80**, 1233 (2018).
- [45] I. Zivkovic, C. A. de Castro, and A. Webb, *Design and characterization of an eight-element passively fed meander-dipole array with improved specific absorption rate efficiency for 7 T body imaging*, NMR in Biomedicine , e4106 (2019).
- [46] A. Webb, *Dielectric materials in magnetic resonance*, Concepts in magnetic resonance part A **38**, 148 (2011).
- [47] W. M. Brink, *Dielectric shimming: exploiting dielectric interactions in High Field MRI*, Ph.D. thesis, Department of Radiology, Leiden University Medical Center (2016).
- [48] W. Teeuwisse, W. Brink, K. Haines, and A. Webb, *Simulations of high permittivity materials for 7 T neuroimaging and evaluation of a new barium titanate-based dielectric*, Magnetic resonance in medicine **67**, 912 (2012).
- [49] K. Koolstra, P. Börnert, W. Brink, and A. Webb, *Improved image quality and reduced power deposition in the spine at 3 T using extremely high permittivity materials*, Magnetic resonance in medicine **79**, 1192 (2018).

- [50] S. Rupprecht, C. T. Sica, W. Chen, M. T. Lanagan, and Q. X. Yang, *Improvements of transmit efficiency and receive sensitivity with ultrahigh dielectric constant (uHDC) ceramics at 1.5 T and 3 T*, Magnetic resonance in medicine **79**, 2842 (2018).
- [51] G. Carluccio, G. Haemer, M. Vaidya, S. Rupprecht, Q. Yang, and C. M. Collins, *SNR Evaluation for a high-permittivity dielectric helmet-shaped coil former for a 28 channel receive array*, in *Proceedings 26. Annual Meeting International Society for Magnetic Resonance in Medicine*, Vol. 26 (Paris, France, 2018) p. 4405.
- [52] K. Haines, T. Neuberger, M. Lanagan, E. Semouchkina, and A. Webb, *High Q calcium titanate cylindrical dielectric resonators for magnetic resonance microimaging*, Journal of Magnetic Resonance **200**, 349 (2009).
- [53] S. A. Aussenhofer and A. G. Webb, *Design and evaluation of a detunable water-based quadrature HEM11 mode dielectric resonator as a new type of volume coil for high field MRI*, Magnetic resonance in medicine **68**, 1325 (2012).
- [54] S. A. Aussenhofer and A. Webb, *High-permittivity solid ceramic resonators for high-field human MRI*, NMR in Biomedicine **26**, 1555 (2013).
- [55] T. P. O'Reilly, T. Ruytenberg, and A. G. Webb, *Modular transmit/receive arrays using very-high permittivity dielectric resonator antennas*, Magnetic resonance in medicine **79**, 1781 (2018).
- [56] T. Ruytenberg and A. G. Webb, *Design of a dielectric resonator receive array at 7 Tesla using detunable ceramic resonators*, Journal of Magnetic Resonance **284**, 94 (2017).
- [57] Z. Yu, X. Xin, and C. M. Collins, *Potential for high-permittivity materials to reduce local SAR at a pacemaker lead tip during MRI of the head with a body transmit coil at 3 T*, Magnetic resonance in medicine **78**, 383 (2017).
- [58] S. Aussenhofer and A. Webb, *An eight-channel transmit/receive array of TE01 mode high permittivity ceramic resonators for human imaging at 7 T*, Journal of Magnetic Resonance **243**, 122 (2014).

2

IMPROVEMENTS IN HIGH RESOLUTION LARYNGEAL MRI FOR PREOPERATIVE TLM AND RT CONSIDERATIONS IN EARLY LESIONS

**T. RUYTENBERG, B.M. VERBIST, J. VONK-VAN OOSTEN,
E. ASTREINIDOU, E.V. SJÖGREN AND A.G. WEBB**

As the benefits, limitations, and contraindications of transoral laser microsurgery (TLM) in glottic carcinoma treatments become better defined, pretreatment imaging has become more important. MRI is the preferred modality to image such laryngeal tumors, even though imaging the larynx using MRI can be difficult. The first challenge is that there are no commercial RF coils that are specifically designed for imaging the larynx. Second, motion in the neck region induced by breathing, swallowing, and vessel pulsation can induce severe image artifacts, sometimes rendering the images unusable. In this chapter, we design a dedicated RF coil array, which allows high quality high-resolution imaging of the larynx. In addition, we show that introducing respiratory-triggered acquisition improves the diagnostic quality of the images by minimizing breathing and swallowing artifacts. Together, these developments enable robust, essentially artifact-free images of the full larynx with an isotropic resolution of 1 mm to be acquired within a few minutes.

This chapter has been published in *Frontiers in Oncology* **8**, 216 (2018) [1].

2.1. INTRODUCTION

Early as well as moderately advanced laryngeal cancers are both highly treatable conditions, with the main treatment options consisting of transoral laser microsurgery (TLM), open partial laryngectomy (OPL), and radiotherapy (RT). All three modalities are used both in primary as well as recurrent disease, and treatment choice depends on the extent of the lesion as well as local therapeutic protocols and patient-specific factors such as age, comorbidity, and patient preference. Advances in therapy over the past two decades have enabled the relative benefits and limitations of the various treatment methods to be better understood. In particular, the indications for TLM have been more clearly defined [2].

The benefits of TLM include the low morbidity and short treatment time associated with endoscopic removal of the tumor. Functional outcomes are better than after OPL [3] and, for early lesions, they are comparable to RT [4]. In moderately advanced lesions, there is as of yet a lack of comparative evidence between TLM and RT concerning functional outcome to draw any definite conclusions [5, 6]. Finally, as TLM leaves all treatment options open after treatment, larynx preservation is generally higher than after RT [6–8]. However, as TLM has evolved, and moderately advanced tumors are increasingly being treated, tumor extension to certain subsites within the larynx have been associated with a higher risk of recurrence after TLM [2]. This has put an increasing requirement on high-quality radiological imaging to select those cases most suited for a transoral approach as opposed to open surgery or RT.

Imaging has become crucial for accurate evaluation, not only of tumor localization and size, but also for the involvement of subsites for which the suitability of TLM is still under debate, such as the pre- and posterior paraglottic space, the cricothyroid membrane, and the inner lamina of the thyroid cartilage [2]. Magnetic resonance imaging (MRI) is increasingly used to distinguish between tumor and edema or fibrosis [9]. In addition, in tumors in which surgery is indicated, imaging can help delineate tumor borders and predict the extent of the resection needed. This information can then be used in preoperative patient counseling regarding functional results, which are related to the extent of the resection. Finally, as the role of TLM expands, high quality imaging has become increasingly important in postoperative follow-up for early detection of submucosal recurrence, therefore, maintaining the possibility to perform open partial salvage surgery [2] or administering salvage RT. As a result, as treatment selection, patient counseling and follow-up monitoring for primary and recurrent early and moderately advanced laryngeal cancer evolves, the demand for high quality, robust, high resolution imaging has increased accordingly.

In tumors where RT is chosen as the preferred treatment of a glottic cancer, high-resolution imaging plays an equally important role. The goal of RT is to deliver a high dose to the tumor and minimize the dose to the surrounding healthy tissues in order to reduce vocal dysfunction, dysphagia, arytenoid edema, and carotid artery injuries [10]. This goal can only be achieved if the tumor is defined with high accuracy, i.e., when high

resolution imaging is available.

Historically, computed tomography (CT) has been the imaging modality of choice, particularly for RT [11]. CT is a robust modality due to very short acquisition times and high signal-to-noise ratio (SNR), but is limited in its utility since differentiation between healthy tissue and tumors can be difficult [11, 12]. Imaging the larynx using MRI became a useful alternative to CT in the late 1980s and early 1990s primarily due to the development of local surface coils, which enabled higher resolution imaging over a field-of-view, which could be localized to the larynx [13–16]. The lack of ionizing radiation, greater inter-tissue contrast, and multiplanar imaging capabilities were all advantages of MRI over CT, but long acquisition times limited the spatial resolution that could be achieved. Only when parallel imaging became available to reduce MRI acquisition times was it possible to achieve high spatial resolution in a realistic scanning time [17]. However, laryngeal imaging is still problematic. Current MRI protocols in early glottis carcinoma primarily use general purpose commercial local surface coils (which can also be combined with a head coil), or phased array head/neck coils [9, 18–24]. As these coils (for example two loops as shown in Figure 2.1A) are not specifically designed for laryngeal imaging, correct positioning centered on the vocal cords is critical, and needs to be done carefully and precisely by an experienced technician. Problems also arise with different-sized necks, which require a different physical separation of the coils. If the coils are placed too close together then they couple to one another, reducing the signal-to-noise, and also result in too small a field-of-view, a reduced penetration depth, and poor parallel imaging performance (including the possibility of fold-back artifacts): a typical example is shown in Figure 2.1B. If the loops are placed too far apart, or the patient has a large neck, signal voids within the larynx may occur, as shown in Figure 2.1C. In addition, the separate loops are prone to displacement during the examination, which increases the patient handling time and may induce patient discomfort.

Even if proper positioning of the coil has been performed, reconstructed images of the larynx often suffer from patient-related artifacts, which in some cases render images non-useful for diagnosis. One common cause is movement of the larynx during data acquisition, as shown in Figure 2.1D. Movement is unavoidable during the scanning protocol, as breathing causes the vocal cords to move. Swallowing, which moves the full larynx up to several centimeters in the feethead direction, may occur and can produce severe image artifacts. In addition, pulsation in the blood vessels in the neck commonly creates flow artifacts, which can extend into the larynx region, depending on the imaging protocol used.

In this chapter, we report on our work to improve the robustness and performance of high resolution laryngeal MRI. This consisted of two different aspects: first the design, construction, and testing of a flexible receive-array coil, which can adapt to different neck sizes, be worn comfortably by the patient, and enable robust parallel imaging for reduced scanning time. In addition, the array can be used for patients who have to be scanned in a RT fixation mask and it is, to our knowledge, the first time that a coil has been specifically designed to fit such fixation devices. In parallel, we investigated the use

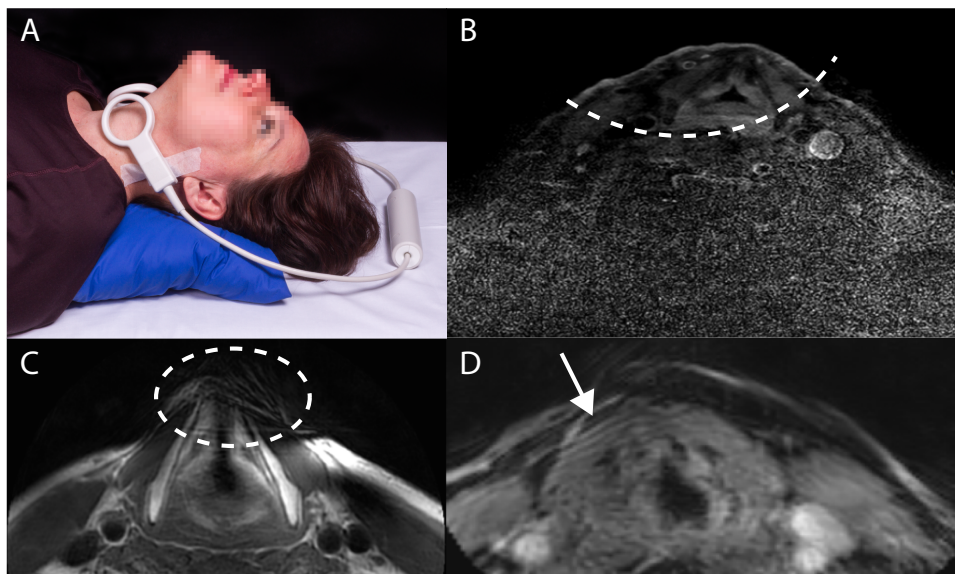


Figure 2.1: Illustrations of the challenges associated with current approaches to laryngeal magnetic resonance imaging. (A) Two individual, commercial circular receive coils, each with a diameter of 4 cm, are placed around the larynx. Positioning in this particular setup is critical for imaging the larynx and can be experienced as uncomfortable by the subject since the loops have to be held firmly in place with tape and/or velcro straps. Written informed consent was obtained from the subject for publication of this photo. (B) Images acquired with a limited penetration depth due to incorrect coil positioning, (C) images showing signal voids in the anterior part of the larynx due to incorrect coil positioning, and (D) images showing movement artifacts due to subject breathing.

of different scan protocols to reduce image artifacts associated with patient motion and pulsatile blood flow.

2.2. MATERIALS AND METHODS

2

2.2.1. COIL DEVELOPMENT

The dedicated radiofrequency (RF) coil receive array was designed to be flexible to accommodate different neck sizes and to have a high degree of isolation between individual elements to allow high acceleration factors while maintaining a high SNR [17, 25]. The number of coils in the receive array represents a compromise: a large number enables a high degree of acceleration, but increases the complexity of the networks required to decouple each of the coils and reduces the flexibility of the overall structure. In order to maintain a high degree of flexibility, as well as maintaining a high degree of decoupling under the different flexation angles required by different-sized necks, we constructed a one-dimensional four element array, as shown in Figure 2.2.

The dedicated coil is a four-element receive-only array and consists of four identical loops ($60\text{ mm} \times 60\text{ mm}^2$ each). Inter-element decoupling is achieved using a method termed induced current elimination [26] in combination with preamplifier decoupling, which uses a low impedance pre-amplifier acting as a current transformer [25]. This combination results in a coupling of less than 0.1% for neighboring elements and 1% for non-neighboring elements. This high level of decoupling is necessary to enable efficient and artifact-free parallel imaging performance [17]. Each coil is tuned at 128 MHz (3 T) and impedance matched to 50Ω using a lattice balun, which also suppresses common mode currents. Further common mode suppression was achieved by using floating cable traps [27]. Decoupling from the transmit body coil (detuning) is performed by a single active PIN diode trap in the each of the resonant loops. A fuse (250 mA very fast acting fuse; Littlefuse 0251.250MXL) is integrated into every loop to provide intrinsic safety in the case of any failure in detuning by disabling the coil in case of abnormal high currents.

The printed circuit board of the coil is etched on 0.125 mm thick FR4, which is flexible enough to be mounted on a curved 1 mm thick acrylic sheet to provide robustness to the coil as well as flexibility. The geometry of the coil is chosen to fit closely but comfortably around the neck and due to the flexibility of the coil, it easily accommodates different neck sizes. This also opens the possibility for the coil to fit on a RT mask, used to secure the head and neck during RT treatment.

2.2.2. PROTOCOL DEVELOPMENT

Magnetic resonance imaging scans were performed using a 3 T Philips Ingenia system, with the scan parameters shown in Table 2.1. In vivo scans were first performed on

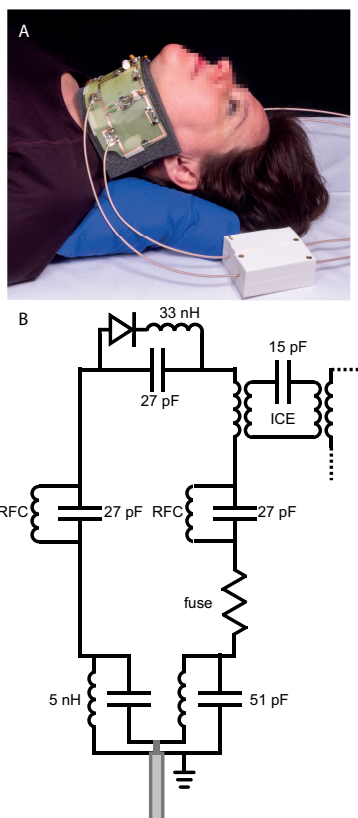


Figure 2.2: The dedicated larynx coil with the electronics visible (an enclosed version is used for in vivo scans). The coil is flexible and, therefore, adjustable to different neck sizes. The white boxes are floating cable traps, which prevent current from flowing on the outer shield of the connecting cables. Written informed consent was obtained from the subject for publication of this photo. (B) A schematic of the electrical circuit of each of the four loops constituting the coil. The individual loops are decoupled from the neighboring elements using an induced current elimination (ICE) circuit. Radiofrequency chokes (RFCs) are used to allow a DC current path to turn on the PIN diodes to isolate the receive coils from the transmit body coil.

Table 2.1: Scan parameters used for volunteer and patient studies.

	T1-weighted TSE	T1-weighted TSE (SPIR fat suppressed)	T2-weighted Dixon TSE	T2-weighted Dixon TSE	DWI
TE/TR (ms)	5.9/725	5.9/649	100/4680	60/2410	51/2038
Scan plane	transversal	transversal	transversal	coronal	transversal
Voxel size (mm ³)	1.0 × 1.0 × 1.0	1.0 × 1.0 × 1.0	1.0 × 1.0 × 1.0	0.65 × 0.81 × 1.5	3.0 × 3.0 × 3.0
Field of view (mm ³)	200 × 200 × 40	200 × 200 × 40	200 × 180 × 40	200 × 200 × 60	108 × 280 × 198
Phase direction	anterior-posterior	anterior-posterior	anterior-posterior	right-left	anterior-posterior
Acceleration factor	3.0	3.0	1.5 ²⁾	2.3	3.0
Averages	1	1	2	1	1
Total duration ¹⁾ (s)	189	216	253	54	168

¹⁾As all scans are respiratory triggered, scan time is dependent on the breathing pattern of the subject and the times shown are based on a breathing rate of once every 7 seconds. TSE (turbo-spin echo), DWI (diffusion weighted imaging), SPIR (Spectral Presaturation with Inversion Recovery).

²⁾An acceleration factor of 1.5 was used during the scans of the two patient cases described in the results section of this paper. Since that time, the protocol has been changed such that all transversal T2-weighted Dixon TSE scans are performed using acceleration factors of 3.0, reducing scan time to 126 seconds.

healthy volunteers. The local medical ethics committee approved all studies, and informed consents were obtained from all volunteers prior to the MR scan.

The four-channel phased array receive coil is interfaced to the scanner through a dedicated conversion box. During all scans, the commercial posterior array coil, which is built into the patient bed was electronically disconnected. In order to assess the performance of the receive coil array, scans on a cylindrical saline phantom (12 cm diameter) representing the neck were performed. The maximum acceleration factor that results in artifact-free images was determined from these phantom scans. Acceleration factors of between 2 and 4 in either the anteriorposterior or rightleft directions showed that fold-over artifacts at a factor of three are present but do not fold-in over the region of the larynx.

In order to address movement artifacts, respiratory-triggered scans were implemented, meaning that images are only obtained during a limited portion of the breathing cycle (in this case during exhaling), ensuring a stable position of the larynx during data acquisition. The respiratory trigger was applied using a belt on the abdomen, which triggered 500 ms after the initial stage of exhalation. Interestingly, since breathing and swallowing are physiologically linked (swallowing often occurs after exhaling), the use of respiratory-triggered scans also prevents swallowing-induced artifacts during image acquisition.

With respect to reducing image artifacts due to pulsatile blood flow in the arteries, we determined that implementing spatial saturation pulses caudal to the larynx did not result in a significant decrease in pulsation artifacts, and so were not used. Instead, to prevent pulsation artifacts falling within the larynx, the phase encoding direction was chosen to be in the anteriorposterior direction [24] for all transversal scans. For coronal scans, the anteriorposterior direction represents the slice-select direction for two-dimensional scans. The feethead direction would be preferred for these scans, however, due to the geometry of the RF coil array acceleration cannot be obtained in this phase encoding direction. Rightleft phase encoding is, therefore, the only possible phase encoding direction for coronal slices. This can sometimes result in pulsatile artifacts in the posterior part of the larynx.

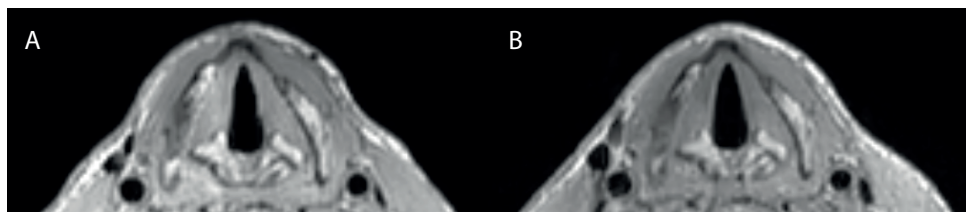


Figure 2.3: Respiratory triggered T1 TSE sequence (1 mm isotropic voxel size) with parameters as in Table 2.1. (A) Shows an image at the level of the vocal cords made with the two loops setup (as in Figure 2.1A) and at the maximum acceleration factor of 2.0: total scan time 234 s. (B) Shows an image at the same level made with the dedicated coil and an acceleration factor of 3.0: total scan time 189 s.

2.3. RESULTS

2.3.1. HEALTHY VOLUNTEERS

A comparison between the setups shown in Figure 2.1A (two commercial loops) and Figure 2.2A (dedicated coil) is shown in Figure 3. The scan with the loops placed on a cooperative volunteer was acquired with an acceleration factor of two (the maximum achievable factor for a two-element coil), while the scan with the dedicated coil was performed with an acceleration factor of three. The image quality between the two setups is very similar (when the two commercial loops are perfectly positioned), but the scan with the dedicated coil could be performed with a 33% reduction in scan time. The images show that the dedicated coil outperforms the commercially available setup even under ideal scanning conditions.

Figure 2.4 shows a comparison of images acquired with and without respiratory triggering. Respiratory triggering obviously increases the total imaging time, but the acceleration factor of three using the dedicated coil array reduces the scan time to 3 min and results in images without breathing and swallowing motion artifacts while at the same time also improving general image quality.

With the dedicated larynx coil, the entire length of the larynx can be covered and also the penetration depth is more than sufficient for imaging the full larynx. In total, 11 volunteers have been scanned with this setup, showing similar image quality for all volunteers. An example of the field of view is shown in Figure 2.5.

2.3.2. PATIENT SCANNING

After scanning healthy volunteers for protocol optimization, scans were performed on two patients with suspected tumor recurrence after treatment. The full scan protocol for patients includes a transversal T1 TSE, transversal and coronal T2 TSE Dixon, transversal DWI sequence before gadolinium being administered and a set of transversal T1 TSE

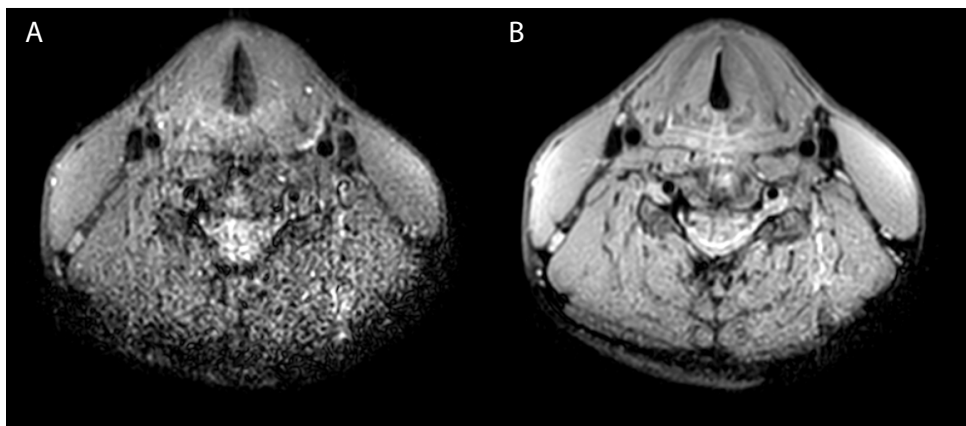


Figure 2.4: T1 TSE multi-slice sequence (transversal) at 1.0 mm isotropic resolution with SPIR fat suppression (scan parameters in Table 2.1) (A) without respiratory trigger, duration 57 s, (B) with respiratory trigger, duration 216 s. Triggering mitigates breathing and swallowing motion artifacts and increases image quality.

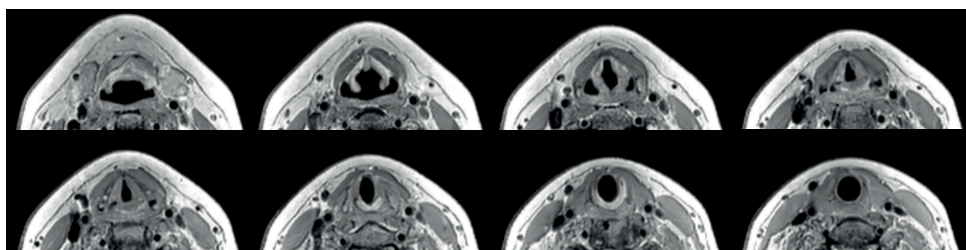


Figure 2.5: T1 TSE 1.0 mm isotropic scan with parameters as in Table 2.1. A selection of eight out of 40 slices ranging from aryepiglottic fold to subglottis on a healthy volunteer showing depth of penetration far beyond the larynx.

scans with SPIR (spectral presaturation with inversion recovery) fat suppression after gadolinium administration. This protocol takes less than 30 min.

2

PATIENT CASE 1

A 64-year-old male patient presented with a carcinoma of the left vocal cord with involvement of the anterior commissure and the anterior part of the contralateral vocal cord (T1b). Because of limited endoscopic exposure of the larynx, TLM could not be performed and the patient was treated with RT (25 fractions of 2.4 Gy each). Due to anxiety disorder, the patient refused flexible laryngoscopy during follow-up. For further surveillance, an MRI examination of the larynx was requested 8 months after irradiation. A subsection of the images acquired using the new coil and imaging protocols are shown in Figure 6. On T2-weighted images without and with fat suppression increased signal intensity was seen in both vocal cords and an area with intermediate signal on the surface of the left vocal cord (Figures 2.6A,B). On DWI, the T2 hyperintense areas showed no diffusion restriction, corresponding to inflammatory edema. DWI showed diffusion restriction in the superficial portion of the left vocal cord, compatible with submucosal recurrence (Figures 2.6C,D). In this patient, slowly increasing enhancement was seen and in tumor recurrence enhancement has been reported to be variable [9] (Figures 2.6E,F). Histopathological examination of biopsy specimens from the left vocal cord confirmed the presence of squamous cell carcinoma.

PATIENT CASE 2

During follow-up of an 82-year-old male patient, who underwent RT for a T2 glottic carcinoma of the right vocal cord 1 year previously with sub- and supraglottic extension, an ulceration suggestive of tumor recurrence was detected. The patient was referred for imaging to evaluate the depth of extension. Figure 2.7 shows four scans used for assessment using the new receive coil array and respiratory-triggered scans. Overall, the scans revealed a paramedian position of the right vocal cord and widening of the space between the thyroid cartilage and arytenoid. On the T2-weighted images, hyperintense signal is seen in the posterior portion of the vocal cord and in the posterior paraglottic space. This area showed enhancement, but no diffusion restriction. This MRI pattern is compatible with inflammatory changes or edema secondary to radiation therapy. Examination under anesthesia was performed and a biopsy of the superficial ulceration was taken. The underlying thyroarytenoid muscle appeared free of tumor. Pathologic exam confirmed a superficial tumor recurrence.

2.4. DISCUSSION

Early and moderately advanced laryngeal carcinoma are well treatable diseases by the main treatment modalities of TLM, OPL, and RT, all of which have their relative bene-

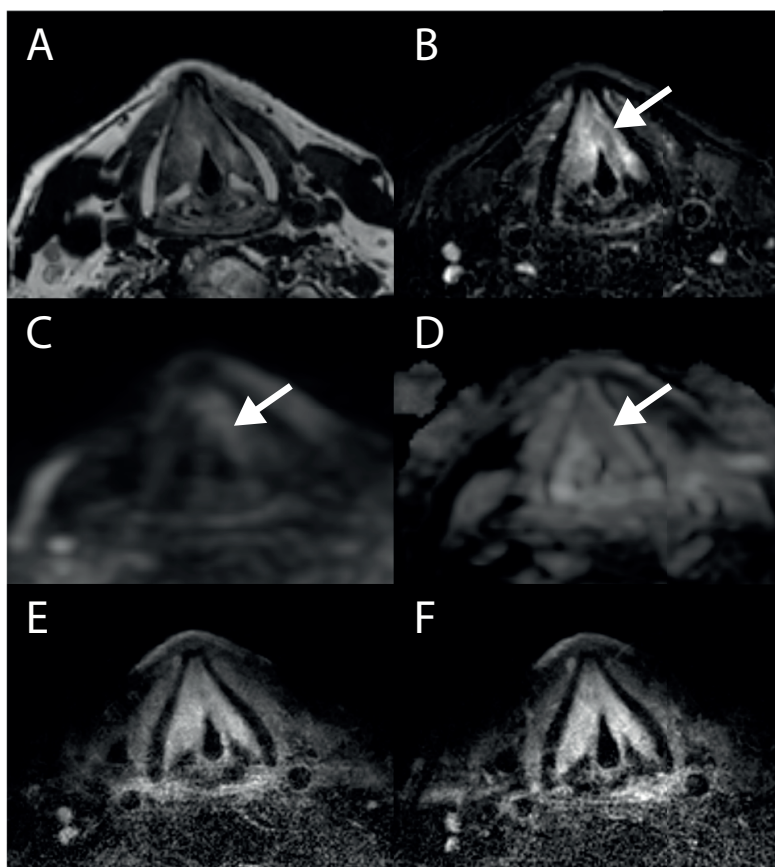


Figure 2.6: Magnetic resonance imaging scans 8 months after radiation therapy for a T1b glottis carcinoma. Increased signal intensity on T2-weighted scans without (A) and with (B) fat suppression in both vocal cords, together with the absence of diffusion restriction on DWI/ADC (C,D) is compatible with posttreatment edema. A biopsy in the superficial area corresponding to intermediate signal on T2 and diffusion restriction on the left vocal cord revealed tumor recurrence. Contrast-enhanced T1-weighted scans at two different time points show gradual enhancement (E,F).

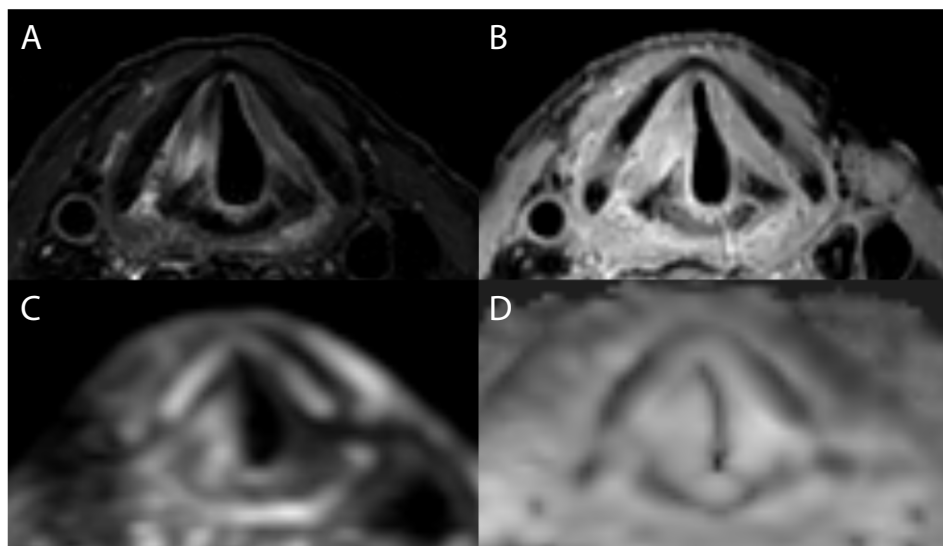


Figure 2.7: Laryngeal magnetic resonance imaging of a patient with superficial recurrence after radiotherapy of an early glottis carcinoma: high signal intensity in the right vocal cord and posterior paraglottic space on T2 (A) combined with a high signal intensity on both DWI (C) and ADC (D) is compatible with post irradiation edema and rules out deep tumor extension. There is diffuse enhancement on contrast enhanced T1 with fat suppression (B).

fits and limitations. In choosing and administering the most suitable treatment option for the individual patient, there are increasing demands for high quality imaging to: (1) assess image-based factors that determine the relative suitability for the different treatment modalities, (2) distinguish edema from tumor tissue, (3) predict the extent of the resection needed and the functional consequences, (4) identify early submucosal recurrence, and (5) improve tumor delineation in highly focused RT strategies. Key factors to obtain these high quality, artifact-free MR images of the glottis are to have a coil with high local sensitivity and to perform data acquisition with protocols, which reduce any motion-induced imaging artifacts. Reviewing previous literature, most groups use commercial general purpose surface coils. 3D gradient echo T1 sequences with fat suppression (for example, volumetric interpolated breath-hold examination) can be obtained with submillimeter voxels in cooperative patients [9, 19, 21]. For TSE sequences, slice thicknesses of 35 mm are chosen to reduce noise and acquisition time [12, 18, 19, 21–24].

Our main aim in this work is to improve on these previously reported scan protocols, particularly with respect to reduced slice thickness in TSE sequences. In order to produce artifact-free images, respiratory-triggered sequences were employed, which intrinsically increases the image acquisition time compared to non-triggered sequences. In order to at least partially compensate for this, an RF coil with high parallel imaging performance needed to be designed, which can be achieved by fabricating a coil with multiple individ-

ual elements. Many design criteria had to be taken into account and multiple prototypes have been built. The coil had to be flexible and fit many different neck-sizes, while being robust to ensure that soldering of the electronic components was not compromised under flexation. With the final design consisting of four channels, it is able to scan fast with an acceleration factor of three and allows for imaging with adequate SNR using a slice thickness of only 1 mm and a voxel size of 1 mm³.

Having obtained considerable experience in scanning both healthy volunteers and patients using the dedicated larynx coil and respiratory-triggered acquisitions, we anticipate that many aspects of image acquisition are worth pursuing to improve the efficiency of data acquisition. For example, we have seen that some sequences do not fully use the available acquisition time during the exhalation. This unnecessarily lengthens these scans by requiring more breathing cycles for data acquisition. Other methods to obtain faster scans, other than parallel imaging, such as compressed sensing [28] have not yet been implemented and can result in substantial scan duration reduction.

In addition, it should be noted that the use of a respiratory trigger also creates extra constraints and challenges. For example, it requires the subject to have a regular breathing pattern that is not too slow, as a slow breathing pattern will slow down acquisition and lengthen the scans. Furthermore, when performing dynamic contrast enhanced scans, due to the lengthening of the scans with the respiratory trigger, early contrast enhancement may be missed. These scans should, therefore, not be performed using a trigger. A last point is the fact that we have initially chosen the 1.0 mm isotropic resolution for most scans in order to be able to easily reslice in any given direction. This reslicing has not always been successful, as very slight displacement between the slices is observed originating from some residual motion, resulting in staircasing of anatomical boundaries when performing multi-slice 2D acquisitions. For improving the performance of coronal scans, a coil with a higher spatial encoding power in the feethead direction would be beneficial in order to obtain a better acceleration performance.

The dedicated coil has also been designed with integration with RT in mind. Patients receiving RT for laryngeal tumors are fixated in a customized individual mask. Fixation of the patient ensures treatment delivery reproducibility, as RT is delivered not in one but in many separate fractions. Because of the required reproducibility, the CT treatment planning is also done in a mask, as should be any diagnostic MR for RT purposes to allow for accurate image registration. In this way, the advantages of tumor delineation for RT based on a high-resolution MRI are fully utilized [29]. Accurate tumor delineation is the first step of the RT process for a highly focused dose delivery, which is critical when aiming for voice preservation and less side effects such as dysphagia, xerostomia, or stroke related to the dose received by the carotid arteries. Our coil is the first dedicated laryngeal coil, to our knowledge, which has been designed to fit a RT mask [24].

2.5. CONCLUSION

The developed dedicated larynx coil and scan protocols allow for high resolution imaging (1.0 mm isotropic for TSE sequences) of the larynx, without being affected by breathing or swallowing artifacts. The coil allows efficient parallel imaging, which is used to speed up data acquisition. Furthermore, the coil is flexible and, therefore, easily accommodates different neck sizes. Additionally, the short total protocol time for patients (30 min maximum) and the fact that they can continue breathing and swallowing during the scans, reduces the burden of these scans for patients. We anticipate that this improved image quality will lead to better treatment planning and counseling in patients with laryngeal tumors.

2.6. ACKNOWLEDGMENTS

The authors would like to thank Paul W. de Bruin for setting up the initial scan protocols and for his survey on different hardware setups for imaging the larynx. This work was supported by The Netherlands Organization for Scientific Research, domain Applied and Engineering Sciences under grant number 13783.

REFERENCES

- [1] T. Ruytenberg, B. M. Verbist, J. Vonk-van Oosten, E. Astreinidou, E. V. Sjögren, and A. G. Webb, *Improvements in high resolution laryngeal magnetic resonance imaging for preoperative transoral laser microsurgery and radiotherapy considerations in early lesions*, *Frontiers in oncology* **8**, 216 (2018).
- [2] G. Peretti, C. Piazza, F. Mora, S. Garofolo, and L. Guastini, *Reasonable limits for transoral laser microsurgery in laryngeal cancer*, *Current opinion in otolaryngology & head and neck surgery* **24**, 135 (2016).
- [3] G. Peretti, C. Piazza, F. Del Bon, R. Mora, P. Grazioli, D. Barbieri, S. Mangili, and P. Nicolai, *Function preservation using transoral laser surgery for T2–T3 glottic cancer: oncologic, vocal, and swallowing outcomes*, *European Archives of Oto-Rhino-Laryngology* **270**, 2275 (2013).
- [4] E. V. Sjögren, M. A. van Rossum, T. P. Langeveld, M. S. Voerman, V. A. van de Kamp, M. O. Friebe, R. Wolterbeek, and R. J. B. de Jong, *Voice outcome in T1a midcord glottic carcinoma: laser surgery vs radiotherapy*, *Archives of Otolaryngology–Head & Neck Surgery* **134**, 965 (2008).
- [5] Y. van Loon, E. V. Sjögren, T. P. Langeveld, R. J. Baatenburg de Jong, J. W. Schoones, and M. A. van Rossum, *Functional outcomes after radiotherapy or laser surgery in early glottic carcinoma: a systematic review*, *Head & neck* **34**, 1179 (2012).
- [6] M. Hendriksma, B. J. Heijnen, and E. V. Sjögren, *Oncologic and functional outcomes of patients treated with transoral CO₂ laser microsurgery or radiotherapy for T2 glottic carcinoma: a systematic review of the literature*, *Current opinion in otolaryngology & head and neck surgery* **26**, 84 (2018).
- [7] M. L. Schrijvers, E. L. van Riel, J. A. Langendijk, F. G. Dikkers, E. Schuurin, J. E. van der Wal, and B. F. AM van der Laan, *Higher laryngeal preservation rate after CO₂ laser surgery compared with radiotherapy in T1a glottic laryngeal carcinoma*, *Head & Neck: Journal for the Sciences and Specialties of the Head and Neck* **31**, 759 (2009).
- [8] V. Mahler, M. Boysen, and K. Brøndbo, *Radiotherapy or CO₂ laser surgery as treatment of T 1a glottic carcinoma?* *European Archives of Oto-Rhino-Laryngology* **267**, 743 (2010).
- [9] M. Ravanelli, D. Farina, P. Rizzardi, E. Botturi, P. Prandolini, S. Mangili, G. Peretti, P. Nicolai, and R. Maroldi, *Mr with surface coils in the follow-up after endoscopic laser resection for glottic squamous cell carcinoma*, *Neuroradiology* **55**, 225 (2013).
- [10] S. O. Osman, E. Astreinidou, H. C. de Boer, F. Keskin-Cambay, S. Breedveld, P. Voet, A. Al-Mamgani, B. J. Heijmen, and P. C. Levendag, *IMRT for image-guided single vocal cord irradiation*, *International Journal of Radiation Oncology* Biology* Physics* **82**, 989 (2012).

- [11] V. Grégoire, M. Evans, Q.-T. Le, J. Bourhis, V. Budach, A. Chen, A. Eisbruch, M. Feng, J. Giralt, T. Gupta, *et al.*, *Delineation of the primary tumour clinical target volumes (CTV-P) in laryngeal, hypopharyngeal, oropharyngeal and oral cavity squamous cell carcinoma: AIRO, CACA, DAHANCA, EORTC, GEORCC, GORTEC, HKN-PCSG, HNCIG, IAG-KHT, LPRHHT, NCIC CTG, NCRI, NRG Oncology, PHNS, SBRT, SOMERA, SRO, SSHNO, TROG consensus guidelines*, *Radiotherapy and Oncology* **126**, 3 (2018).
- [12] M. Ravanelli, G. M. Agazzi, D. Farina, and R. Maroldi, *New developments in imaging of laryngeal cancer*, *Current Otorhinolaryngology Reports* **5**, 49 (2017).
- [13] J. Castelijns, J. Doornbos, J. B. Verbeeten, G. Vielvoye, and J. Bloem, *MR imaging of the normal larynx*. *Journal of computer assisted tomography* **9**, 919 (1985).
- [14] H. D. Curtin, *Imaging of the larynx: current concepts*. *Radiology* **173**, 1 (1989).
- [15] R. B. Lufkin and W. N. Hanafée, *Application of surface coils to MR anatomy of the larynx*, *American journal of roentgenology* **145**, 483 (1985).
- [16] C. B. McArdle, B. J. Bailey, and E. G. Amparo, *Surface coil magnetic resonance imaging of the normal larynx*, *Archives of Otolaryngology–Head & Neck Surgery* **112**, 616 (1986).
- [17] K. P. Pruessmann, M. Weiger, M. B. Scheidegger, and P. Boesiger, *SENSE: sensitivity encoding for fast MRI*, *Magnetic resonance in medicine* **42**, 952 (1999).
- [18] J. W. Casselman, *High-resolution imaging of the skull base and larynx*, in *Parallel Imaging in Clinical MR Applications* (Springer, 2007) pp. 199–208.
- [19] R. Maroldi, M. Ravanelli, and D. Farina, *Magnetic resonance for laryngeal cancer*, *Current opinion in otolaryngology & head and neck surgery* **22**, 131 (2014).
- [20] M. Becker, K. Burkhardt, P. Dulguerov, and A. Allal, *Imaging of the larynx and hypopharynx*, *European journal of radiology* **66**, 460 (2008).
- [21] L. Preda, G. Conte, L. Bonello, C. Giannitto, E. Tagliabue, S. Raimondi, M. Ansarin, L. De Benedetto, A. Cattaneo, F. Maffini, *et al.*, *Diagnostic accuracy of surface coil MRI in assessing cartilaginous invasion in laryngeal tumours: Do we need contrast-agent administration?* *European radiology* **27**, 4690 (2017).
- [22] E. Allegra, P. Ferrise, S. Trapasso, O. Trapuzzano, A. Barca, S. Tamburrini, and A. Garozzo, *Early glottic cancer: role of MRI in the preoperative staging*, *BioMed research international* **2014** (2014).
- [23] E. A. Jager, N. Kasperts, J. Caldas-Magalhaes, M. E. Philippens, F. A. Pameijer, C. H. Terhaard, and C. P. Raaijmakers, *GTV delineation in supraglottic laryngeal carcinoma: interobserver agreement of CT versus CT-MR delineation*, *Radiation Oncology* **10**, 26 (2015).

- [24] G. M. Verduijn, L. W. Bartels, C. P. Raaijmakers, C. H. Terhaard, F. A. Pameijer, and C. A. van den Berg, *Magnetic resonance imaging protocol optimization for delineation of gross tumor volume in hypopharyngeal and laryngeal tumors*, International Journal of Radiation Oncology* Biology* Physics **74**, 630 (2009).
- [25] P. B. Roemer, W. A. Edelstein, C. E. Hayes, S. P. Souza, and O. M. Mueller, *The NMR phased array*, Magnetic resonance in medicine **16**, 192 (1990).
- [26] X. Yan, J. C. Gore, and W. A. Grissom, *New resonator geometries for ICE decoupling of loop arrays*, Journal of Magnetic Resonance **277**, 59 (2017).
- [27] D. Seeber, J. Jevtic, and A. Menon, *Floating shield current suppression trap*, Concepts in Magnetic Resonance Part B: Magnetic Resonance Engineering: An Educational Journal **21**, 26 (2004).
- [28] M. Lustig, D. Donoho, and J. M. Pauly, *Sparse MRI: The application of compressed sensing for rapid MR imaging*, Magnetic Resonance in Medicine: An Official Journal of the International Society for Magnetic Resonance in Medicine **58**, 1182 (2007).
- [29] S. Hanvey, M. McJury, L. M. Tho, M. Glegg, M. Thomson, D. Grose, A. James, M. Rizwanullah, C. Paterson, and J. Foster, *The influence of MRI scan position on patients with oropharyngeal cancer undergoing radical radiotherapy*, Radiation Oncology **8**, 129 (2013).

3

SHIELDED-COAXIAL-CABLE (SCC) COILS AS RECEIVE AND TRANSCIVE ARRAY ELEMENTS FOR 7T HUMAN MRI

T. RUYTENBERG, A.G. WEBB AND I. ZIVKOVIC

The performance of shielded-coaxial-cable (SCC) coils as elements for multi-channel receive-only and transceive arrays for 7 tesla human MRI were compared with equivalently-sized conventional loop coils. These SCC coils consist of a coaxial loop with interrupted central conductor at the feed-point side and an interrupted shield at the opposite point. Inter-element decoupling, transmit efficiency, and sample heating were compared with results from conventional capacitively-segmented loop coils. Three multi-channel arrays were constructed and their inter-element decoupling was characterized via measured noise correlation matrices and additionally under different flexing conditions of the coils. The measured and simulated B_1^+ maps of both SCC and conventional loops were very similar. For all the arrays constructed, the inter-element decoupling was much greater for the SCC elements than the conventional ones. Even under high degrees of flexion, the coupling coefficients were lower than -10 dB, with a much smaller frequency shift than for the conventional coils. This makes them suitable for the construction of size adjustable arrays.

3.1. INTRODUCTION

Transceive and transmit/receive arrays are commonly used in ultra-high field (>3 T) MRI since they can be used for B_1 -shimming [2–6] as well as accelerated acquisitions using either SENSE (Sensitivity Encoding) or GRAPPA (Generalized Autocalibrating Partially Parallel Acquisition) [7, 8] [6, 7]. The major challenge is to minimize the coupling between individual elements of the array, particularly when they are placed close together. Various methods have historically been used including geometrical overlapping [9], transformers [10], capacitive/inductive networks [11–14] and passive resonators [15–17]. Each method can then be combined with impedance mismatching with the pre-amplifier for an additional 20–30 dB decoupling [18, 19]. More recently proposed decoupling paradigms include using an uneven distribution of electrical impedances around the length of the loop [20] and high impedance coils [21]. The decoupling technique described in [20] is based on the fine tuning of each coils capacitance distribution to balance magnetic and electric coupling such that they cancel each other. This technique requires a number of lumped elements whose value must be precisely calculated. The decoupling technique proposed in [21] is essentially based on an inverted pre-amplifier decoupling [9] where instead of high impedance at the feeding point (which suppresses current flow) there is a very low impedance at the feeding point. In [21] the loop is constructed from a coaxial cable with specific characteristic impedance with an interrupted central conductor at the feeding point side and interrupted shield on the opposite side. The authors note in their discussion that one limitation of this technique is that the maximum loop size decreases as a function of static field: at 7 T, the maximum diameter of the high impedance loop was noted to be 40 mm. A second limitation is that the coils can only be used as receive elements since their decoupling depends on pre-amplifiers.

In this chapter, we investigate the use of shielded-coaxial-cable (SCC) coils as elements of transceive and receive arrays. The SCC was first described and used by the amateur radio community [22]. The SCC has also been described very briefly in the NMR literature. In [23], a mathematical model that describes the resonance spectra of the SCC was developed, although no MR data were presented. In [24], the optimization of SCC quality-factor maximizations for spectroscopic applications at 1.5 T was studied, with the authors finding similar performance between the SCC and a conventional loop coil. As such the SCC is not a new principle in coil design, but its incorporation into transmit or receive arrays has not been described previously, especially with respect to the isolation properties between individual elements of an array. Given its mode of action, it would appear to have several desirable properties in terms of intrinsic isolation. Due to discontinuities in the shield, there is an RF potential difference along its length. In receive mode, the oscillating magnetic field excites current flow on the outer shield wall. Skin effects isolate the outer shield wall from the inner shield wall. The current on the outside of the shield produces a voltage across the open gap in the shield and this voltage excites current flow on the inner wall of the shield. In turn, the current on the inner wall creates current on the inner conductor through inductive field coupling. The reciprocal mechanism applies in transmission. The shield acts as an antenna while the inside of the loop is a simple transformer. Therefore, one can infer that the inter-element isola-

tion in an array might be considerably better than for a conventional loop coil, which we investigate in this work. In terms of operation at high frequency for in-vivo human use, the resonant frequency is defined by the length of the coaxial cable, which allows circular loops up to 100 mm in diameter to be formed at 7 T. It has also been shown in [25, 26] that introduction of multiple shield gaps or multiple turns can increase/decrease the resonant frequency of the SCC coil, so the loop diameter can be adjusted to the desired value for the particular field strength being used. The coaxial cable is flexible so the coil can conform to the geometry of the body part being imaged, similar to, for example, a liquid metal coil [27]. Finally, the design can be used in either receive-only or transceive arrays. The performance of a four-element receive-only array (knee) and two transceive arrays of eight (knee) and five (hand) elements were investigated via in-vivo imaging of healthy volunteers.

3.2. METHODS

3.2.1. COIL FABRICATION

Receive-only loops (Figure 3.1a) were made from 1.8 mm diameter flexible coaxial cable (G01132-06, Huber+Suhner, Switzerland) with a conventional pi-matching network with two 18 pF capacitors (Dalicap Co., Ltd., China) in the series arms and one 24 pF capacitor in the parallel one. An electrically floating copper shield was created on the back of the printed circuit board used for soldering the passive components in order to shield any stray RF field. Two PIN diodes (MA4P7441F-1091T, MACOM, USA) were used for detuning purposes and were connected between the inner conductor of the coaxial cable and the shield, at a position opposite from the feed point. The cable shield was interrupted at the top part of the loop (opposite from the feed point) while the inner conductor was interrupted at the bottom part. The resonance of the loop is largely determined by the total length of the coaxial-cable, as shown in equations 3.1 and 3.2 [25, 26]: the resonant condition occurs when the inductive reactance, X_L , is equal to the capacitive reactance, X_C .

$$X_L(\omega_0) = \omega_0 \mu_0 \frac{d_0}{2} \left[\ln \left(\frac{8d_0}{d_1} \right) - 2 \right] \quad (3.1)$$

$$X_C(\omega_0) = -Z_0 c \cot \left(\frac{\omega_0 l \sqrt{\epsilon_r}}{c_0} \right) \quad (3.2)$$

where d_0 is the coil diameter, d_1 is the cable diameter, l is the stub length between the inner and outer gaps of the coaxial cable, Z_0 is characteristic impedance of cable and ϵ_r is permittivity of the dielectric material inside the cable.

For performance comparison purposes, a circular SCC coil with diameter 100 mm was formed, as shown in Figures 3.1a and 3.1b. Conventional circular loops with a diameter

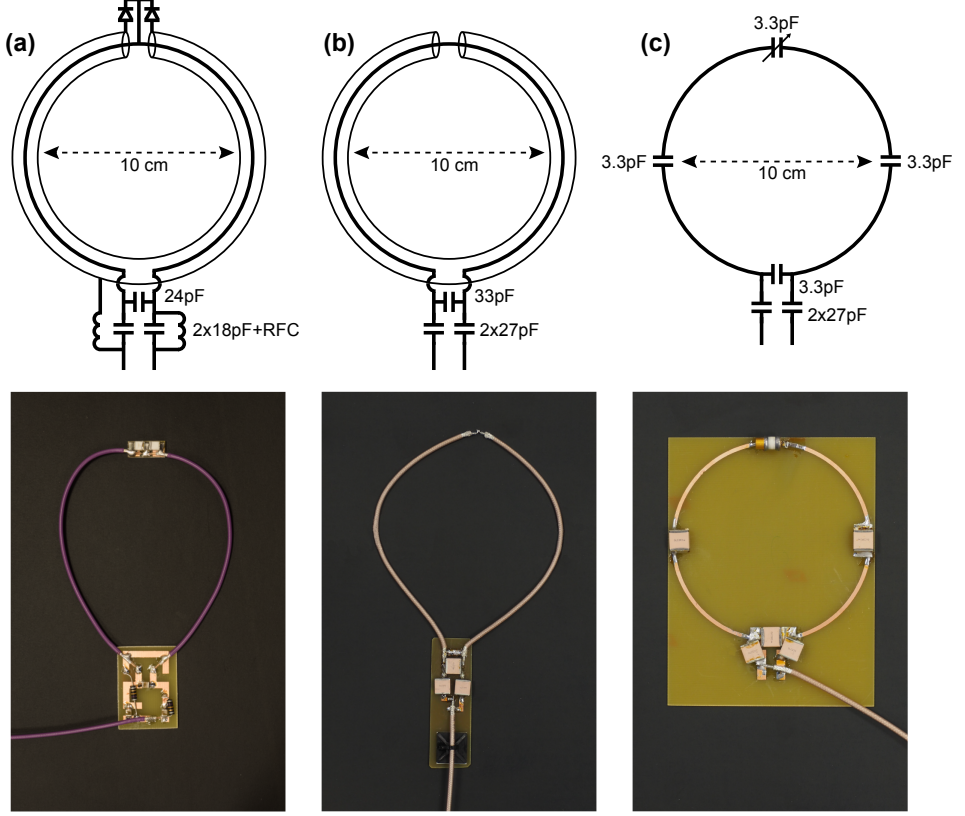


Figure 3.1: Schematics and photos of (a) receive-only coaxial loop coil, (b) transceive and (c) conventional coil.

of 100 mm were fabricated on an FR-4 substrate ($\epsilon_r = 4.3$, $\tan\delta = 0.025$, substrate thickness 1.5 mm) with three distributed capacitors (3.3 pF, Dalicap Co., Ltd., China), one variable tuning capacitor (connected in parallel) and two matching capacitors (connected in series, 27 pF), as shown in Figure 3.1c.

Elliptical transceive loops ($120 \times 60 \text{ mm}^2$, Figure 3.1b) were created using the same design methodology without the PIN diodes. A slightly thicker (3 mm diameter) coaxial cable (K_02252_D-08, Huber+Suhner, Switzerland) was used for the high transmit power. Two high-voltage-rated capacitors of 27 pF (7200 Volt, Dalicap Co., Ltd., China) were connected in series and one high-voltage-rated 33 pF capacitor was connected in parallel. The same floating shield was used as described above. For comparison with the transceive array an elongated loop made of 1 mm copper wire with four distributed capacitors (2.2 pF) and two matching capacitors (connected in series, 47 pF) was constructed. An eight-channel annular transmit/receive array with elliptical shielded loop coils placed immediately adjacent to one-another was designed to cover the full axial extent of the knee. The coils were positioned immediately adjacent to one another. A

second transceiver array consisting of five coil elements formed on an electrically insulating glove (rated 500 Volt, GLE36-00, Regeltex, France) was constructed for imaging the hand. As with the design presented for 3T imaging in [21] one coil was placed above each digit.

S-parameter measurements were performed using a Vector Network Analyser (TR1300/1, Copper Mountain Technologies, USA) and a rectangular tissue-mimicking phantom ($\epsilon_r = 50$ and $\sigma = 0.55$ S/m, $400 \times 400 \times 190$ mm³). A 1 cm thick foam spacer was placed between the coils and the phantom. The coupling coefficient between two loops (SCC and conventional) was measured while varying the amount of overlap from 0 mm to 40 mm. In a second experiment, three loops at various inter-coil separations (25% overlap, immediately adjacent, and spaced by one-half the loops diameter) were measured.

The unloaded Q (Q_{ul}) and loaded Q (Q_{lo}) values of a single conventional and SCC element were measured with a pick-up coil and a vector network analyzer.

The dependence of the coils resonant frequency on the coils geometry was also evaluated for both conventional and SCCs. The coils geometry was varied from circular (100×100 mm²) to elongated (60×150 mm²) shape and from flat to bent around a 120 mm diameter cylindrical phantom ($\epsilon_r = 50$ and $\sigma = 0.55$ S/m).

3.2.2. ELECTROMAGNETIC SIMULATIONS

Electromagnetic simulations were performed in CST Microwave Studio 2019 (CST Studio Suite, Computer Simulation Technology, Darmstadt, Germany). Simulations were first performed with a single antenna element on a square phantom (phantom properties: $\epsilon_r = 50$ and $\sigma = 0.55$ S/m) using the frequency domain solver with tetrahedral meshing, as hexahedral meshing is not able to properly mesh a curved coaxial cable. To evaluate the B_1^+ and SAR_{10g} efficiency of the single antenna, results were normalized to 1 W of accepted power. Subsequent in-vivo simulations using an eight element transmit array were performed using the voxel model Gustav (CST Studio Suite, Computer Simulation Technology).

3.2.3. MRI MEASUREMENTS

All MRI measurements were performed on a 7T Philips Achieva scanner, which uses low input impedance preamplifiers on the receive side with a value of roughly 2+5j Ohms.

For phantom experiments, a single transceiver loop and conventional loop were placed 1 cm above the rectangular phantom described previously. B_1^+ maps measured on a phantom were obtained using the Dual Refocusing Echo Acquisition Mode (DREAM) [28] sequence with the following parameters: field-of-view (FoV) = $400 \times 320 \times 25$ mm³, voxel size = $5 \times 5 \times 5$ mm³, slices = 5, tip angle = 10°, stimulated acquisition mode (STEAM)

angle = 50° , TE/TR = 1.97/15 ms, number of signal averages (NSA) = 1.

Thermometry measurements were performed on the same phantom using the transceive elongated SCC and conventional coils. These measurements were performed using the proton reference frequency method [29]. A 3D gradient-echo sequence was used for heating, and also for performing the thermal measurements [30]: TR/TE = 14/10 ms, FA = 100° , scan duration = 15 minutes. In order to induce measurable temperature changes the SAR limits of the scanner were disabled and the power absorbed by the sample was increased by applying a series of 100 kHz off-resonance pre-pulses during the imaging sequence (these far off-resonance pulses do not interfere with the imaging itself). Both coil elements were configured to transmit the same amount of RF power.

In order to determine how sensitive the coils are to the size of the object being imaged the four channel receive-only array was tested on three different sized phantoms with the following circumferences 290 mm, 370 mm and 410 mm. The coils were tuned for the 370 mm circumference phantom. The individual coil minor axis lengths corresponding to different phantom circumferences were 73 mm, 93 mm and 103 mm. Phantom images were obtained with a 3D T1-weighted gradient-echo sequence using the following parameters: TR/TE = 5.8/2.5 ms, FA = 10° , voxel size = $0.7 \times 0.7 \times 0.7 \text{ mm}^3$, NSA = 1.

For in-vivo experiments all volunteers signed an informed consent form, and the study was approved by the local medical ethics committee. Imaging using the four-element receive-only SCC array was performed on the knee of a healthy volunteer. A quadrature high-pass birdcage coil (Nova Medical) was used for transmit. In-vivo images were obtained with a 3D T1-weighted gradient-echo sequence using the following parameters: TR/TE = 5.8/2.5 ms, FA = 10° , voxel size = $0.7 \times 0.7 \times 0.7 \text{ mm}^3$, NSA = 1.

In-vivo measurements using the eight-element SCC transceive array and five-channel glove transceive SCC array were performed using a vendor-supplied multi-transmit system. For images of the knee, transmit phases were adjusted for excitation of the CP⁺ mode, and for images of the hand equal transmit phases were used for all channels. The knee images were obtained on four volunteers, with different body mass indices (BMIs), using a 3D T1-weighted gradient-echo sequence with the following parameters: TR/TE = 5.8/2.5 ms, FA = 10° , voxel size = $0.7 \times 0.7 \times 0.7 \text{ mm}^3$, no averaging. The circumferences of the volunteers knees were 370 mm, 390 mm, 400 mm and 430 mm. The minor axis lengths of the 8-channel flexible array elements varied from 46 mm to 54 mm. The hand images were obtained on two volunteers using a 3D T1-weighted gradient-echo sequence with the following parameters: TR/TE = 25/4.9 ms, FA = 25° , voxel size = $0.5 \times 0.5 \times 4.0 \text{ mm}^3$, no averaging and T1w TSE sequence with the following parameters: TR/TE = 23/631 ms, voxel size = $0.5 \times 0.5 \times 4.0 \text{ mm}^3$, NSA = 1.

3.3. RESULTS

3.3.1. COMPARISON OF CONVENTIONAL AND SCC COILS

Figure 3.2a depicts the S_{12} -parameters of a 100 mm diameter circular SCC and an equally-sized conventional loop coil as a function of overlap in a two-element array placed on the rectangular phantom. While the conventional loops show minimum coupling at 20 mm overlap as expected, the SCC loops have no sharp optimum value and have a higher decoupling for every degree of overlap/separation. In order to investigate next-neighbour coupling, Figure 3.2b shows the measured S-parameter matrix of three elements of circular SCCs and its conventional analogues. The measured inter-element coupling was in general lower for the SCCs compared to the conventional surface coils.

Figure 3.3 shows simulated and measured B_1^+ distributions and simulated surface current distributions on circular conventional and SCCs. Simulated and measured B_1^+ distributions are very similar for both SCC and conventional coil. There was around 15% lower B_1^+ efficiency of the SCC at superficial depths while at depths of ~50 mm and higher the efficiencies were comparable. The simulated surface current distributions show evenly distributed surface current magnitude on the conventional coil, while on the inner part of coaxial coil the surface current has its maximum at the bottom part of loop (around feeding point) and has variable magnitude at the top part (around shield gap point). The magnitude of the surface current distribution on the shield of the coaxial coil was almost one order of magnitude lower than the magnitude of the surface current on the conventional coil.

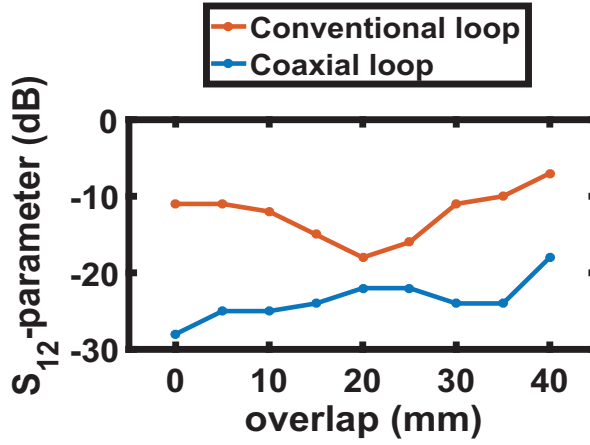
Figure 3.4 shows the measured resonant frequency shift when the coil geometry is changed from circular (100 mm×100 mm) to slightly-elongated (80 mm×130 mm) to elongated (60 mm×150 mm). The coils were initially tuned to resonate at 298 MHz for the circular geometry. The shifts in resonant frequency for the conventional coil were 2.1 MHz and 11.1 MHz (Figure 3.4b), respectively, whereas those for the SCC were 0.3 MHz and 1.5 MHz, respectively. Figures 3.4c and 3.4d show the resonant frequency shifts when the coils were bent around the cylindrical phantom. The resonant frequency shift of the conventional coil was 7 MHz while that of the SCC was 2.5 MHz.

Measured unloaded (Q_{ul})/loaded (Q_{lo}) Q factors of the conventional coil were 105/20 while those of the SCC were 100/60, corresponding to Q_{ul}/Q_{lo} ratios of 5.3 and 1.7.

3.3.2. RECEIVE-ONLY ARRAY – KNEE IMAGING

Figure 3.5a shows measured noise correlation matrices of the four channel receive-only SCC array on three different phantom circumferences – 290 mm (coils minor axis length was 73 mm), 370 mm (coils minor axis length was 93 mm) and 410 mm (loop diameter was 103 mm). The S_{11} of individual channels was tuned on the phantom with 370 mm

(a)



(b)

Measured S-parameters of 3×1 arrays

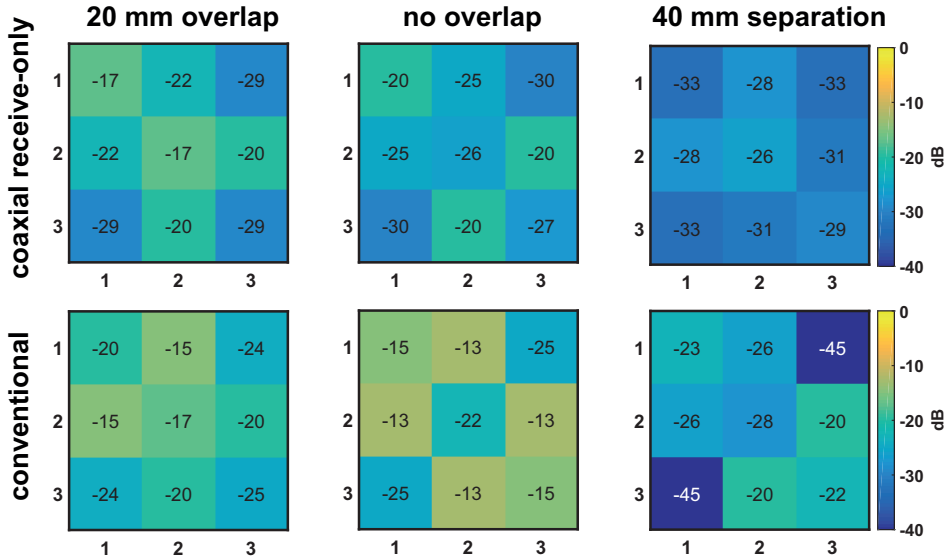


Figure 3.2: (a) S_{12} -parameters for two coils for both the SCC and conventional loop as a function of overlap. The loops have a diameter of 100 mm and were placed on a tissue-mimicking phantom. (b) Measured S -parameters of three SCCs (top row) and conventional loops (bottom row) placed on the phantom with +20 mm overlap (left column), immediately adjacent to one another (0% overlap, middle column) and 40 mm separation between elements (right column).

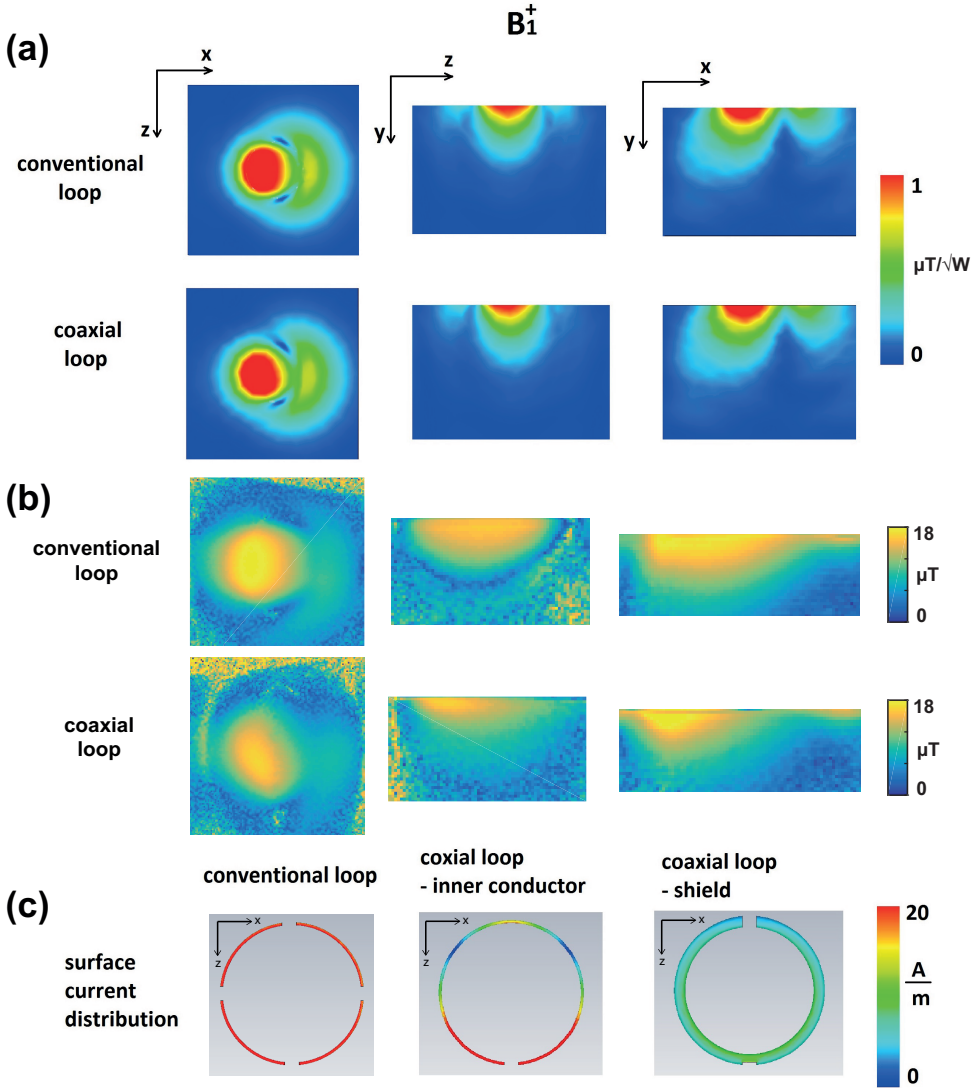


Figure 3.3: (a) Simulated B_1^+ distributions of conventional and coaxial loops, normalized to 1 W of accepted power. (b) Measured B_1^+ distributions of conventional and coaxial loops. (c) Surface current distributions on conductor of conventional loop (left), inner conductor of SCC (middle) and on shield of SCC (right).

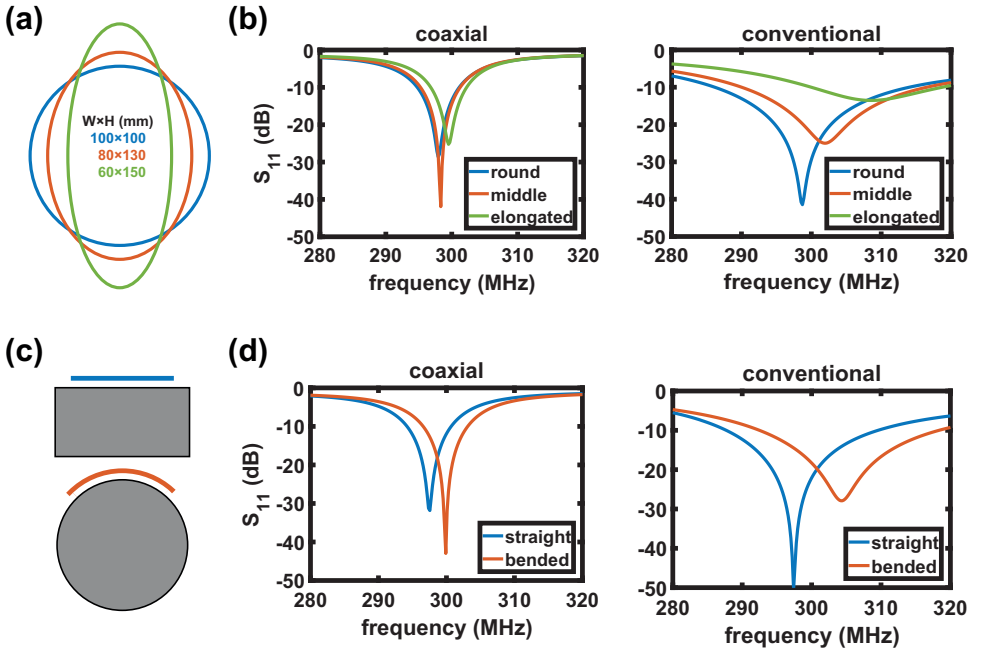


Figure 3.4: (a) Degree of elongation of the loops, starting from circular (diameter 100 mm), middle elongated (diameter 80 mm) and elongated (diameter 60 mm). (b) Measured S_{11} of SCC (left) and conventional (right) coils when the shape was changed from circular to elongated. The coils were initially tuned at circular shape. (c) Schematics of the coil position on a flat and cylindrical phantom. (d) Measured S_{11} of SCC (left) and conventional (right) coils when placed on a flat and bended on a cylindrical phantom. The coils were initially tuned at position on a flat phantom.

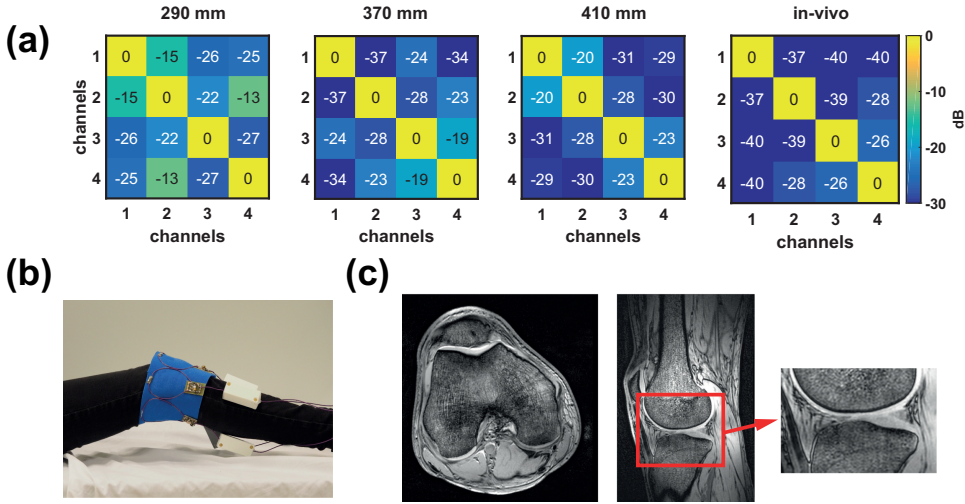


Figure 3.5: (a) Measured noise correlation matrices of the 4-channel receive array on phantoms of the following circumferences - 290 mm, 370 mm and 410 mm. The coils were tuned on a phantom with a circumference of 370 mm. Measured in-vivo noise correlation matrix. (b) Photograph of the in-vivo measurement setup consisting of four non-overlapped receive loops (a birdcage coil was used for transmit and is not shown on the image). (c) In-vivo images of the knee. A magnified image of the cartilage is shown to demonstrate the fine structure.

circumference. The highest measured coupling between the channels on a phantom with 290 mm circumference was -13 dB (S_{11} of individual channels of this array was -13 dB or better). The highest measured coupling between the channels on a phantom with 370 mm circumference was -19 dB (S_{11} of individual channels of this array was -20 dB or better). The highest measured coupling between the channels on a phantom with 410 mm circumference was -20 dB (S_{11} of individual channels of this array was -15 dB or better). The coil coupling between the elements in the in-vivo measurement was lower than -26 dB (S_{11} of individual channels was -20 dB or better). Figure 3.5b shows the measurement setup with four receive-only loops placed around the knee of a volunteer. The loops were placed immediately adjacent to one another. High resolution gradient-echo images were obtained in both sagittal and axial orientations using an isotropic voxel size of 0.7 mm^3 demonstrating excellent visualization of the cartilage and trabecular bone structure.

3.3.3. TRANSCIVE ARRAY – KNEE IMAGING

For a transceive array for knee imaging we constructed an eight-element SCC array, and in order for these to be accommodated around the knee the coils need to be elongated. Figure 3.6a and b show photographs of the elongated SCC and conventional coils, respectively. Figure 3.6d and e shows measured and simulated B_1^+ maps of a single elliptical transceiver SCC compared to the conventional elongated loop coil segmented by

four capacitors. Both loops were placed on the same phantom and imaged at the same time using individual channels of the multiple transmit setup to ensure that the same input power and imaging conditions are used. Both transverse and sagittal profiles are shown. The B_1^+ maps show very similar intensity profiles for the SCC and conventional loops, although it should be noted that the SCC acts as a slightly ($\sim 8\%$) shorter coil in the sagittal plane. Figure 3.6c shows B_1^+ profiles of SCC and conventional coils plotted along the central lines (red dashed line in Figure 3.6d). The B_1^+ efficiency of the conventional coil is slightly better than the efficiency of SCC at superficial depths. At depths ~ 50 mm and more the efficiency of the SCC becomes comparable or better than the efficiency of the conventional coil.

Figure 3.7a shows simulated SAR_{10g} of the elongated conventional and SCC coils. The results are very similar maximum SAR_{10g} of conventional coil was 1.28 W/kg and of SCC was 1.23 W/kg. Thermometry data of the conventional and SCCs are shown in Figure 3.7b. This data was corrected for any B_0 drift during the experiment. The acquired thermometry maps were normalized to the maximum temperature increase. The maximum temperature produced by the conventional coil was around 12% higher than the temperature produced by the SCC. Figure 3.7c shows maximum SAR_{10g} simulated by eight channel array of elongated coils placed around a knee of a voxel model. The maximum simulated SAR_{10g} was 2.5 W/kg.

Figure 3.8a shows measured noise correlation matrices of the eight channel SCC array placed around the knee for four different volunteers. The knee circumferences varied from 370 mm to 430 mm. The flexed single coil element minor axis length varied from 46 mm to 54 mm. The highest coupling coefficient was measured in Subjects 3 and 4 and was -10 dB. The other coupling coefficients were -14 dB and better. Figure 3.8b shows a photograph of the eight-channel elongated transceive array placed around the knee of a healthy volunteer. Both sagittal and axial images are shown (Figure 3.8c). Some shading at the centre of the image is evident in the images for which no post-processing correction has been applied.

3.3.4. TRANSCIVE ARRAY – HAND IMAGING

Figure 3.9 shows results from the five-channel glove transceiver array. The highest inter-element coupling was between elements 4 and 5 (-11 dB). Different hand sizes did not change the coils loading significantly. Figures 3.9c and d show fine bone structure visible on a single finger image with both gradient and spin echo sequences. S_{11} -parameters were measured also for different flexion angles of the glove (results not included) and the worst case showed only a 1-2 dB higher S_{11} value at maximum flexion.

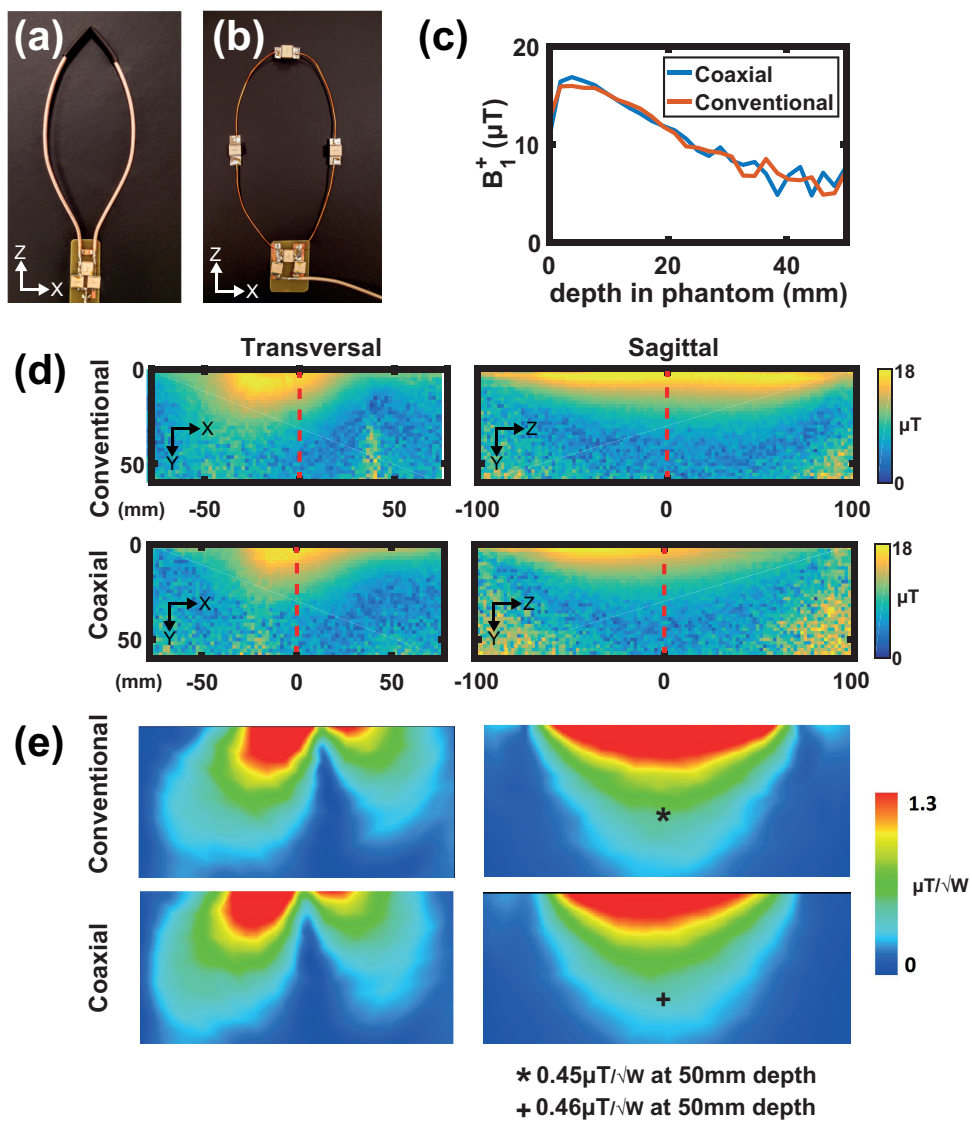


Figure 3.6: Photographs of a (a) SCC elongated loop and (b) conventional elongated loop. (c) Measured B_1^+ profile along the central axis of the antenna (red dashed line in (d)). (d) Measured transversal and sagittal B_1^+ maps of conventional and SCC coils. (e) Simulated transversal and sagittal B_1^+ maps of conventional and SCC coils.

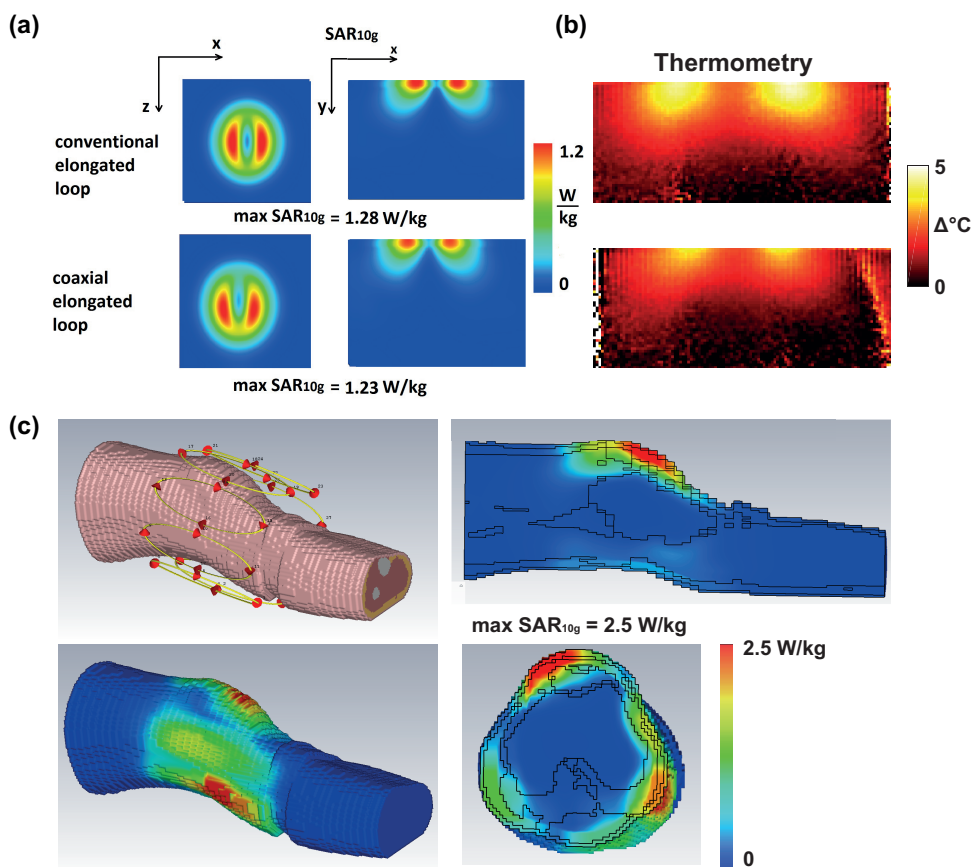


Figure 3.7: (a) Simulated SAR_{10g} of a single element on a phantom of conventional elongated (upper image) and coaxial elongated (lower image) coil. (b) Corresponding thermometry measurements of elongated conventional and coaxial coils, normalized to the maximum temperature. (c) Simulated SAR_{10g} on a voxel model.

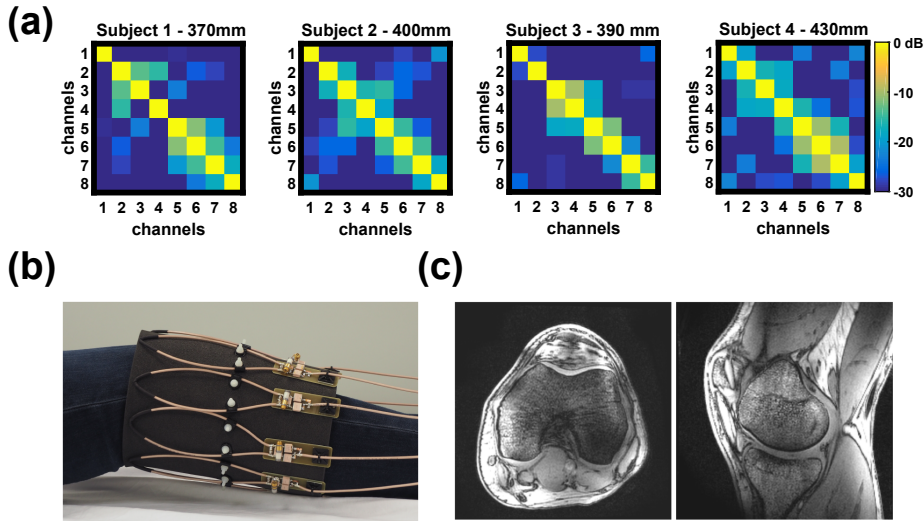


Figure 3.8: (a) Measured noise correlation matrices on four different subjects with different knee circumferences. (b) Photograph of the in-vivo measurement setup consisting of eight non-overlapped transceive loops. (c) In-vivo images of the knee.

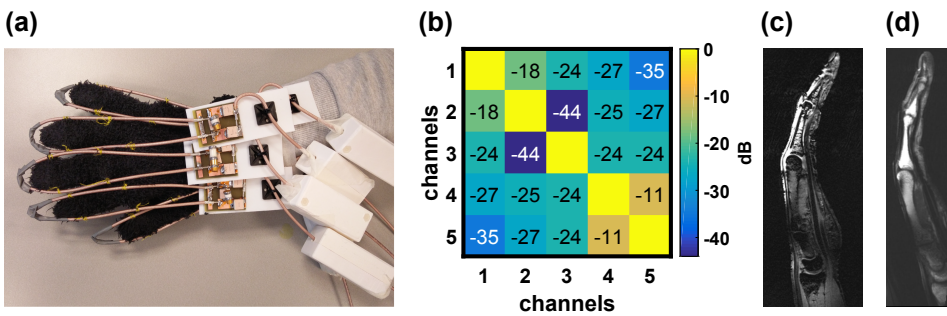


Figure 3.9: (a) Photograph of the in-vivo measurement setup consisting of five transceive loops attached to a glove. (b) In-vivo measured noise correlation matrix. In-vivo images of the hand in natural position showing a single finger in sagittal view using a (c) gradient and (d) spin echo sequence.

3.4. DISCUSSION

This chapter has demonstrated a simple method for constructing loop arrays with a high degree of inter-element decoupling using SCCs. In this design distributed lumped elements within the loop are not required. The concept is very similar to designs proposed in [21, 23, 24] and in [22] for low frequency amateur radio communications, and to the cross-over coil shown by Mispelter et al. [31] which has a slightly different configuration in which the inner conductors in the cross-over coil are cross-connected to the shield at the shield gap.

As shown by Avdievich et al. the magnetic coupling coefficient (k_m) of two loops (~100 mm diameter) at 300 MHz is very low [32]. The dominant coupling is therefore resistive (k_e) and occurs from coil-to-coil through the sample. Since the ratio of the unloaded-to-loaded Q-factor of the SCC is more than three times lower than that of the conventional coil (Q_{ul}/Q_{lo} of conventional coil was 5.3 and of SCC was 1.7), this implies lower coupling to the sample and lower inter-element coupling due to a lower k_e . This can further be explained as follows. The inductive E-field (produced by surface currents on the coil) induces eddy currents in the sample. Induced eddy currents in the sample produce a secondary E-field which induces currents back to the coil. The stronger the surface currents on the coil, the stronger the coupling (eddy currents) to the sample, which reflects as a lower Q-factor of the loaded conventional coil. The shield of the coaxial coil partially shields the surface currents on the inner conductor, such that the coupling to the sample is lower than the coupling of the conventional coil.

From the surface current distribution shown in Figure 3.3, the lowest current magnitude is on the shield of SCC (almost one order of magnitude lower than the surface current on conventional coil). The surface current distribution on inner conductor of the SCC and on conductor of conventional coil are of similar magnitude. Since the inner conductor of the SCC does not have distributed capacitors, wave effects are noticeable in the magnitude of the surface current.

From B_1^+ simulations and measurements it can be concluded that the conventional coil is more efficient element at superficial depths, while at depths of ~50 mm and more the efficiency of SCC becomes comparable or better than that of the conventional coil. The general B_1^+ distributions of both conventional and SCC show similar patterns, although the longitudinal B_1^+ coverage in the sagittal plane of the conventional coil is larger than the coverage of the SCC due to the lower current densities on a shield closer to the shield gap and on inner conductor of the SCC. From SAR_{10g} simulations and thermometry measurements it can also be concluded that an SCC and conventional coil induce similar electric fields in a conducting sample.

Results also showed that changing the shape from round to elongated or bending the coil element has a much smaller effect on the tuning and matching of the SCC than for the conventional coil.

3.5. CONCLUSION

Receive and transceive arrays of SCC elements showed a higher degree of intrinsic inter-element decoupling than conventional loops. This allows the simple construction of flexible multi-element arrays for high field MRI. The SCC can be used in a receive-only or in a transceive array. It should be possible to expand the application of the proposed coil concept for imaging body parts for which rigid coil design is not suitable, such as the larynx [33]. The SCC is also potentially useful as an array element in size-adjustable tight-fitting head arrays.

3.6. ACKNOWLEDGEMENTS

The authors would like to thank Wouter Teeuwisse for his help with in-vivo MR measurements. This work was made possible by NWO domain TTW under grant #13783 and European Research Council Advanced Grant (670629 NOMA MRI).

REFERENCES

- [1] T. Ruytenberg, A. Webb, and I. Zivkovic, *Shielded-coaxial-cable coils as receive and transceive array elements for 7T human MRI*, Magnetic resonance in medicine **83**, 1135 (2020).
- [2] W. Mao, M. B. Smith, and C. M. Collins, *Exploring the limits of RF shimming for high-field MRI of the human head*, Magnetic Resonance in Medicine: An Official Journal of the International Society for Magnetic Resonance in Medicine **56**, 918 (2006).
- [3] R. Abraham and T. S. Ibrahim, *Proposed radiofrequency phased-array excitation scheme for homogenous and localized 7-Tesla whole-body imaging based on full-wave numerical simulations*, Magnetic Resonance in Medicine: An Official Journal of the International Society for Magnetic Resonance in Medicine **57**, 235 (2007).
- [4] J. Vaughan, G. Adriany, C. Snyder, J. Tian, T. Thiel, L. Bolinger, H. Liu, L. DelaBarre, and K. Ugurbil, *Efficient high-frequency body coil for high-field MRI*, Magnetic Resonance in Medicine: An Official Journal of the International Society for Magnetic Resonance in Medicine **52**, 851 (2004).
- [5] A. Graessl, W. Renz, F. Hezel, M. A. Dieringer, L. Winter, C. Oezerdem, J. Rieger, P. Kellman, D. Santoro, T. D. Lindel, *et al.*, *Modular 32-channel transceiver coil array for cardiac MRI at 7.0 T*, Magnetic resonance in medicine **72**, 276 (2014).
- [6] G. Adriany, P.-F. Van de Moortele, F. Wiesinger, S. Moeller, J. P. Strupp, P. Andersen, C. Snyder, X. Zhang, W. Chen, K. P. Pruessmann, *et al.*, *Transmit and receive transmission line arrays for 7 Tesla parallel imaging*, Magnetic Resonance in Medicine: An Official Journal of the International Society for Magnetic Resonance in Medicine **53**, 434 (2005).
- [7] K. P. Pruessmann, M. Weiger, M. B. Scheidegger, and P. Boesiger, *SENSE: sensitivity encoding for fast MRI*, Magnetic resonance in medicine **42**, 952 (1999).
- [8] M. A. Griswold, P. M. Jakob, R. M. Heidemann, M. Nittka, V. Jellus, J. Wang, B. Kiefer, and A. Haase, *Generalized autocalibrating partially parallel acquisitions (GRAPPA)*, Magnetic Resonance in Medicine: An Official Journal of the International Society for Magnetic Resonance in Medicine **47**, 1202 (2002).
- [9] P. B. Roemer, W. A. Edelstein, C. E. Hayes, S. P. Souza, and O. M. Mueller, *The NMR phased array*, Magnetic resonance in medicine **16**, 192 (1990).
- [10] G. Shajan, M. Kozlov, J. Hoffmann, R. Turner, K. Scheffler, and R. Pohmann, *A 16-channel dual-row transmit array in combination with a 31-element receive array for human brain imaging at 9.4 T*, Magnetic resonance in medicine **71**, 870 (2014).
- [11] X. Zhang and A. Webb, *Design of a capacitively decoupled transmit/receive NMR phased array for high field microscopy at 14.1 T*, Journal of Magnetic Resonance **170**, 149 (2004).

- [12] M. Bilgen, *Inductively-overcoupled coil design for high resolution magnetic resonance imaging*, Biomedical engineering online **5**, 3 (2006).
- [13] R. F. Lee, R. O. Giaquinto, and C. J. Hardy, *Coupling and decoupling theory and its application to the MRI phased array*, Magnetic Resonance in Medicine: An Official Journal of the International Society for Magnetic Resonance in Medicine **48**, 203 (2002).
- [14] B. Wu, X. Zhang, P. Qu, and G. X. Shen, *Design of an inductively decoupled microstrip array at 9.4 T*, Journal of Magnetic Resonance **182**, 126 (2006).
- [15] N. I. Avdievich, J. W. Pan, and H. P. Hetherington, *Resonant inductive decoupling (RID) for transceiver arrays to compensate for both reactive and resistive components of the mutual impedance*, NMR in Biomedicine **26**, 1547 (2013).
- [16] X. Yan, X. Zhang, B. Feng, C. Ma, L. Wei, and R. Xue, *7T transmit/receive arrays using ICE decoupling for human head MR imaging*, IEEE transactions on medical imaging **33**, 1781 (2014).
- [17] I. R. Connell, K. M. Gilbert, M. A. Abou-Khousa, and R. S. Menon, *Design of a parallel transmit head coil at 7T with magnetic wall distributed filters*, IEEE transactions on medical imaging **34**, 836 (2014).
- [18] B. Keil, J. N. Blau, S. Biber, P. Hoecht, V. Tountcheva, K. Setsompop, C. Triantafyllou, and L. L. Wald, *A 64-channel 3T array coil for accelerated brain MRI*, Magnetic resonance in medicine **70**, 248 (2013).
- [19] J. A. de Zwart, P. J. Ledden, P. Kellman, P. van Gelderen, and J. H. Duyn, *Design of a SENSE-optimized high-sensitivity MRI receive coil for brain imaging*, Magnetic Resonance in Medicine: An Official Journal of the International Society for Magnetic Resonance in Medicine **47**, 1218 (2002).
- [20] X. Yan, J. C. Gore, and W. A. Grissom, *Self-decoupled radiofrequency coils for magnetic resonance imaging*, Nature communications **9**, 3481 (2018).
- [21] B. Zhang, D. K. Sodickson, and M. A. Cloos, *A high-impedance detector-array glove for magnetic resonance imaging of the hand*, Nature biomedical engineering **2**, 570 (2018).
- [22] D. DeMaw, *On ground low-noise receiving antennas*, QST **4**, 30 (1988).
- [23] M. D. Harpen, *The theory of shielded loop resonators*, Magnetic resonance in medicine **32**, 785 (1994).
- [24] A. Stensgaard, *Optimized design of the shielded-loop resonator*, Journal of Magnetic Resonance, Series A **122**, 120 (1996).
- [25] L. Nohava, R. Czerny, M. Obermann, M. Pichler, R. Frass-Kriegl, J. Felblinger, J.-C. Ginefri, and E. Laistler, *Flexible multi-turn multi-gap coaxial RF coils (MTMG-CCs)*:

- design concept and bench validation*, in *Proceedings 27. Annual Meeting International Society for Magnetic Resonance in Medicine*, Vol. 27 (Montréal, Canada, 2019) p. 0565.
- [26] R. Czerny, L. Nohava, R. Frass-Kriegl, J. Felblinger, J.-C. Ginefri, and E. Laistler, *Flexible multi-turn multi-gap coaxial RF coils: enabling a large range of coil sizes*, in *Proceedings 27. Annual Meeting International Society for Magnetic Resonance in Medicine*, Vol. 27 (Montréal, Canada, 2019) p. 1550.
- [27] A. Port, L. Albisetti, M. Varga, J. Marjanovic, J. Reber, D. O. Brunner, , and K. P. Pruessmann, *Liquid metal in stretchable tubes: A wearable 4-channel knee array*, in *Proceedings 27. Annual Meeting International Society for Magnetic Resonance in Medicine*, Vol. 27 (Montréal, Canada, 2019) p. 1114.
- [28] K. Nehrke and P. Börnert, *DREAM-a novel approach for robust, ultrafast, multislice B1 mapping*, *Magnetic Resonance in Medicine* **68**, 1517 (2012).
- [29] J. D. Poorter, C. D. Wagter, Y. D. Deene, C. Thomsen, F. Staahlberg, and E. Achten, *Noninvasive MRI thermometry with the proton resonance frequency (PRF) method: in vivo results in human muscle*, *Magnetic resonance in medicine* **33**, 74 (1995).
- [30] W. M. Brink, Z. Wu, and A. G. Webb, *A simple head-sized phantom for realistic static and radiofrequency characterization at high fields*, *Magnetic resonance in medicine* **80**, 1738 (2018).
- [31] J. I Mispelter, M. Lupu, and A. Briguët, *NMR probeheads for biophysical and biomedical experiments: theoretical principles & practical guidelines* (Imperial College Press, 2006).
- [32] N. Avdievich, A. Pfrommer, I. Giapitzakis, and A. Henning, *Analytical modeling provides new insight into complex mutual coupling between surface loops at ultrahigh fields*, *NMR in Biomedicine* **30**, e3759 (2017).
- [33] T. Ruytenberg, B. M. Verbist, V.-V. Oosten, E. Astreinidou, E. V. Sjögren, A. G. Webb, *et al.*, *Improvements in high resolution laryngeal magnetic resonance imaging for preoperative transoral laser microsurgery and radiotherapy considerations in early lesions*, *Frontiers in oncology* **8**, 216 (2018).

4

DESIGN OF A DIELECTRIC RESONATOR RECEIVE ARRAY AT 7 TESLA USING DETUNABLE CERAMIC RESONATORS

T. RUYTENBERG AND A.G. WEBB

Ceramic-based dielectric resonators can be used for high frequency magnetic resonance imaging and microscopy. When used as elements in a transmit array, the intrinsically low inter-element coupling allows flexibility in designing different geometric arrangements for different regions-of-interest. However, without being able to detune such resonators, they cannot be used as elements in a receive-only array. Here, we propose and implement a method, based on mode-disruption, for detuning ceramic-based dielectric resonators to enable them to be used as receive-only elements.

4.1. INTRODUCTION

Receive coil arrays are used on almost all clinical and research MR scanners. Each individual element of the array typically has a circular/rectangular/hexagonal or pentagonal geometry and is constructed from copper with an appropriate number of segmenting capacitors to reduce phase accumulation along the length of the coil. The original concepts of coil overlapping to reduce mutual inductance, and additional inter-element decoupling via an impedance mismatch at the input to the preamplifier, are still widely used [2, 3]. Different methods of decoupling individual elements have been introduced over time, including capacitive decoupling [4], inductive decoupling [5], induced current elimination [6, 7], and resonant inductive decoupling [8], the last of which can eliminate both the reactive and resistive components of inter-element coupling. Clinical receive coil arrays of 32 elements are now standard, with 64 elements currently being introduced for both neurological as well as body applications. Research arrays have shown improved performance in terms of peripheral signal-to-noise and reduced geometry factor (g-factor) in 128-element designs for cardiology and body applications [9, 10].

Although highly successful, the requirement for fixed geometries between coils to achieve effective decoupling does reduce the flexibility to place coils exactly where desired. To enable such flexibility, one would need elements which show a greater intrinsic degree of decoupling than conventional conductor-based loop coils. One possibility is to use ceramic-based high permittivity dielectric resonators, which have been shown to have low inter-element coupling [11, 12] when used as elements in a transmit/receive array. Comparisons with equivalently-sized loop arrays showed slightly better performance (in terms of the transmit efficiency per square root of maximum specific absorption rate) close to the ceramic, and slightly lower performance at larger depths [13]. These arrays showed low inter-element coupling even when elements were spaced only millimetres apart without the use of decoupling circuits.

A natural extension to existing work on high permittivity dielectric resonators would be to use them as receive-only elements, again taking advantage of the intrinsically low inter-element coupling to be able to place them where desired on the body. In conventional coils, active and passive PIN diodes are used to provide isolation between the transmit coil and each of the receive elements [12]. These can be used both in the resonant coil as well as the impedance matching network, and can be used in combination with appropriate inductors to switch in-and-out parallel LC circuits which present a very high impedance to current flow when the diodes are actively or passively turned on [14]. However, since the basic element of a dielectric resonator is a continuous ceramic block rather than a discrete-element LC circuit, this method cannot directly be applied since there are no discrete capacitive elements which can form part of a switched high impedance circuit. Methods for detuning dielectric resonators exist in the microwave literature [15], but do not provide sufficient isolation for MR operation. A method involving immersion of decoupling elements for a fluid-based dielectric resonator has been described [16], but this is not applicable to thin solid ceramic-based elements.

In solid dielectrics, electromagnetic fields can however be perturbed by adding conductors to the boundaries of the solid dielectric resonator [17–19]. Adding such a conductor perturbs the electromagnetic boundary conditions, which alters the electromagnetic mode structure. This will therefore result in a frequency shift, which can be used to tune or detune a solid dielectric resonator. In the present study, a method for effective detuning of ceramic based dielectric resonators is presented based on disrupting the fundamental mode structure via conducting strips and PIN diodes. Electromagnetic simulations and phantom verification of the efficacy of mode disruption are presented. In vivo images of the ankle were then acquired using a quadrature volume coil transmit and four-element dielectric resonator array receive at 7T.

4.2. METHODS

Electromagnetic simulations were performed using the eigenmode solver of CST Microwave Studio (v.2016.07, Darmstadt, Germany). The resonators were modelled using a conductivity of 1.5 S/m, which was determined by S_{11} network analyser measurements.

Individual dielectric resonator elements were constructed from rectangular ($88 \times 44 \times 5 \text{ mm}^3$) ceramic blocks of lead zirconate titanate (PZT), with a relative permittivity of 1070 (TRS Technologies, State College, PA, USA). These blocks can be cut to size using conventional machining tools, noting that some method of lead abatement is necessary.

All MRI experiments were performed using a human 7 Tesla MRI system (Philips Achieva). A detunable quadrature high pass birdcage head coil with internal diameter 28 cm was used for transmission (Nova Medical, Wilmington, MA). An array of four identical dielectric resonator antennas with detuning circuits was constructed. Phantom experiments were performed using a 90 mm diameter cylindrical oil phantom and a low tip-angle 3D gradient echo sequence. In vivo experiments were performed on healthy volunteers under the auspices of the local medical ethics committee. Images of the ankle were acquired using a 3D gradient echo sequence (T1-weighted, field-of-view $120 \times 120 \times 60 \text{ mm}^3$, data matrix $160 \times 160 \times 80$ to give 0.75 mm isotropic spatial resolution, echo time 2.8 ms, repetition time 10 ms, tip angle 10° , total acquisition time 168 s). Parallel imaging experiments were performed using a reduction factor of 1.5 in each of two directions, resulting in an imaging time of 75 s.

4.3. RESULTS

The resonance frequencies of the different modes of a rectangular dielectric resonator are determined by its dimensions, and can be calculated to a high degree of accuracy by solving the basic transcendental equations using various numerical methods [20]. The resonant frequencies are also affected by the boundary conditions of the resonator [21]. A change in resonant frequency can be produced by displacement of the electric and

magnetic fields, and its direction of change can be determined from cavity perturbation theory. Specifically, if the stored energy is mostly electric, moving a metal shielding wall closer to the resonator lowers the resonant frequency. Conversely, for a displaced field that is predominantly magnetic, the resonant frequency increases.

As in previous work [13], the receive array is based on dielectric resonators operating in the $TE_{01\delta}$ mode, with inductive impedance matching provided via a coupling loop placed above the center of the resonator. Therefore, it is easiest to introduce a detuning mechanism on the sides of the resonator, well away from the coupling loop. Placing a conductive element close to the side of the rectangular resonator interacts primarily with the electric field and therefore lowers the resonance frequency. The long side of the resonator is chosen, since in this area the electric field is highest and therefore a given perturbation results in a larger frequency shift. In order to perturb the electric field, a number of gapped copper strips are added to the resonator. Individual segments are inter-connected using PIN diodes. Passing a DC current through the diodes effectively changes the attached copper strips from small discrete elements to one much longer element.

Fig. 4.1 shows the results of eigenmode electromagnetic simulations from the ceramic resonator, one with four small segmented copper strips on each side, and one with a long single copper strip of equivalent length. Fig. 4.1(b)(e) shows the magnetic and electric field distributions in both vector and magnitude depictions, corresponding to the $TE_{01\delta}$ mode.

Fig. 4.1(g) and (h) shows the effects of the segmented copper strip. The mode structure is very similar in terms of the magnetic field distribution (slightly foreshortened and broadened), but quite different in terms of the electric field distribution. The resonant frequency of the $TE_{01\delta}$ mode is shifted lower by 20 MHz. Fig. 4.1(j) and (k) shows the fields produced for the long copper strip. This lowest frequency mode has a very weak magnetic field component, and is shifted in frequency to 180 MHz: there is a higher order mode which occurs close to 298 MHz but has a very weak B-field component which is parallel to B_0 and therefore gives no signal.

Fig. 4.2(a) shows the constructed resonator with detuning circuit fabricated by creating printed circuit boards with four 10 CE 10 mm² copper strips: these were fixed to the sides of the resonator using conductive silver paint (Pelco 16062). The strips are inter-connected with PIN diodes (MA4P7441F-1091, Macom, Lowell, MA, USA): each side of the resonator is driven by a 100 mA DC current from the Philips MR system. Fig. 4.2(b) shows the network analyser plot of the S_{11} reflection coefficient from an untuned pickup loop placed above the center of the resonator to demonstrate the frequency detuning. The resonant $TE_{01\delta}$ mode at 298 MHz (blue) shifts by more than 100 MHz to approximately 180 MHz (red) when the diodes are turned on, in good agreement with the electromagnetic simulations. Fig. 4.2(c) shows a fully assembled dielectric resonator antenna with an impedance-matching loop with variable capacitors to accommodate different loads. The impedance matching network contains a detuning PIN diode and RF

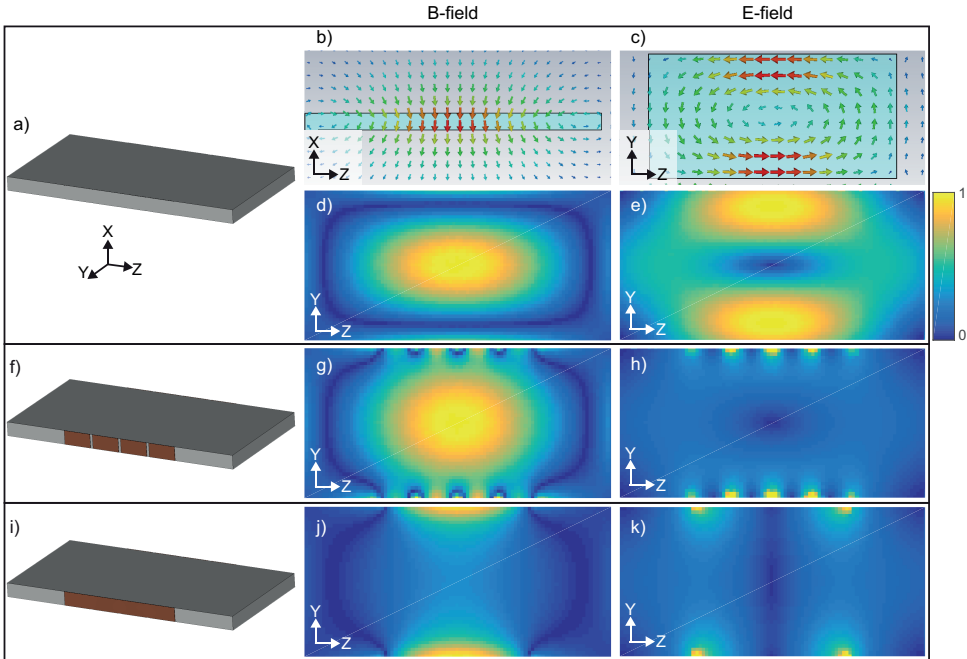


Figure 4.1: Results from eigenmode simulations. (a), (f) and (i) Show schematics of the ceramic block resonator, the resonator with un-connected copper strips, and the resonator with one continuous long strip. (d), (g) and (j) Show the magnitude of the magnetic field looking from the top of the resonator. (e), (h) and (k) Show the corresponding magnitude of the electric field. (b) Shows the vector field corresponding to (d) as seen from the side of the resonator, and (c) shows the vector field corresponding to (e) as a top view.

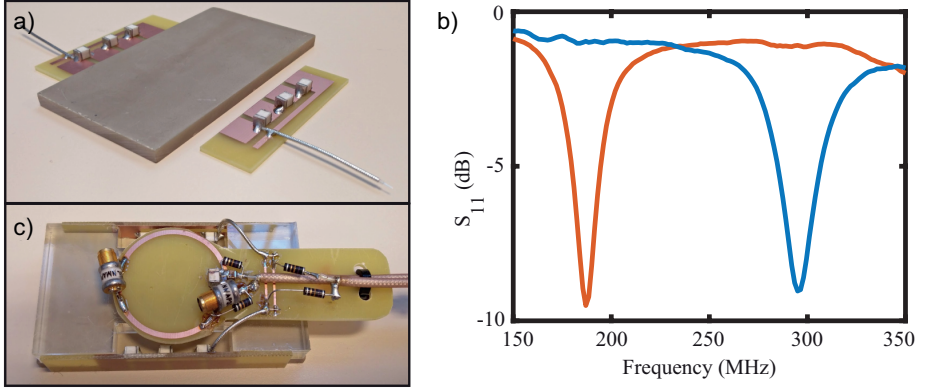


Figure 4.2: Dielectric resonator with detuning circuits which are electrically connected to the ceramic with silver paint. (b) Network analyser plots using a non-resonant pick-up loop on a dielectric resonator without (blue) and with (red) detuning current applied. (c) The fully assembled dielectric resonator.

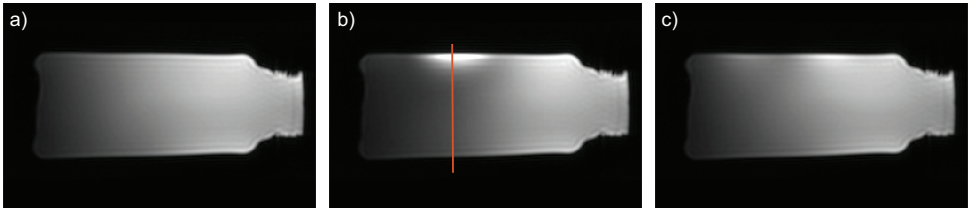


Figure 4.3: 3D low tip angle gradient echo images of a cylindrical oil phantom acquired with: (a) volume coil transmit and receive with no dielectric resonator, (b) a dielectric resonator placed on top of the phantom but no detuning current applied, (c) identical to (b) with the detuning current applied. The vertical line in (b) shows the center of the dielectric resonator.

chokes.

Fig. 4.3 shows phantom scans using the quadrature volume coil as a transmitter. Fig. 4.3(a) shows the image using the volume coil in transmit/receive mode with no dielectric resonator present. Fig. 4.3(b) shows images acquired with dielectric resonator placed on top of the phantom without a detuning current being applied. As expected, image artefacts are seen due to the presence of the resonator concentrating the transmit field due to strong coupling with the volume coil. Fig. 4.3(c) shows the same situation as in (b) except that now a detuning current is applied to the PIN diodes. The image is almost identical to that when there is no dielectric resonator present, showing that the detuning mechanism is effective.

Fig. 4.4 shows images using a volume coil in transmit mode and a four-element dielectric resonator array placed equidistantly around the oil phantom as receive elements. The

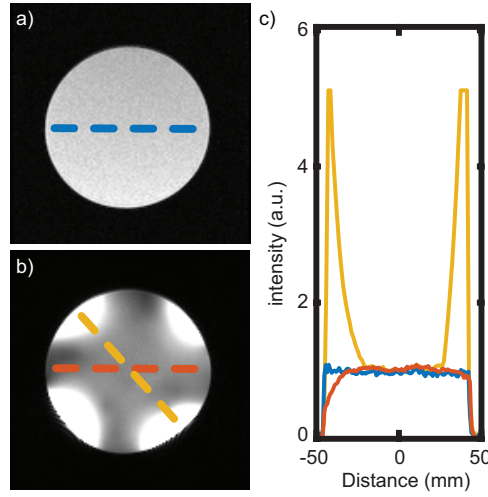


Figure 4.4: Oil phantom images acquired using a low tip angle 3D gradient echo sequence with: (a) volume coil in transmit and receive, (b) volume coil in transmit and four-element dielectric resonator array in receive. (c) Line profiles for the cross sections shown in (a) and (b).

increase in signal-to-noise close to the elements is approximately a factor-of-five.

Fig. 4.5 shows in vivo images of the ankle of a healthy volunteer, acquired with an isotropic spatial resolution of 0.75 mm. The volume coil was used in transmit mode, with four dielectric resonator elements placed around the ankle. Accelerated imaging using a SENSE factor [22] of 1.5 in both the left-right and anterior-posterior directions was also performed, reducing the imaging time from 168 s to 75 s with no visible image artefacts, as shown in Fig. 4.5(d)(f).

4.4. CONCLUSIONS

In this work we have proposed and tested a method for electronic detuning of ceramic dielectric resonators using PIN diodes and conductive elements which produce significant shifts in the frequency of the $TE_{01\delta}$ resonant mode. In vivo images of the extremities were acquired with a four-element detunable receive-only dielectric resonator array, with the number of elements being possible to scale up relatively easily for imaging larger fields-of-view.

Previous work has shown that dielectric resonators possess similar properties to surface coils of equivalent size in terms of transmit and receive efficiency [11, 13]. There are obviously both advantages and disadvantages of designing a dielectric resonator array compared to a conventional surface coil array, as have been discussed in several previous papers. Given the similarities in terms of transmit efficiency, the major advantage is

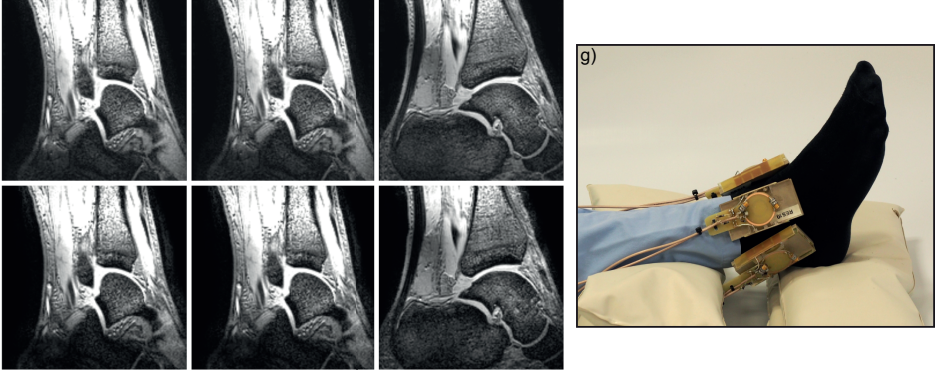


Figure 4.5: Three slices from a 3D T1-weighted gradient echo sequence of a human ankle, data matrix $160 \times 160 \times 80$, 0.75 mm isotropic spatial resolution, TE 2.8 ms, TR 10 ms, FA 10 degrees. (a)(c) without acceleration. (d)(f) a reduction factor of 1.5 in two directions. A four element detunable dielectric resonator array was used for signal reception as depicted in figure (g).

the lower inter-element coupling, and the major disadvantage is that the size of the resonator cannot be freely chosen given the limited availability of materials with specific relative permittivity values.

Inter-element coupling between dielectric resonators depends upon the permittivity of the material used: very high permittivities reduce the interaction with neighbouring elements, but this is accompanied by a lower penetration of the magnetic field component of the $TE_{01\delta}$ mode of the resonator. There is, therefore, a tradeoff between the two properties which remains to be studied systematically.

4.5. ACKNOWLEDGMENTS

This work was supported by The Netherlands Organization for Scientific Research, Domain Applied and Engineering Sciences (NWO Domain TTW), project number 13783.

REFERENCES

- [1] T. Ruytenberg and A. G. Webb, *Design of a dielectric resonator receive array at 7 Tesla using detunable ceramic resonators*, Journal of Magnetic Resonance **284**, 94 (2017).
- [2] P. B. Roemer, W. A. Edelstein, C. E. Hayes, S. P. Souza, and O. M. Mueller, *The NMR phased array*, Magnetic resonance in medicine **16**, 192 (1990).
- [3] S. M. Wright, R. L. Magin, and J. R. Kelton, *Arrays of mutually coupled receiver coils: theory and application*, Magnetic resonance in medicine **17**, 252 (1991).
- [4] B. Wu, X. Zhang, P. Qu, and G. X. Shen, *Capacitively decoupled tunable loop microstrip (TLM) array at 7 T*, Magnetic resonance imaging **25**, 418 (2007).
- [5] B. Wu, C. Wang, R. Krug, D. A. Kelley, D. Xu, Y. Pang, S. Banerjee, D. B. Vigneron, S. J. Nelson, S. Majumdar, *et al.*, *7T human spine imaging arrays with adjustable inductive decoupling*, IEEE Transactions on Biomedical Engineering **57**, 397 (2010).
- [6] Y. Li, Z. Xie, Y. Pang, D. Vigneron, and X. Zhang, *ICE decoupling technique for RF coil array designs*, Medical physics **38**, 4086 (2011).
- [7] X. Yan, J. C. Gore, and W. A. Grissom, *New resonator geometries for ICE decoupling of loop arrays*, Journal of Magnetic Resonance **277**, 59 (2017).
- [8] N. I. Avdievich, J. W. Pan, and H. P. Hetherington, *Resonant inductive decoupling (rid) for transceiver arrays to compensate for both reactive and resistive components of the mutual impedance*, NMR in Biomedicine **26**, 1547 (2013).
- [9] M. Schmitt, A. Potthast, D. E. Sosnovik, J. R. Polimeni, G. C. Wiggins, C. Triantafyllou, and L. L. Wald, *A 128-channel receive-only cardiac coil for highly accelerated cardiac MRI at 3 Tesla*, Magnetic Resonance in Medicine: An Official Journal of the International Society for Magnetic Resonance in Medicine **59**, 1431 (2008).
- [10] C. J. Hardy, R. O. Giaquinto, J. E. Piel, K. W. Rohling AAS, L. Marinelli, D. J. Blezek, E. W. Fiveland, R. D. Darrow, and T. K. Foo, *128-channel body MRI with a flexible high-density receiver-coil array*, Journal of Magnetic Resonance Imaging: An Official Journal of the International Society for Magnetic Resonance in Medicine **28**, 1219 (2008).
- [11] S. Aussenhofer and A. Webb, *An eight-channel transmit/receive array of TE01 mode high permittivity ceramic resonators for human imaging at 7 T*, Journal of Magnetic Resonance **243**, 122 (2014).
- [12] W. Edelstein, C. Hardy, and D. Mueller, *Electronic decoupling of surface coils for NMR imaging and spectroscopy*, in *annual meeting of the Society of Magnetic Resonance in Medicine, London*, Vol. 2 (1984) pp. 1084–1085.
- [13] T. P. O'reilly, T. Ruytenberg, and A. G. Webb, *Modular transmit/receive arrays using very-high permittivity dielectric resonator antennas*, Magnetic resonance in medicine **79**, 1781 (2018).

- [14] E. A. Barberi, J. S. Gati, B. K. Rutt, and R. S. Menon, *A transmit-only/receive-only (TORO) RF system for high-field MRI/MRS applications*, Magnetic Resonance in Medicine: An Official Journal of the International Society for Magnetic Resonance in Medicine **43**, 284 (2000).
- [15] D. Kajfez and P. Guillon, *Dielectric Resonators*, 2nd ed. (Noble Publishing Corporation, 1998).
- [16] S. A. Aussenhofer and A. G. Webb, *Design and evaluation of a detunable water-based quadrature HEM11 mode dielectric resonator as a new type of volume coil for high field MRI*, Magnetic resonance in medicine **68**, 1325 (2012).
- [17] B. Virdee, *Current techniques for tuning dielectric resonators*, Microwave Journal **41**, 130 (1998).
- [18] R. F. Harrington, *Time-harmonic electromagnetic fields* (McGraw-Hill, 1961).
- [19] A. Netic, *A new method for frequency modulation of dielectric resonator oscillators*, (Proceeding of the 15th European Microwave Conference, 1985).
- [20] R. K. Mongia and A. Ittipiboon, *Theoretical and experimental investigations on rectangular dielectric resonator antennas*, IEEE Transactions on Antennas and Propagation **45**, 1348 (1997).
- [21] S. Fiedziuszko and A. Jelenski, *The influence of conducting walls on resonant frequencies of the dielectric microwave resonator (correspondence)*, IEEE Transactions on Microwave Theory and Techniques **19**, 778 (1971).
- [22] K. P. Pruessmann, M. Weiger, M. B. Scheidegger, and P. Boesiger, *SENSE: sensitivity encoding for fast MRI*, Magnetic resonance in medicine **42**, 952 (1999).

5

INTEGRATED DIELECTRICS FOR SNR IMPROVEMENTS IN RECEIVE-ONLY SURFACE COILS AT 3T

T. RUYTENBERG, T.P. O'REILLY AND A.G. WEBB

A receive-only surface coil array for 3 Tesla integrating a high-permittivity material (HPM) with a relative permittivity of 660 was designed and constructed and subsequently its performance was evaluated and compared in terms of transmit field efficiency and specific absorption ratio (SAR) during transmission, and signal-to-noise ratio during reception, with a conventional identically-sized surface coil array. Finite-difference time-domain simulations, bench measurements and in-vivo neck imaging on three healthy volunteers were performed using a three-element surface coil array with integrated HPMs placed around the larynx. Simulation results show an increase in local transmit efficiency of the body coil of ~10-15% arising from the presence of the HPM. The receiver efficiency also increased by approximately 15% close to the surface. Phantom experiments confirmed these results. In-vivo scans using identical transmit power resulted in SNR gains throughout the laryngeal area when compared with the conventional surface coil array. In particular specifically around the carotid arteries an average SNR gain of 52% was measured averaged over the three subjects, while in the spine an average of 20% SNR gain was obtained.

5.1. INTRODUCTION

High-permittivity materials (HPMs) have been used in many studies as a method to tailor transmit (B_1^+) and/or receive (B_1^-) field efficiencies and spatial distributions. For very high field (7T) a variety of dielectric materials, ranging from plain water [2] to calcium and barium titanate powders mixed with (deuterated) water [3, 4] and solid ceramics [5] with relative permittivities ranging from 78 to 300 have been used either to homogenize the B_1^+ field or to produce local focusing of the B_1^+ field for improved imaging of specific anatomies, such as the temporomandibular joint and the inner ear [6, 7]. The receive sensitivity is also affected by these HPMs, which can manifest as an increased SNR [8, 9].

HPMs have also been used at clinical field strengths as 1.5 and 3T, with results showing increased SNR [10] and locally increased B_1^+ fields and reduced SAR [10, 11]. By considering Ampère's law with Maxwell's addition:

$$\nabla \times \mathbf{B} = \mu_0 (\mathbf{J}_c + \mathbf{J}_d) = \mu_0 (\mathbf{J}_c + j\omega\epsilon\mathbf{E}) \quad (5.1)$$

where \mathbf{J}_c is the conduction current and \mathbf{J}_d the displacement current equal to $j\omega\epsilon\mathbf{E}$ with j the imaginary unit, ω the angular frequency and the permittivity, higher permittivities are required at these lower fields [12]. Relative permittivity values of 1000 have been used for imaging the spine at 3T [13], values of 1200 and 3300 at 1.5 and 3T for head imaging [14], and 4500 at 1.5T for wrist imaging [15]. In the last two studies, SNR gains of about 50% were demonstrated in-vivo. Vaidya et al. [16] have shown in a simulation study on ideal current patterns that although ultimate intrinsic SNR [17] is not improved using HPMs, these materials can shift the balance between optimal and dark modes [18], leading to the demonstrated SNR gains for specific coil arrays.

In all of these previous studies, HPMs have been placed inside commercial coil arrays, which can potentially lead to detuning and alterations in the coupling matrices between the various elements of the array. Additionally, in experimental studies these materials never fully cover the entire coil array, or they are used in combination with volume coils, where the coil is far away for the imaged object and therefore from the HPM.

In this study, therefore, we specifically design surface coil arrays with the HPMs integrated into the structure, covering the entirety of the coil array. Electromagnetic simulations, phantom experiments and in-vivo imaging were performed to evaluate the effect on transmit and receive field efficiencies of a receive-only coil with integrated HPM compared to an identically sized conventional coil without HPM.

5.2. METHODS

5.2.1. COIL MANUFACTURING AND CHARACTERIZATION

For coil characterization and comparison purposes, a conventional receive-only surface coil with inner dimensions of $73 \times 60 \text{ mm}^2$, conductor width of 3 mm etched on an FR4 PC board, with four tuning capacitors of 27 pF and a balanced capacitive matching network was constructed, with a second one of identical dimensions incorporating a rectangular dielectric block (lead zirconate titanate, PZT, $70 \times 57 \times 10 \text{ mm}^3$, $\epsilon_r = 660$, $\sigma = 0.01 \text{ S/m}$, mass = 210 gr, TRS Technologies, State College, PA, USA) placed in the center of the surface coil (Figure 5.1a). The dielectric block had no resonances at the imaging frequency (lowest mode $f_{TE01\delta} = 267 \text{ MHz}$). For a rectangular waveguide with perfectly reflecting boundaries, resonant frequencies can be determined using the following equation

$$f_{mnp} = \frac{1}{2\sqrt{\mu_r \epsilon_r}} \sqrt{\frac{m^2}{a^2} + \frac{n^2}{b^2} + \frac{p^2}{d^2}} = \frac{c}{2} \sqrt{\frac{m^2}{a^2} + \frac{n^2}{b^2} + \frac{p^2}{d^2}} \quad (5.2)$$

with m, n and p the mode numbers, and a, b , and d the length, width and thickness of the dielectric; μ_r and ϵ_r are the relative permeability and permittivity, respectively. For very high permittivity materials this would be a good approximation, but to estimate both permittivity and conductivity of the material, electromagnetic finite-difference time-domain simulations were performed. In these simulations a dielectric block was simulated with a weakly-coupled pick-up coil on top. Electric permittivity and conductivity were iteratively changed until agreement with bench measurements was found on both the Q-value and eigenfrequencies. Both coils were tuned and matched to 50 Ohms at 127.8 MHz when placed on a tissue-mimicking phantom ($\epsilon_r = 45$ and $\sigma = 0.4 \text{ S/m}$). Both coils used could be tuned using a 0-10 pF variable capacitor. For matching, the conventional loop used two 28 pF capacitors and the integrated HPM coil two 20 pF capacitors. For detuning during transmission, passive circuits were implemented using crossed diodes (UMX9989AP, Microsemi, Lowell, MA, USA) and an active circuit was implemented using an LC-trap with PIN-diode (MA4P7441F-1091T, MACOM, Lowell, MA, USA) [19].

For in-vivo imaging, three-element receive-only coil arrays were constructed, one array with HPM and a conventional array without. The design was chosen such that the two outer elements are positioned above the carotid arteries and the middle element above the larynx. Individual elements in the arrays were fitted on a 3D-printed curved holder with a radius of 60 mm and were subsequently decoupled using induced current elimination (ICE) circuits [20]. These circuits consist out of three overlapping loops, two of the neighboring elements, and one of the additional resonator in between these loops. The decoupling was tuned using the middle loop with a 10-20 pF variable capacitor. Tuning and matching of the array was performed while loaded with a phantom ($\epsilon_r = 79$,

$\sigma = 0.5 \text{ S/m}$) such that S_{11} -parameters were better than -18 dB and the ICE decoupling between neighboring elements was lower than -22 dB. Coupling between the two non-neighboring elements was -12 dB for both arrays. Floating common-mode chokes of a bazooka type [21] were placed on every channel of the coils with a measured common mode suppression ratio of 20 dB. For MR measurements, a receive interface box was used with low-impedance ($\sim 2 \text{ Ohm}$) pre-amplifiers.

5.2.2. ELECTROMAGNETIC SIMULATIONS

All simulations were performed using CST Microwave Studio 2019 (CST MWS, Darmstadt, Germany). In order to investigate the receive performances of single coil elements, finite difference time-domain (FDTD) simulations were performed using four discrete ports. Capacitors were simulated at these ports as well as a single port on the short side of the coil containing a capacitive matching circuit combined with a driving port. The coil was placed 15 mm away from a rectangular phantom measuring $300 \times 300 \times 200 \text{ mm}^3$ with a relative permittivity of 60 and a conductivity of 0.4 S/m . B_1^- fields were subsequently obtained using 1 Watt accepted power. The effects of the HPM on the B_1^+ fields were investigated by simulating the three-element in-vivo array on a cylindrical phantom using the birdcage body coil. Finally the in-vivo array was simulated on a body voxel model (Gustav, CST Voxel Family) to estimate changes in the local SAR and the location and value of the maximum SAR_{10g} .

5.2.3. IMAGING SEQUENCES

The 3T quadrature body coil was used for transmission in all experiments and the integrated posterior receive coil in the patient bed was disabled. SNR scans on a phantom were performed using proton-density weighted gradient echo sequences with acquisition voxel size = $1 \times 1 \times 5 \text{ mm}^3$, acquisition matrix = 400×400 , TE/TR = $2.2/2000 \text{ ms}$, flip angle = 20° , duration 606 s. Post processing was performed using raw data to obtain absolute SNR units [22]. Transmit efficiency (B_1^+) maps were acquired on a phantom using the Dual Refocusing Echo Acquisition Mode (DREAM) method [23] with a TR extension of 30 ms and a stimulated echo acquisition mode angle of 60 degrees.

For all in-vivo scans on healthy volunteers IRB approval for this study was obtained and written informed consent was acquired from every volunteer prior to their participation. In-vivo, carotid artery imaging was performed using turbo spin echo (TSE) black blood sequences, triggered on the cardiac cycle. T1-weighted imaging was performed with parameters: acquisition voxel size = $0.55 \times 0.75 \times 3 \text{ mm}^3$, acquisition matrix = 272×198 , TE/TR = $9/1333 \text{ ms}$, slices = 9, duration = 288 s and T2-weighted imaging using acquisition voxel size = $0.55 \times 0.75 \times 3 \text{ mm}^3$, acquisition matrix = 272×195 , TE/TR = $80/3750 \text{ ms}$, slices = 9, duration = 210 s. For the SNR measurements, a single-slice T1-weighted black blood sequence was run with the following parameters: acquisition voxel size = $0.55 \times 0.75 \times 3 \text{ mm}^3$, acquisition matrix = 272×198 , TE/TR = $9/882 \text{ ms}$, dura-

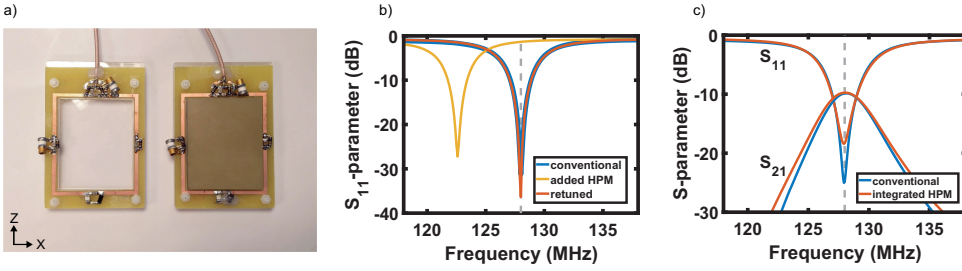


Figure 5.1: a) a photograph of a conventional rectangular surface coil on the left, and on the right a coil with added high permittivity material. b) S_{11} -parameters of the conventional and integrated HPM coil (before and after retuning). c) coupling between two conventional coils placed side by side with 45 mm separation, and the corresponding plot for two coils with integrated HPMs.

tion = 21 s. The in-vivo coils were used in combination with a radiotherapy head cushion (Black MaxSupports wideshaped, MacroMedics, Waddinxveen, The Netherlands) to reduce head motion during scanning, for subject comfort, and for slightly lifting up the chin for increased accessibility to the neck enabling easier positioning of the coil.

In the experimental comparison of elements and arrays with and without HPM, the following sequence was adhered to for comparisons when the data was acquired in series. First the coil with HPM was positioned and a full system calibration was initiated, after which scanning was performed. The coils were interchanged to the coil without HPM and scanning was performed without recalibrating the system. Not recalibrating ensures that no parameters were changed by the system unknowingly.

5.3. RESULTS

Figure 5.1a) shows a photograph of the conventional surface coil and one with an integrated HPM block. Figure 5.1b) plots the respective S_{11} parameters when the block is simply placed inside the conventional surface coil. As expected the resonance frequency decreases (by approximately 5 MHz) due to the presence of the material. Notice that the Q-value is essentially unchanged, indicating that the loss tangent of the material is low. The unloaded/loaded Q-values were measured to be 6.5 and 3.3 for elements with and without HPM, respectively. The coil with integrated HPM is simply retuned by adjusting the variable capacitor opposite the matching network. Figure 5.1c) shows the coupling behavior between two loaded coils placed close to one another: the characteristics with and without the HPM are essentially identical.

Figure 5.2a) shows a graphical representation of the simulation setup for the surface coil without HPM, and Figure 5.2b) the one with the HPM. Corresponding B_1^- maps are shown in Figure 5.2c) and d) respectively. The ratio of these two maps shows local differences close to the dielectric, as illustrated in Figure 5.2e). Up to a 15% increase in the B_1^- is observed at the surface, with the ratio reducing to unity at a depth of ~ 80 mm. The

B_1^- gains were also studied for different simulated permittivities as shown in Figure 5.2f). Higher permittivities show higher gains at the surface, although these are accompanied by some loss at increasing depths compared to no HPM: for example for the case of $\epsilon = 1500$ the ratio is less than unity for depths greater than ~ 70 mm. Figure 5.2g) finally shows the effect of using HPM of a different thickness, while keeping the distance between the bottom of the HPM and the phantom constant. Thicker HPM shows higher surface gains, but at depth B_1^- fields are slightly lower.

Figure 5.3 shows experimental results comparing the SNR of images acquired with a conventional surface coil and one with the integrated HPM placed on the same phantom. There was a 200 mm distance between the center of the elements to ensure that there was no coupling between them. SNR images are shown in Figure a) and a plot of the SNR along the central axis is shown in Figure b) for both elements. A 49% increase in SNR at the surface is measured. As these measurements were performed with a low tip angle gradient echo sequence, the measured SNR increase is proportional to the product of the B_1^+ and B_1^- fields. Electromagnetic simulations show that the B_1^+ field from the transmit coil is enhanced by $\sim 15\%$ at the surface by the HPM (see also results in Figure 5.5e). Thus the measured enhancement in the images is somewhat greater than the simulated value of $\sim 32\%$.

Figures 5.4 a) and b) show photographs of the three coil array with integrated HPMs (an identical setup without HPMs was also constructed). The measured S-parameter matrices are shown in Figures 5.4c) and d), showing very similar characteristics in terms of inter-element decoupling

Since it is well-known that HPMs alter the B_1^+ distribution, a simulation was performed using the setup shown in Figure 5.5a). The results are shown in Figure 5.5b) which indicates an increase in the B_1^+ with HPM present of approximately 15% directly below the HPM. Figure 5.5c) shows the experimental results obtained using the DREAM sequence, which show a slightly higher maximum value of 20% with good co-location of the areas of increased transmit efficiency when compared with the simulation results. Power was not adjusted in the comparison of Figure 5.5c), while for 5.5d) this optimization was performed. Figure 5.5e) finally shows the SNR ratio of the setup with and without HPM where a power optimization was performed for both setups individually as in Figure 5.5d). A 60% increase in SNR is observed close to the HPM.

Figure 5.6 shows SAR and B_1^+ simulations on a voxel body model using the transmit body coil. The neck of the body model was centered in the coil and simulations were run without and with three HPM blocks ($\epsilon_r = 660$) on the anterior side of the neck corresponding to the three-element coil array. Simulations were run with 1 Watt accepted power and SAR_{10g} was calculated. The figure shows the location of maximum SAR to be on the posterior side of the neck for both simulation without and with HPM present. A 2% increase in the maximum SAR_{10g} from 1.85 W/kg to 1.89 W/kg is observed when applying the HPM. The B_1^+ simulations show a 5-20% B_1^+ increase in the anterior side of the neck.

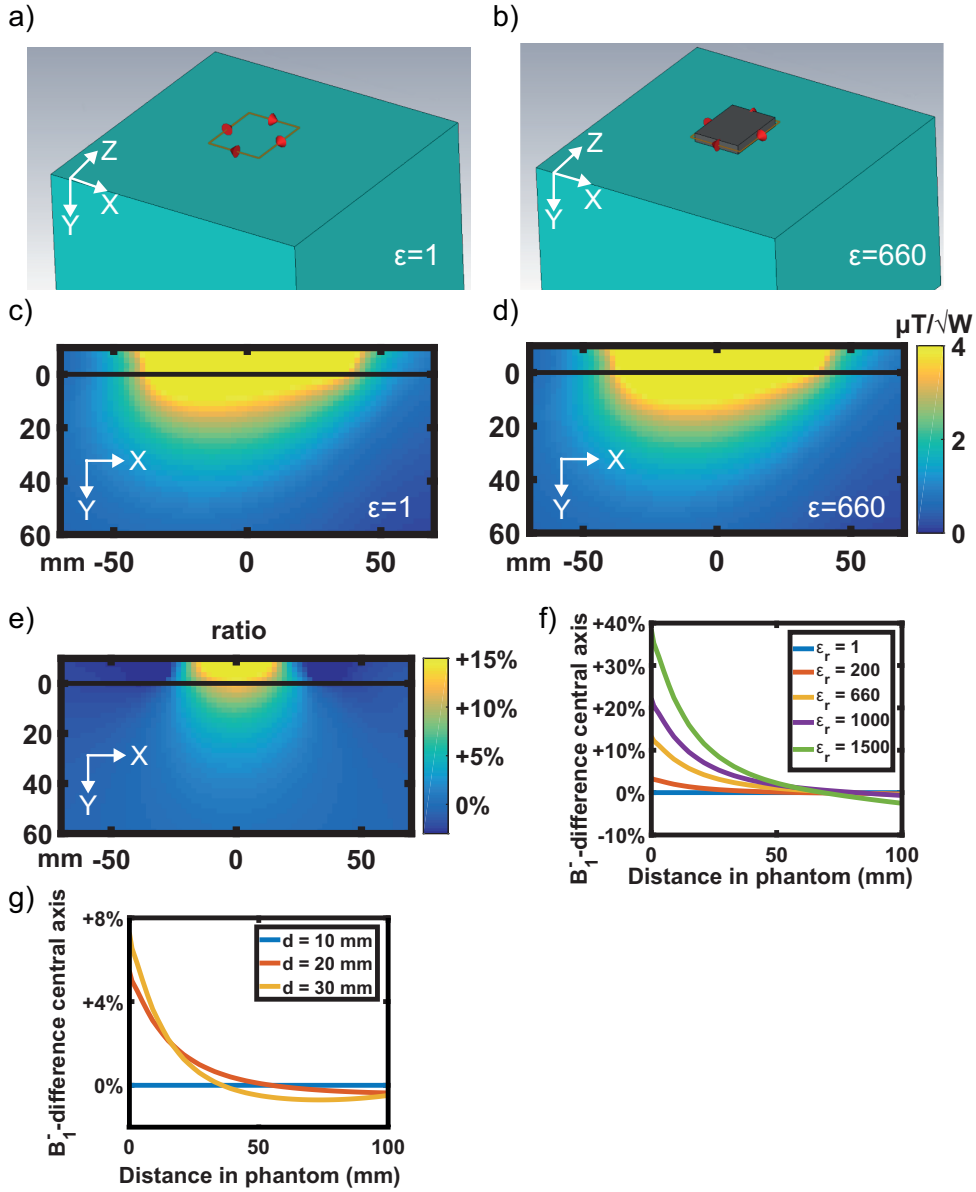
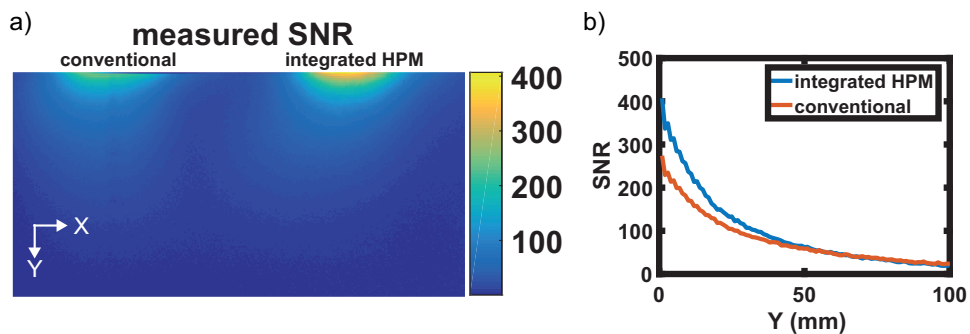


Figure 5.2: Simulated B_1^- fields in a phantom. a) and c) surface coil with no HPM, b) and d) surface coil with HPM $\epsilon_r=660$, $\sigma=0.01 \text{ S/m}$, e) Ratio of the B_1^- field with HPM relative to that without HPM, showing a maximum of 15% increase, f) Plot of the ratio along the central axis of the coil as a function of depth in the phantom for different permittivities (constant conductivity of 0.01 S/m). g) varying thickness of the HPM ($\epsilon_r=660$, $\sigma=0.01 \text{ S/m}$), while the distance from the bottom of the HPM to the phantom is kept constant. All B_1^- simulations were performed using 1 W accepted power.



5

Figure 5.3: SNR comparison of a single-element conventional and integrated HPM coil placed on a tissue-mimicking phantom. Setup and axes as in Figure 5.1a. a) Proton-density weighted gradient echo image. b) SNR plot along the central axis of each coil. Some Gibbs ringing is noticeable in the profiles.

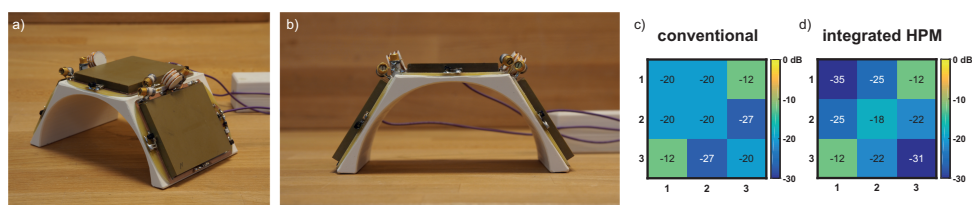


Figure 5.4: The three-channel array used for in-vivo measurements with integrated HPM. An identical array was constructed without HPM for comparison (not shown). a) overview, b) front view. c) and d) show measured S-parameter matrices on a cylindrical phantom.

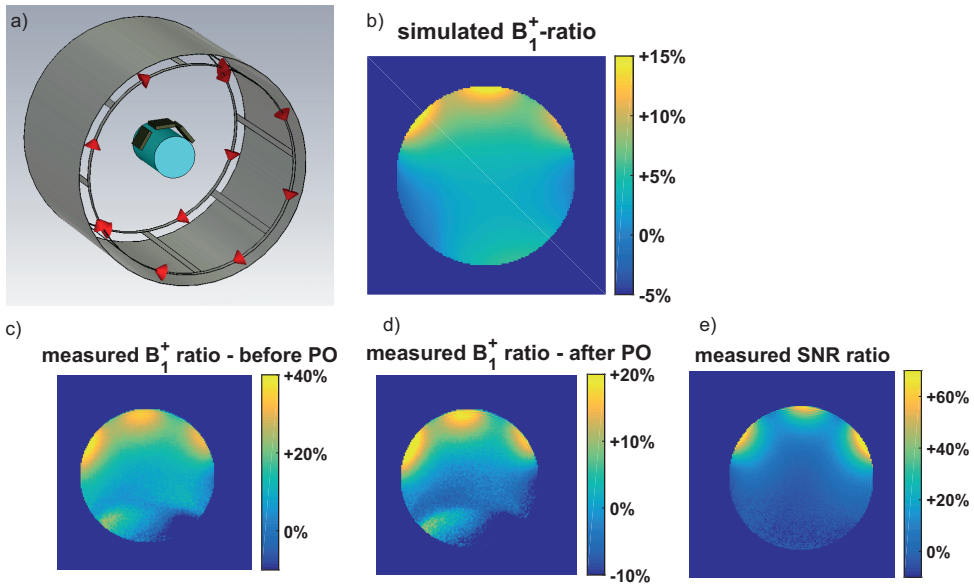


Figure 5.5: Simulations and comparative measurements of the B_1^+ fields using the in vivo array. a) simulation setup, showing the transmit birdcage. b) the ratio map of two B_1^+ field simulations on a phantom, one with HPM and one without. c) measured B_1^+ ratio of HPM/noHPM without power optimization (PO). d) measured B_1^+ ratio of HPM/noHPM with PO. 41% less power was used, resulting in about 20% less B_1^+ . e) measured SNR ratio of HPM/noHPM (after PO). A 60% increase in SNR is measured in the vicinity of the HPM.

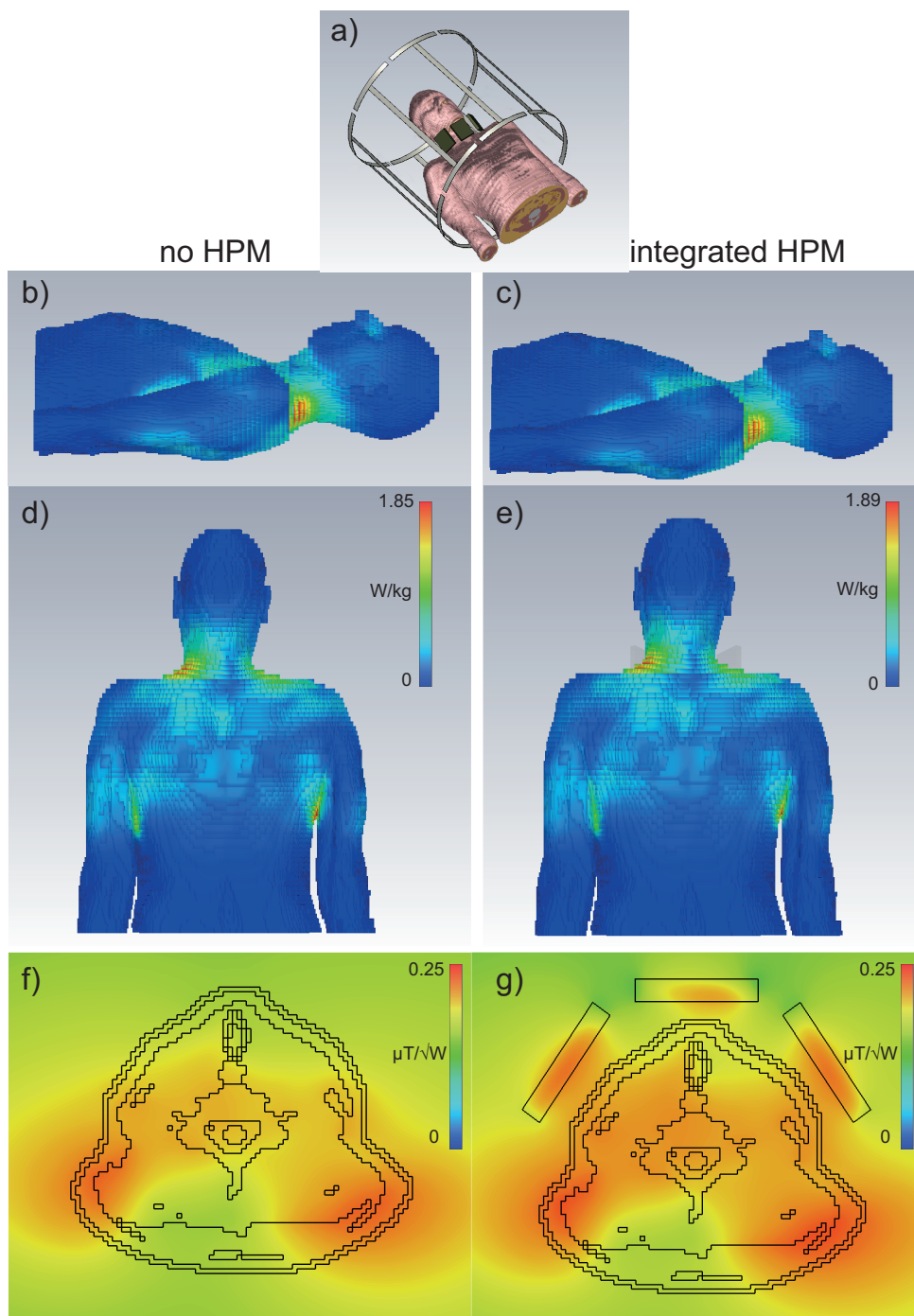


Figure 5.6: SAR_{10g} simulations using the body coil on a voxel model a) simulation setup (birdcage shield not shown for visibility). b) and c) side view for no HPM and integrated HPM, showing the location of the maximum SAR on the posterior side of the neck. d) and e) posterior view. An increase of 2% maximum SAR_{10g} is observed when using the integrated HPM coil with equal accepted power. f) and g) Simulated B_1^+ fields in a transversal slice in the neck.

Figure 5.7 shows results from in-vivo scanning of three volunteers using both conventional and integrated HPM coil arrays. The coil covers the anterior part of the neck, and so can be used for either laryngeal imaging [23][24] or also carotid artery imaging. The SNR was compared at four points: 1. the anterior side of the carotid artery, 2. the posterior side of the carotid artery, 3. the posterior side of the larynx, and additionally a deeper anatomy at point 4, the spinal cord. The same transmit power was applied for both sets of scans. An increase in SNR is observed in all regions for all volunteers when the coil with integrated HPM is used and around the carotid artery specifically, an increase of 52% is measured. The posterior side of the larynx shows an average increase of 45% and for the spinal cord an average increase of 20% is observed. The depth of the center of the spinal cord (point 4 in Figure 5.7a) from the skin surface at the position of the outer coil elements was measured to be 61, 52, and 55 mm for the three subjects. That SNR gains are achieved at these depths can possibly be explained by both the semi-annular geometry causing all elements to contribute to the signal at this point, and by the air cavity of the throat, possibly leading to a slightly higher penetration depth than simulated on the uniform phantoms.

5.4. CONCLUSION AND DISCUSSION

The results presented here show that by specifically designing receive-only surface coil arrays with integrated HPMs both the local transmit and receive efficiencies can be increased by 15 to 20% close to the surface with only a very small (~2%) increase in SAR. SNR gains of up to 52% averaged over three subjects were measured in vivo.

For the in-vivo scans the choice was made to compare coils with and without integrated HPM using the same transmit power to study the SNR differences. In general, literature shows that using HPM introduces B_1^+ gains which can be compensated by using less transmit power [10, 13, 25]. Not using equal power in this study would therefore likely lead to lower transmit power for the coil with integrated HPM and subsequently a lower SAR. The influence of recalibrating the utilized power was assessed during phantom scans in Figure 5.5, showing that 41% less power for the HPM coil can be used compared to the conventional coil when requesting a 90° flip angle in the isocenter transversal plane. We anticipate that this difference in power can also be achieved during the in vivo scans and that due to not applying this optimization when switching to the conventional coil, the achieved flip angles for the no HPM case in Figure 5.7 might have been slightly lower than requested.

While central axis gains are evident from Figure 5.2, a lower field-of-view is also observed in the figure, as the ratio in Figure 5.2e is slightly below unity at about 50 mm from the central axis in the X-direction. This is also the case Z-direction (not shown). The reduced field-of-view in the X-direction is compensated for in the in-vivo array due to its semi-annular design.

Simulations also indicate that higher increases in SNR should be possible if the material

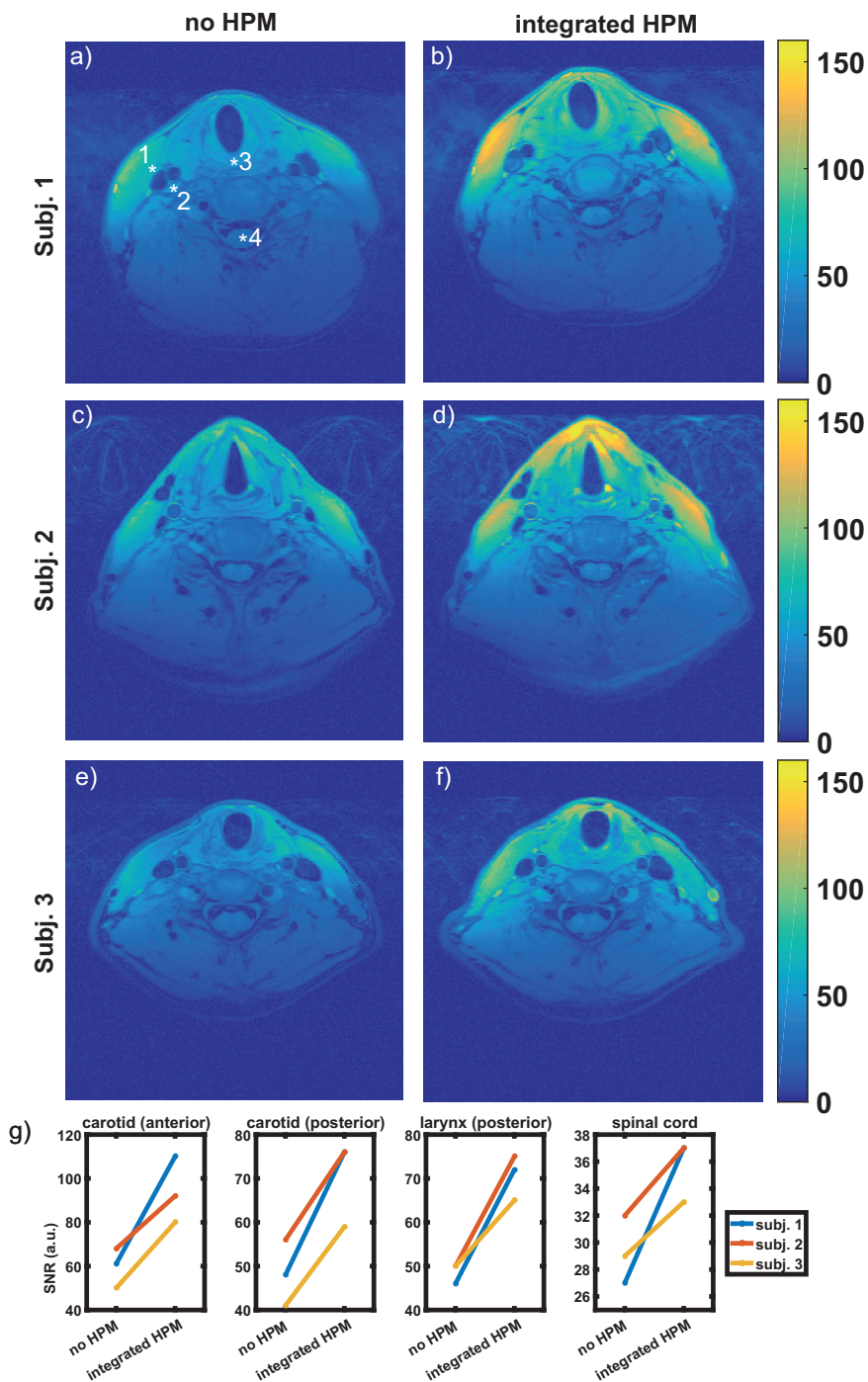


Figure 5.7: In-vivo SNR for three subjects using T1-weighted TSE sequences. a), c), e) conventional array. b), d), f) integrated HPM array. For every subject the same transmit power was used between scans with the two arrays. g) SNR for the conventional and integrated HPM array at the points depicted in Figure a), measured in the three subjects. For all subjects SNR gains are observed all four points.

permittivity is increased. However, this assumes that the loss tangent remains low relative to the body. For example, conductivities of 0.1, 0.5 and 1.0 S/m result in coil losses of 2.5, 11 and 19% respectively. These simulations show the importance of low-loss HPMs as the gains obtained in Figure 5.2f) are of the same order of magnitude with losses from 0.5 S/m onward, nullifying the HPM's effect.

One of the potential disadvantages of using integrated HPMs is the increase in weight of the array. The three-element integrated HPM coil in this paper has a mass of 760 grams, but this was not perceived as uncomfortable by any of the subjects in this study. This is in line with previous studies, where even larger amounts of HPM up to 4 kg on the chest have been used [26]. The use of integrated HPM coils would be much easier to realize in, for example, posterior body arrays integrated into the scanner bed. Weight can possibly be reduced by using water-based ceramics. Although their effectiveness has been shown in literature, their use in fully integrated HPM coils might be limited, as high relative permittivities (>300) are difficult to obtain and conductivities are often higher than 0.1 S/m [3, 4, 10].

5.5. ACKNOWLEDGEMENTS

The authors would like to thank Wyger Brink for performing simulations relating to this work and for extended discussions. This work was funded by the ERC under grant number 670629 and 737180, and by the NWO domain AES under grant number 13375.

REFERENCES

- [1] T. Ruytenberg, T. P. O'Reilly, and A. G. Webb, *Design and characterization of receive-only surface coil arrays at 3T with integrated solid high permittivity materials*, Journal of Magnetic Resonance **311**, 106681 (2020).
- [2] Q. X. Yang, W. Mao, J. Wang, M. B. Smith, H. Lei, X. Zhang, K. Ugurbil, and W. Chen, *Manipulation of image intensity distribution at 7.0 T: passive RF shimming and focusing with dielectric materials*, Journal of Magnetic Resonance Imaging: An Official Journal of the International Society for Magnetic Resonance in Medicine **24**, 197 (2006).
- [3] W. M. Teeuwisse, W. M. Brink, and A. G. Webb, *Quantitative assessment of the effects of high-permittivity pads in 7 Tesla MRI of the brain*, Magnetic resonance in medicine **67**, 1285 (2012).
- [4] W. M. Brink, *Dielectric shimming: exploiting dielectric interactions in High Field MRI*, Ph.D. thesis, Department of Radiology, Leiden University Medical Center (2016).
- [5] G. G. Haemer, G. Carluccio, and C. M. Collins, *Design of an 8ch dipole transmit array for head imaging with the use of a high permittivity material helmet shaped former*, in *2018 International Conference on Electromagnetics in Advanced Applications (ICEAA)* (IEEE, 2018) pp. 601–604.
- [6] A. Manoliu, G. Spinner, M. Wyss, D. A. Ettlin, D. Nanz, F. P. Kuhn, L. M. Gallo, and G. Andreisek, *Magnetic resonance imaging of the temporomandibular joint at 7.0 T using high-permittivity dielectric pads: a feasibility study*, Investigative radiology **50**, 843 (2015).
- [7] W. M. Brink, A. M. van der Jagt, M. J. Versluis, B. M. Verbist, and A. G. Webb, *High permittivity dielectric pads improve high spatial resolution magnetic resonance imaging of the inner ear at 7 T*, Investigative radiology **49**, 271 (2014).
- [8] G. Carluccio, G. Haemer, M. Vaidya, S. Rupprecht, Q. Yang, and C. M. Collins, *SNR Evaluation for a high-permittivity dielectric helmet-shaped coil former for a 28 channel receive array*, in *Proceedings 26. Annual Meeting International Society for Magnetic Resonance in Medicine*, Vol. 26 (Paris, France, 2018) p. 4405.
- [9] M. V. Vaidya, C. M. Deniz, C. M. Collins, D. K. Sodickson, and R. Lattanzi, *Manipulating transmit and receive sensitivities of radiofrequency surface coils using shielded and unshielded high-permittivity materials*, Magnetic Resonance Materials in Physics, Biology and Medicine **31**, 355 (2018).
- [10] Q. X. Yang, J. Wang, J. Wang, C. M. Collins, C. Wang, and M. B. Smith, *Reducing SAR and enhancing cerebral signal-to-noise ratio with high permittivity padding at 3 T*, Magnetic resonance in medicine **65**, 358 (2011).

- [11] Z. Yu, X. Xin, and C. M. Collins, *Potential for high-permittivity materials to reduce local sar at a pacemaker lead tip during MRI of the head with a body transmit coil at 3 T*, Magnetic resonance in medicine **78**, 383 (2017).
- [12] C. M. Collins, G. Carluccio, B. Zhang, G. Adriany, K. Ugurbil, and R. Lattanzi, *On the Relationship Between Field Strength and Permittivity for Desired Effects of High-Permittivity Materials in MRI*, in *Proceedings 27. Annual Meeting International Society for Magnetic Resonance in Medicine*, Vol. 27 (Montréal, Canada, 2019) p. 1566.
- [13] K. Koolstra, P. Börnert, W. Brink, and A. Webb, *Improved image quality and reduced power deposition in the spine at 3 T using extremely high permittivity materials*, Magnetic resonance in medicine **79**, 1192 (2018).
- [14] S. Rupperecht, C. T. Sica, W. Chen, M. T. Lanagan, and Q. X. Yang, *Improvements of transmit efficiency and receive sensitivity with ultrahigh dielectric constant (uHDC) ceramics at 1.5 T and 3 T*, Magnetic resonance in medicine **79**, 2842 (2018).
- [15] I. Zivkovic, W. Teeuwisse, A. Slobozhanyuk, E. Nenasheva, and A. Webb, *High permittivity ceramics improve the transmit field and receive efficiency of a commercial extremity coil at 1.5 Tesla*, Journal of Magnetic Resonance **299**, 59 (2019).
- [16] M. V. Vaidya, D. K. Sodickson, C. M. Collins, and R. Lattanzi, *Disentangling the effects of high permittivity materials on signal optimization and sample noise reduction via ideal current patterns*, Magnetic resonance in medicine **81**, 2746 (2019).
- [17] O. Ocali and E. Atalar, *Ultimate intrinsic signal-to-noise ratio in MRI*, Magnetic resonance in medicine **39**, 462 (1998).
- [18] D. K. Sodickson, R. Lattanzi, M. Vaidya, G. Chen, D. S. Novikov, C. M. Collins, and G. C. Wiggins, *The Optimality Principle for MR signal excitation and reception: new physical insights into ideal RF coil design*, in *Proceedings 25. Annual Meeting International Society for Magnetic Resonance in Medicine*, Vol. 25 (Honolulu, Hawaii, 2017) p. 0756.
- [19] H. Fujita, T. Zheng, X. Yang, M. J. Finnerty, and S. Handa, *RF surface receive array coils: the art of an LC circuit*, Journal of magnetic resonance imaging **38**, 12 (2013).
- [20] X. Yan, J. C. Gore, and W. A. Grissom, *New resonator geometries for ICE decoupling of loop arrays*, Journal of Magnetic Resonance **277**, 59 (2017).
- [21] D. Seeber, J. Jevtic, and A. Menon, *Floating shield current suppression trap*, Concepts in Magnetic Resonance Part B: Magnetic Resonance Engineering: An Educational Journal **21**, 26 (2004).
- [22] P. Kellman and E. R. McVeigh, *Image reconstruction in SNR units: a general method for SNR measurement*, Magnetic resonance in medicine **54**, 1439 (2005).
- [23] K. Nehrke and P. Börnert, *DREAM-a novel approach for robust, ultrafast, multislice B1 mapping*, Magnetic Resonance in Medicine **68**, 1517 (2012).

- [24] T. Ruytenberg, B. M. Verbist, J. Vonk-van Oosten, E. Astreinidou, E. V. Sjögren, and A. G. Webb, *Improvements in high resolution laryngeal magnetic resonance imaging for preoperative transoral laser microsurgery and radiotherapy considerations in early lesions*, *Frontiers in oncology* **8**, 216 (2018).
- [25] P. De Heer, W. Brink, B. Kooij, and A. Webb, *Increasing signal homogeneity and image quality in abdominal imaging at 3 T with very high permittivity materials*, *Magnetic resonance in medicine* **68**, 1317 (2012).
- [26] S. Aussenhofer and A. Webb, *An eight-channel transmit/receive array of TE₀₁ mode high permittivity ceramic resonators for human imaging at 7 T*, *Journal of Magnetic Resonance* **243**, 122 (2014).

6

SUMMARY AND GENERAL DISCUSSION

T. RUYTENBERG

6.1. SUMMARY

This thesis describes novel magnetic resonance imaging (MRI) surface antennas and arrays, and their applications at both 3 and 7 Tesla. While the first half of this work describes flexible lightweight antenna arrays, the other half focuses on the use of solid ceramic high-permittivity materials as a substantial part of the antenna.

Chapter 2 presents a flexible lightweight four-element antenna array for use on the neck, particularly designed to image the larynx at 3 Tesla. As the benefits, limitations, and contraindications of transoral laser microsurgery in glottic carcinoma treatments become better defined, pretreatment imaging has become more important. MRI is the preferred modality to image such laryngeal tumors, even though imaging the larynx using MRI can be difficult. The first challenge is that there are no commercial RF coils that are specifically designed for imaging the larynx. Second, motion in the neck region induced by breathing, swallowing, and vessel pulsation can induce severe image artifacts, sometimes rendering the images unusable. In this chapter, a dedicated RF coil array was designed, which allows high quality high-resolution imaging of the larynx. In addition, it is shown that introducing respiratory-triggered acquisition improves the diagnostic quality of the images by minimizing breathing and swallowing artifacts. Together, these developments enable robust, essentially artifact-free images of the full larynx with an isotropic resolution of 1 mm to be acquired within a few minutes.

Chapter 3 describes a novel flexible coil element design at 7 Tesla, based on a thin coaxial cable as main part of the resonant circuit. The performance of these shielded-coaxial-cable (SCC) coils as elements for multi-channel receive-only and transceive arrays were compared with equivalently-sized conventional loop coils. The SCC coils consist of a coaxial loop with interrupted central conductor at the feed-point side and an interrupted shield at the opposite point. Inter-element decoupling, transmit efficiency, and sample heating were compared with results from conventional capacitively-segmented loop coils. Three multi-channel arrays were constructed and their inter-element decoupling was characterized via measured noise correlation matrices and additionally under different flexing conditions of the coils. The measured and simulated transmit field maps of both SCC and conventional loops were very similar. For all the arrays constructed, the inter-element decoupling was much greater for the SCC elements than the conventional ones. Even under high degrees of flexion, the coupling coefficients were lower than -10 dB, with a much smaller frequency shift than for the conventional coils. This makes them suitable for the construction of size adjustable arrays.

Chapter 4 describes the detunability of receive-only dielectric resonator antenna arrays at 7 Tesla, made of solid ceramic-based resonators with a high electric permittivity. Such antenna designs incorporating dielectric resonator have been implemented in high-frequency MRI and microscopy in literature. When used in MRI as elements for a transmit array, the intrinsically low inter-element coupling allows flexibility in designing different geometric arrangements for different regions-of-interest. However, without being able to detune such resonators, they cannot be used as elements in a receive-only ar-

ray. In this chapter a method based on mode-disruption is proposed and implemented, in order to detune ceramic-based dielectric resonators and to enable them to be used as receive-only elements. Eigenmode simulations were performed to understand the working principle of the implemented detuning method and a four-element array was built for extremity imaging. Images of the ankle are shown as proof of principle.

Chapter 5 builds on both chapter 2 and 4 and uses non-resonating solid ceramic high-permittivity materials. The chapter describes the full integration of these materials in receive-only surface coil arrays at 3 Tesla. After design and construction of such an array with solid ceramic high-permittivity material, its performance was evaluated and compared in terms of transmit field efficiency and specific absorption ratio during transmit, and signal-to-noise ratio during receive, with a conventional identically-sized surface coil array. Finite-difference time-domain simulations, bench measurements and in-vivo neck imaging on three healthy volunteers were performed using a three-element surface coil array with integrated high-permittivity materials placed around the larynx. Simulation results show an increase in local transmit efficiency of the body coil of ~10-15% arising from the presence of the high-permittivity material. The receiver efficiency also increased by approximately 15% close to the surface. Phantom experiments confirmed these results. In-vivo scans using identical transmit power resulted in signal-to-noise ratio gains throughout the laryngeal area when compared with the conventional surface coil array. In particular specifically around the carotid arteries an average signal-to-noise ratio gain of 52% was measured averaged over the three subjects, while in the spine an average of 20% signal-to-noise ratio gain was obtained.

6.2. GENERAL DISCUSSION

The overall goal of the work presented in this thesis has been introducing increased SNR in MRI using close-fitting coils. This was applied to a geometrically difficult region like the neck in Chapter 2, was carried out by fabricating a flexible transceive array in Chapter 3, and by introducing high-permittivity materials in Chapters 4 and 5.

FLEXIBILITY

Creating flexible coil arrays benefits MRI in multiple ways. Firstly, by positioning the receive coils closer to the region of interest, the sensitivity goes up and therefore SNR benefits are evident. Secondly, one has to take into account that over the past decades average body dimensions have grown substantially and obesity is much more prevalent [1]. Additionally, due to the increased risk of health problems in this specific patient group, this group will also more often appeal to the use of diagnostic medical imaging while medical imaging in general is more difficult in these patients [2]. Flexible arrays could serve as a one-size-fits-all coil and the introduction of such coils will ease the applicability of MRI specifically in this patient group.

Multiple reasons form the basis for the limited availability of flexible commercial coils at the momentⁱ. A main and foremost reason is that a flexible array can be difficult to tune, match and decouple, due to the coil having the ability to obtain a different geometry and due to a variety of different loading conditions. Especially decoupling using overlap does not work under these varying conditions. Less load sensitive methods do exist, like the induced current elimination used in Chapter 2. A second reason is the difficulty to produce active medical devices that are flexible but can still guarantee mechanical integrity though the test of time when intensively used. When building flexible transmit arrays, as done in Chapter 3, matters become even more complex with regards to safety assessments of induced E-field heating. These assessments are nowadays often done via finite-difference time-domain simulations of the coil on body voxel models. Not only can flexible arrays be positioned in many different ways, also the loading conditions of the individual elements will change for every application which can change their produced electric fields. Therefore a single simulation might not suffice for performing safety assessments of flexible transmit arrays.

HIGH-PERMITTIVITY MATERIALS

6

The use of solid high-permittivity materials contrasts everything written before in this discussion concerning flexibility and a one-size-fits-all coil. The materials itself are non-flexible and very dense as they are obtained by compressing and sintering ceramic powder, which makes these materials heavy. Additionally these materials are often very brittle, requiring special care when incorporating them into MRI coils. Flexible high-permittivity materials do exist in the form of ceramic powders mixed with water or deuterium oxide, but do not achieve relative permittivities higher than ~300 for mixtures with barium titanate [3].

In the Chapters 4 and 5, both resonating and non-resonating high-permittivity materials were studied. While with both types of materials working devices were obtained, a couple of points are to be considered. In Chapter 4 hyperintensities were observed directly underneath the resonators, while this was not the case while imaging with the non-resonating materials. These hyperintensities can result in spectral leakage artefacts (Gibbs ringing). A comparison performed by Rupprecht et al. [4], showed less differences in imaging when comparing resonating with non-resonating high-permittivity materials. One also has to consider that building coils with dielectric resonators, this does take additional effort compared to the non-resonators, as the coupling from a pick-up loop to the resonator has to be precisely tuned. Therefore, the non-resonating high-permittivity materials seem like a more robust solution to incorporate into future MRI coils.

Next steps into incorporating these materials in MRI coils, would be creating larger arrays. One would however quickly encounter the boundaries of what is possible weight-wise due to the high density of the materials. Incorporating into posterior coils inside the

ⁱGE healthcare recently introduced their AIR Technology™, a set of flexible blankets incorporating coils with coaxial cables as a basis for the resonator.

scanner bed, and into head coils could be considered low hanging fruit as these structures are not mechanically weighing down on the patient and these constructions are often robust. Because head coils are occasionally moved around the scanner room, total weight has to be considered.

Scaling up is a process that can be rather difficult in a research environment. Not only is advanced knowledge on mechanical constructions required for making large arrays with heavy materials, also accessibility to a variety of manufacturing methods will be necessary to be able to meet the standards of the Medical Device Regulation of the European Union. Such a step might therefore only be feasible by a partnership with manufacturers or should be carried out by manufacturers as a whole.

REFERENCES

- [1] NCD Risk Factor Collaboration, *Trends in adult body-mass index in 200 countries from 1975 to 2014: a pooled analysis of 1698 population-based measurement studies with 19.2 million participants*, The Lancet **387**, 1377 (2016).
- [2] R. N. Uppot, D. V. Sahani, P. F. Hahn, D. Gervais, and P. R. Mueller, *Impact of obesity on medical imaging and image-guided intervention*, American Journal of Roentgenology **188**, 433 (2007).
- [3] W. M. Brink, *Dielectric shimming: exploiting dielectric interactions in High Field MRI*, Ph.D. thesis, Department of Radiology, Leiden University Medical Center (2016).
- [4] S. Rupprecht, B. Tilakaratne, C. R. Messner, C. Sica, M. T. Lanagan, W. Chen, and Q. X. Yang, *Design of Self-Resonance Modes (SRM) of monolithic ultra-high dielectric constant (uHDC) materials and RF Coils for B1 field enhancement*, in *Proceedings 25. Annual Meeting International Society for Magnetic Resonance in Medicine*, Vol. 25 (Honolulu, Hawaii, 2017) p. 2703.

NEDERLANDSE SAMENVATTING

Dit proefschrift beschrijft nieuwe oppervlakteantennes voor kernspintomografie (MRI) op veldsterktes van 3 en 7 Tesla, samenstellingen daarvan en hun applicaties. De eerste helft van dit werk beschrijft flexibele samenstellingen van antennes met een laag totaal-gewicht. De tweede helft richt zich op het gebruik van solide keramisch materiaal met een hoge elektrische permittiviteit als substantieel onderdeel van de antenne.

In **hoofdstuk 2** wordt een flexibele, lichtgewicht antenne beschreven met vier elementen voor gebruik op de nek, specifiek om het strottenhoofd af te beelden op 3 Tesla. Naarmate de voordelen, limitaties en contra-indicaties van transorale lasermicrochirurgie in de behandeling van strottenhoofdkanker beter gedefinieerd worden, wordt medische beeldvorming voor uitvoering van deze behandeling steeds belangrijker. Beeldvorming middels MRI heeft de voorkeur van het afbeelden van zulke tumoren, maar dat kan lastig zijn. De eerste uitdaging is dat er geen commerciële RF antennes voor MRI bestaan die specifiek ontwikkeld zijn voor het afbeelden van het strottenhoofd. Ten tweede kan beweging in de nekregio, geïnduceerd door ademhaling, slikken en pulsatie van de halsslagader, grote artefacten in het beeld veroorzaken waardoor de beelden onbruikbaar kunnen worden. In dit hoofdstuk is een antenne ontwikkeld, specifiek voor het afbeelden van het strottenhoofd met hoge resolutie. Daarnaast wordt aangetoond dat de diagnostische kwaliteit van de beelden sterk wordt verhoogd indien data-acquisitie enkel wordt uitgevoerd tijdens uitademing, doordat daarmee de artefacten door ademhaling en slikken worden verminderd. Deze ontwikkelingen maken het samen mogelijk om robuuste, artefact-vrije beelden van het volledige strottenhoofd te verkrijgen met isotrope resolutie van 1 mm in slechts enkele minuten.

Hoofdstuk 3 beschrijft een nieuw flexibel antenne-ontwerp voor 7 Tesla beeldvorming, gebaseerd op een dunne coaxiale kabel als hoofdonderdeel van het resonante circuit. De prestaties van deze coaxiale-kabelantenne (SCC-antenne) als element voor meerkanaals ontvangst- en zendontvangstsamenstellingen worden vergeleken met conventionele lusantennes van gelijke grootte. De SCC-antenne bestaat uit een coaxiale kabel in de vorm van een lus met een onderbroken centrale geleider bij het voedingspunt van de antenne en daar tegenover een onderbroken schild. Ontkoppeling tussen de elementen, zendefficiëntie en opwarming van het af te beelden object zijn vergeleken met resultaten van een conventionele capaciteef-gesegmenteerde lusantenne. Drie meerkanaals-antennesamenstellingen zijn geconstrueerd en hun interelementontkoppeling is gekarakteriseerd middels gemeten ruiscorrelatiematrices. Deze karakterisatie is ook uitgevoerd terwijl de antennes gebogen waren. De gemeten en gesimuleerde zendveldkaarten van zowel de SCC-antenne als de conventionele lusantenne blijken erg vergelijk-

baar. Voor alle geconstrueerde antennesamenstellingen was de interelementontkoppeling hoger voor de SCC-antennes, dan voor de conventionele lusantennes. Zelfs wanneer de samenstellingen sterk gebogen werden, waren de ontkoppelcoëfficiënten lager dan -10 dB, met een lagere frequentieverschuiving dan bij de conventionele lusantennes. Hierdoor zijn ze erg geschikt voor gebruik in flexibele en op maat verstelbare antennesamenstellingen.

Hoofdstuk 4 gaat in op de ontstembaarheid van samenstellingen van ontvangstantennes op basis van diëlektrische resonatoren op 7 Tesla. Deze diëlektrische resonatoren bestaan uit een solide, keramisch materiaal met hoge elektrische permittiviteit. Dit soort antenne-ontwerpen met diëlektrische resonatoren zijn in de literatuur eerder geïmplementeerd in hoge-veld MRI en microscopie. Wanneer deze gebruikt worden als samenstellingen van zendantennes, geeft dat extra mogelijkheden in het ontwerp van de geometrie van deze samenstellingen door de intrinsiek lage interelementkoppeling, waardoor ze makkelijk op verschillende anatomieën gebruikt kunnen worden. Echter kunnen zij, zonder de mogelijkheid deze resonatoren te ontstemmen, niet worden gebruikt als elementen in samenstellingen van ontvangstantennes. In dit hoofdstuk wordt een methode voorgesteld en geïmplementeerd waarbij de resonante modus wordt verstoord, om zo de keramische diëlektrische resonatoren te ontstemmen en ze te gebruiken als ontvangstantennes. Eigenmodus simulaties zijn uitgevoerd om het werkingsprincipe van de geïmplementeerde ontstemmethode te begrijpen en er is een vier-elements antennesamenstelling ontworpen om extremiteiten mee af te beelden. Afbeeldingen van een enkel worden getoond om de bruikbaarheid van zulke antennesamenstellingen aan te tonen.

Hoofdstuk 5 bouwt voort op zowel hoofdstuk 2 als 4 en gebruikt daarbij solide, niet-resonante keramische materialen met een hoge elektrische permittiviteit. Het hoofdstuk beschrijft de volledige integratie van deze materialen in samenstellingen van ontvangst-oppervlakteantennes op 3 Tesla. Na het ontwerp en de constructie van zulke samenstellingen zijn de prestaties ervan geëvalueerd en vergeleken met een gelijkvormige conventionele antenne op het gebied van zendefficiëntie, opwarming tijdens het zenden en de signaal-ruisverhouding in ontvangst. Er zijn computersimulaties, elektronische metingen en vervolgens in-vivo metingen uitgevoerd waarbij bij drie gezonde proefpersonen afbeeldingen van de nek zijn gemaakt middels een driekanaalssamenstelling van oppervlakte-elementen met geïntegreerd materiaal van hoge permittiviteit. Simulatie-resultaten laten zien dat de lokale zendveldefficiëntie van de lichaamsspoel ~10-15% verhoogd wordt door de aanwezigheid van het materiaal met hoge permittiviteit. De ontvangstefficiëntie neemt dichtbij het oppervlak eveneens met ongeveer 15% toe. Fantoomexperimenten bevestigen deze resultaten. In-vivo metingen met gelijk zendvermogen laten in het gehele strottenhoofd een toename van de signaal-ruisverhouding zien bij gebruik van de nieuwe antennesamenstelling in vergelijking met een conventionele antennesamenstelling. Specifiek rond de halsslagaders is een toename van signaal-ruisverhouding over drie proefpersonen gemeten van gemiddeld 52%. In de wervelkolom was deze gemiddelde toename 20%.

ACKNOWLEDGEMENTS

This work would not have been possible without the support of many individuals. On this page I would like to express my gratitude to them.

Andrew, your knowledge in MR and RF, and your out-of-the-box thinking has been very valuable during the time I was around. You gave me the opportunity to look into the huge world of MR and to develop in whichever direction I was interested in. You were also able to get me back on track when things got stuck. Thank you for your guidance, even when you were abroad which did not refrain you from answering my emails within minutes.

Another person which I would like to thank specifically is Wouter. Your perseverance towards quality of the devices and tools we built in the workshop is admirable. I have to admit that I did learn from most of the comments you made on tool handling, most of them...

Thanks to Wyger, Tom, Irena, Jan-Willem and Nick, who made working in the workshop so much more fun. My office mates that survived the full four years with me, Nathalie and Wyger, thank you for the positive atmosphere in our daylight-deprived office.

Memories I will never forget were created during our after-ISMRM travels. I am very grateful for the opportunity to go to the most exotic places with a wonderful selection of people. Kirsten, Merlijn, Marjolein, Wyger, Myriam, Jedrek and Thom, we've had the most amazing times visiting cities in Malaysia, hiking on multiple Hawaiian islands and doing an RV trip through Quebec, Canada.

Thanks also go to Thijs van Osch, for his help with getting approval from the research ethics committee on the larynx coil, to Berit, Eleftheria, Elisabeth and Jordi for their input and effort on the larynx project, and to the gentlemen of Machnet for their continued effort on creating a commercial product from the prototypes in this dissertation.

I am grateful for being a part of the Gorter group. I enjoyed the multidisciplinary and the open atmosphere in the group. Don't forget to keep going for Friday afternoon drinks!

The Leidse Studenten Duikvereniging gave me the opportunity to look beyond what you can see above the water surface, to express my technical affinity on their scuba dive equipment and to develop some organisational skills. Gabriël, Pelle, Esther and Luuk, thanks for spending a full year with me when I was not doing my PhD research. It en-

riched my life a lot.

Final thanks will go to my family and to Annick. Without your continued love and support, I would not have been where I am now.

CURRICULUM VITÆ

Thomas Ruytenberg was born on the 6th of January 1992 in Capelle aan den IJssel. In 2013 he received a bachelor in *Physics* at Leiden university after having worked on an acoustic cardiac trigger for MRI at the C.J Gorter Center for High-Field MRI. He continued education during his master in *Research in Experimental Physics*, where he worked on more fundamental subjects. After having received his master's degree in 2015, he returned to the C.J. Gorter Center for High-Field MRI for a PhD position in MRI hardware, on which this dissertation was based.

Currently, Thomas is a Medical Physics Resident hoping to make progress on implementing new techniques into clinical healthcare.

LIST OF PUBLICATIONS

9. **T. Ruytenberg**, A.G. Webb and I. Zivkovic, *A flexible five-channel shielded-coaxial-cable (SCC) transceive neck coil for high resolution carotid imaging at 7T*, Magnetic Resonance in Medicine; *in press*.
8. **T. Ruytenberg**, T.P. O'Reilly and A.G. Webb, *Design and characterization of receive-only surface coil arrays at 3T with integrated solid high permittivity materials*, Journal of Magnetic Resonance **311**, 106681 (2020).
7. **T. Ruytenberg**, A.G. Webb and I. Zivkovic, *Shielded-coaxial-cable (SCC) coils as receive and transceive array elements for 7T human MRI*, Magnetic Resonance in Medicine **83**, 1135-1146 (2020).
6. **T. Ruytenberg**, B.M. Verbist, J. Vonk-van Oosten, E. Astreinidou, E.V. Sjögren and A.G. Webb, *Improvements in High Resolution Laryngeal Magnetic Resonance Imaging for Preoperative Transoral Laser Microsurgery and Radiotherapy Considerations in Early Lesions*, Frontiers in Oncology **8**, 216 (2018).
5. T.P. O'Reilly, **T. Ruytenberg** and A.G. Webb, *Modular transmit/receive arrays using very high permittivity dielectric resonator antennas*, Magnetic Resonance in Medicine **79.3**, 1781–1788 (2018).
4. **T. Ruytenberg** and A.G. Webb, *Design of a dielectric resonator receive array at 7 Tesla using detunable ceramic resonators*, Journal of Magnetic Resonance **284**, 94–98 (2017).
3. M.P. Bakker, A.V. Barve, **T. Ruytenberg**, W. Löffler, L.A. Coldren, D. Bouwmeester and M.P. van Exter *Polarization degenerate solid-state cavity quantum electrodynamics*, Physical Review B **91**, 115319 (2015).
2. M.P. Bakker, **T. Ruytenberg**, M.P. van Exter and D. Bouwmeester, *Quantum dot nonlinearity through cavity-enhanced feedback with a charge memory*, Physical Review B **24**, 241305 (2015).
1. **T. Ruytenberg**, A.G. Webb and J.W.M. Beenakker, *A multi-purpose open-source triggering platform for magnetic resonance*, Journal of Magnetic Resonance **247**, 15–21 (2014).